2014

Phases of bosons in optical lattices and coupled to artifical gauge fields

Qinqin Lu
Louisiana State University and Agricultural and Mechanical College

PHASES OF BOSONS IN OPTICAL LATTICES AND COUPLED TO ARTIFICIAL GAUGE FIELDS

A Dissertation

Submitted to the Graduate Faculty of the
Louisiana State University and
Agricultural and Mechanical College
in partial fulfillment of the
requirements for the degree of
Doctor of Philosophy

in

The Department of Physics and Astronomy

by
Qinqin Lu
B.S., University of Science and Technology of China, 2008
May 2014

The degree candidate's name is 吕骎骎 in Chinese. Due to variations of transliterating Chinese characters into the Latin alphabet, the candidate's name can be spelt as any combination of Qinqin, QinQin, Qin-Qin (given name), and Lu, Lü, Lyu, Lv, Lui (surname).

为自己的日子
在自己的脸上留下伤口
因为没有别的一切为我们作证

—— 海子《我，以及其他的证人》

ACKNOWLEDGMENTS

During my Ph.D. study, there have been many people who I am grateful to. I would like to thank my advisor Dr. Daniel Sheehy for his insightful directions and kind guidance in my daily research. I would like to thank Dr. Kelly Patton, a former postdoctoral member in our group, for the useful discussions with him. I would like to thank my committee members for their time devoted. I would like to thank the professors who have instructed or helped me, especially Dr. A. Ravi. P. Rau, for their enthusiasm on students.

I would like to thank my friends, local and international, for their support which is indispensable to my career and my life. I would like to express my special gratitude to my old friends from my hometown or from my undergraduate university, for our long and steadfast friendship. We will take a cup of kindness, for *auld lang syne*. I would like to thank my parents and my extended family for their unswerving love to which I am forever indebted. 爸爸妈妈，谢谢你们。

I would like to thank the world for its massive diversity and thank all human civilizations for their breathtaking creativity, as seeking truth, beauty and virtue in them makes a meaningful life.

Lastly, to quote Bertrand Russell, "Of all forms of caution, caution in love is perhaps the most fatal to true happiness."

TABLE OF CONTENTS

LIST OF FIGURES

ABSTRACT

Ultracold atoms have emerged as an indispensable setting to study quantum many-body systems. Recent experimental and theoretical work has explored the curious phases and novel properties of Bose-Einstein Condensate with optical lattices, and Bose-Einstein Condensate with light-induced artificial spin-orbit coupling. In this thesis, we report our research on these two types of boson systems.

In the first topic, in contrast with calculations of bosons in optical lattices that focus on the tight-binding regime, we note that the single-particle states of bosons in a periodic potential generally satisfy the Mathieu equation, and have developed a formalism for studying bosons in an optical lattice using the Mathieu equation. Moreover, based on this formalism, we have proposed a self-consistent scheme for describing interacting bosons in an optical lattice using Hartree Fock approximation. We apply this scheme to quantify the effects of inter-atomic interactions on the properties of bosons in an optical lattice, as exhibited in the comparison between observables of non-interacting and interacting systems, such as the superfluid transition temperature and momentum distribution as probed in time-of-flight expansion.

In the second topic, the phases of a Bose-Einstein condensate with light-induced spin-orbit coupling are studied within the mean-field approximation. We obtain the phase diagram at fixed chemical potential and at fixed density for bosons with spin-orbit coupling, finding a regime of phase separation and a regime in which the bosons condensed into a mixed phase. We determine how this phase diagram evolves as a function of the atom interaction parameters and as a function of the strength of light-atom coupling. The mixed phase is found to be stable for sufficiently small light-atom coupling. Specifically, we show that the structure of the

phase diagram at fixed chemical potential suggests an unusual density dependence for the mixed phase in a harmonic trapping potential, in which the density of one spin increases with increasing radius, suggesting a unique experimental signature of this state. The collective Bogoliubov sound mode is shown to also provide a signature of the mixed phase, vanishing as the boundary to the regime of phase separation is approached.

Together, in these two topics we address the need to enhance the understanding of the unconventional physical properties of Bose-Einstein Condensate in a controlled electromagnetic environment (optical lattices, Raman lasers, etc.), and provide predictions for possible experimental findings.

CHAPTER 1
INTRODUCTION

Physics is the science to comprehend the physical world at all scales. At the atomic level, ultracold atoms is a unique field which is both intrinsicly interesting by itself and extensively applicable for simulating various quantum systems. It is an essential tool to understand condensed matter systems, a vital path to realize quantum computation, a pioneering index in the search for new materials, and a beneficial alternative to achieve systems of extreme conditions that are otherwise difficult to be realized.

What is really special about cold atoms is their highly controllable environment. An array of parametric conditions can be carefully tuned for single particles, few body systems and in particular many body systems, in the last of which the atoms exhibit macroscopic quantum phenomena in many-body phases.

The field has seen rapid advance in the recent two decades. After the first realization of Bose-Einstein Condensation, with the integration of optical, magnetic or electronic setups, ultracold atoms have been used to study systems bearing fundamentally distinct symmetries and to explore novel phases that were never discovered before. Translational symmetry breaking optical lattices bring in spatial periodicity, mimicking conventional condensed matter systems. The coupling to artificial abelian and non-abelian gauge fields expands the space of Hamiltonian for cold atoms and enable them to show behaviors that were usually reserved for systems of higher energy. My thesis research focuses on the phases of bosons that are coupled to artificial gauge fields and in optical lattices, spiced up with interatomic interactions which can greatly change the overall picture. This first chapter serves as a general introduction.

1.1 A Brief History of Ultracold Bosons

We begin by recalling the development of cold bosons in a historic perspective. In 1924-1925, Bose [1] and Einstein [2, 3] predicted that bosons form a condensate at an extremely low temperature, laying the cornerstone of this field. In this new phase called Bose-Einstein Condensate (BEC), bosons collectively occupy the lowest state and share the same wavefunction. Since then scientists have been actively looking for BEC in possible candidates. As laser cooling techniques developed, the $\sim$100 nanokelvin (nK) range and below finally became accessible during the late 20th century [4], when the pursuit for BEC finally succeeded in dilute gases of alkali atoms in 1995 (rubidium-87 [5], lithium-7 [6], sodium-23 [7]). Carl Wieman, Eric Cornell and Wolfgang Ketterle shared the 2001 Nobel Prize for their contribution to the experimental discovery of BEC. A false color image of the velocity distribution of BEC is shown in Fig. $1-1$.

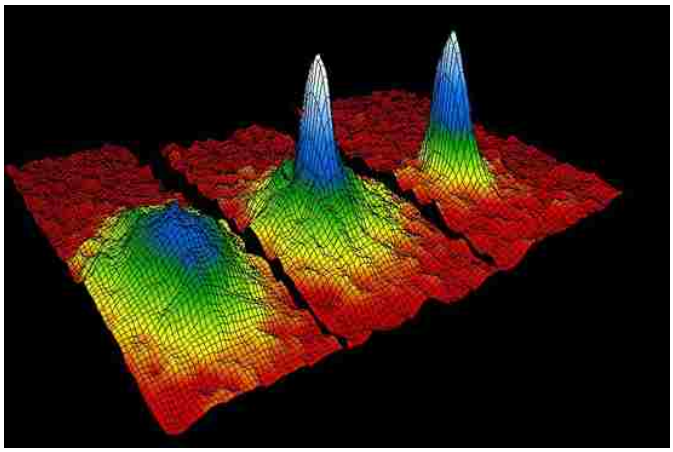

Figure 1-1: Velocity distribution of atomic cloud at 400, 200, 50 nK (from left to right). BEC appears in the latter two. Blue and white shading indicates higher density. NIST/JILA/CU-Boulder image [8]

Since the realization of BEC, it has been used to study a wide variety of problems by experimentalists. The interference of two overlapping condensates [11]

explicitly indicates the matter-wave nature of BECs. The phase transition from superfluid to Mott insulator [9, 10] investigates how a zero-temperature system in a deep lattice would behave at the strong interacting limit. With the introduction of disorder through rugged optical lattices, cold atoms can be a vivid matter-wave example of Anderson localization [15]. The Josephson effect experiment for cold atoms [14] establishes an analog to superconductor. The quantized vortex in a rotating BEC [12, 13] effectively creates an artificial vector potential in superfluids. One could easily recognize the phenomenal potential of BEC-related experiments in this incomplete list.

A recent focus in cold atoms is the coupling with artificially engineered gauge fields. Since 2009, NIST reported the realization of artificially created electromagnetic fields, including uniform gauge field [31], magnetic field [32], electric field [33] and the first success of artificially engineered spin-orbit coupling(SOC) [34]. The presence of SOC in cold atoms opens the door for studying novel physical behavior in condensed matter systems such as spin-Hall effect [40, 41, 42, 55, 56], for searching topological insulators [39, 43] and for finding new spintronic materials [44, 45]. The engineering of artificial gauge fields have helped cold atoms enter a larger set of Hamiltonians such as an effective Dirac Hamiltonian which leads to Zitterbewegung [46, 47] and the Harper Hamiltonian which produces Hofstadter's butterfly [54]. The connections between cold atoms and other fundamental fields are still strongly growing.

1.2 Structure of This Thesis

The main text of this dissertation consists of seven chapters, including this introductory chapter. The next six chapters are organized as the following.

We begin from introducing existing non-interacting and interacting theories for BEC as foundations for our study. In Chapter 2, the natural starting point is to

show how BEC arises from the simplest non-interacting system. After that we discuss a few theoretical tools to deal with interacting systems applicable for different temperature and interaction regimes. Our main focus is on mean-field theory, including Gross-Pitaevskii Equation, Bogoliubov Approximation and Hartree Fock Approximation. Strong correlation theory such as the Bose-Hubbard Model is also introduced. Besides systems that only have a single type of interaction, we also treat an interacting boson system of two species at the end of this chapter.

Then, we proceed to the theory of bosons in an optical lattice in Chapter 3. We start from the the non-interacting theory for bosons in a periodic lattice potential, including the system's eigenvalue equation - the Mathieu Equation, which our work on the thermodynamic properties, BEC phase transition and the momentum distribution is based on. We apply our understanding of the exact single-particle eigenstates of bosons in an optical lattice to calculate the density profile after time-of-flight free expansion. An preliminary discussion of the interacting effects on bosons in an optical lattice is at the end of this chapter.

Chapter 4 carries on the study on interacting bosons in an optical lattice. We propose a self-consistent scheme utilizing the Hartree-Fock Approximation, essentially treating interaction as an additional periodic potential. Using this scheme, we make predictions for experimental observables such as the superfluid transition temperature, condensate fraction and the boson momentum distribution, thus quantitatively delineate how a boson system in an optical lattice is influenced by inter-atomic interactions.

Beginning at Chapter 5, we switch gears and work on cold atoms with artificial gauge fields. In this chapter, we introduce the current experimental setups for engineering artificial spin-orbit coupling for bosons by NIST, and derive the spin-orbit Hamiltonian to reveal the spin-orbit coupling structure in the Hamiltonian.

Chapter 6 elaborates on the phases of spin-orbit coupled bosons with an emphasis on the miscible BEC phase which originates from a mix of the two spin states. We first demonstrate the interesting band structure of double local minima implied by the spin-orbit Hamiltonian. Based on the band structure, we construct a low energy effective Hamiltonian, which we then examine in detail for the phase transition from the separated phases into the miscible phase and produce two interconnected phase diagrams at fixed density and fixed chemical potential ensembles. Using the phase diagram, we obtain the density distribution for spin-orbit bosons in a harmonic trap. Crucially, we discover an non-trivial density dependence for one spin species in the trap which could serve as an experimental signature for the BEC-mixed state. Last but not the least, the collective modes are also studied as a possible signature for the miscible state in this chapter.

The last chapter, Chapter 7 concludes the thesis research by reiterating the motives and providing a summary of the topics in previous chapters, and places our research in the context of a larger picture. We will also try to connect to possible extensions of our research in this chapter.

CHAPTER 2
NON-INTERACTING AND INTERACTING BEC

Bose-Einstein Condensate (BEC) are a group of bosons that collectively share the same wave function when temperature drops below the critical point. In its pristine form, a BEC of non-interacting bosons isolated from any external fields is just a purely statistical phenomenon and has been standard textbook materials for decades. However, in real life there are always inter-atomic interactions present. Interaction between particles is a problem central to physics, and more than often it can be an intricate one. Interaction brings in rich phases and properties to a given system, but also poses great challenges for physicists. Different schemes are developed to tackle interaction under approximations appropriate to the given system. In this chapter, we will introduce the basics of non-interacting BEC, and review several mechanisms to treat interacting systems which will be used in later chapters.

2.1 Thermodynamics of Non-Interacting BEC

To start, it is essential to know why a simple BEC is possible. Bosons obey Bose-Einstein statistics. The total number of bosons is a sum over all states of the Bose distribution function evaluated for the energy of that state:

$$N = \sum_i n_B(\varepsilon_i - \mu) = \sum_i \frac{1}{e^{\beta(\varepsilon_i - \mu)} - 1}, \tag{2.1}$$

where n_B is the Bose distribution, $\beta = 1/k_B T$, k_B is the Boltzmann constant, T is temperature, μ is the chemical potential and ε_i is the energy of the i-th state. We also denote the state with the lowest energy ε_0 as the ground state, which is

$\varepsilon_0 = 0$ for free gas. When temperature goes down, if the volume and the total particle number are fixed, the negative valued μ increases. When μ reaches ε_0, Bose-Einstein condensation occurs and the temperature is called the critical temperature T_c. Therefore, T_c can be solved from Eq. 2.1 by setting $\mu = \varepsilon_0$. Below T_c, μ stays at ε_0 and the system possesses a BEC.

For free bosons, the single particle energy $\varepsilon_k = \hbar^2 k^2/2m$ with $\hbar k$ the boson momentum and $\hbar$ the Planck constant. After converting summation to integral, Eq. 2.1 gives the particle number

$$N = \zeta(\frac{3}{2})\frac{V}{[\lambda(T_c)]^3}, \tag{2.2}$$

where λ is the thermal de Broglie wavelength $\lambda(T) = \sqrt{2\pi\hbar^2/mk_BT}$, and V is the volume. The Riemann zeta function $\zeta(\frac{3}{2}) \approx 2.6124$. We can also write Eq. 2.2 equivalently as

$$T_c = (\frac{N/V}{\zeta(3/2)})^{\frac{2}{3}}\frac{2\pi\hbar^2}{mk_B} \approx 3.3125\frac{\hbar^2}{mk_B}(\frac{N}{V})^{\frac{2}{3}}. \tag{2.3}$$

The number density N/V is proportional to $T_c^{3/2}$. The critical condition can also be stated as λ being comparable to the average separation between atoms [23].

When T is below T_c, some particles enter the ground state, and are missed from the integral. The right hand side of Eq. 2.1 is now only the excited atoms, which is less than the total number of atoms. The difference

$$N_0 = N - \sum_{i\neq 0}\frac{1}{e^{\beta(\varepsilon_i-\mu)}-1} \tag{2.4}$$

is the number of atoms at the ground state, i.e. in the condensate. The condition for BEC can be defined as when the condensate occupies a macroscopic fraction of

all atoms. Specifically, for free bosons, the number of atoms in the condensate is

$$N_0 = N - 2.612\frac{V}{[\lambda(T)]^3} \ \ (T \leq T_c). \tag{2.5}$$

In the real world interaction exists among atoms. When the distance between atoms are much greater than the scattering length, or expressed as $na^3 \sim 0$ (n is the number density, a is the scattering length), the system can be approximated as non-interacting, and the above model applies.

2.2 Interacting Systems

Interaction is ubiquitous. In a system of multiple atoms, the number of interacting pairs grow as a factorial function of the number of atoms, and the complexity quickly becomes impossible to directly handle. Therefore physicists developed many-body theory to understand the collective behavior of atoms, which is the framework of all the following approximations.

The full Hamiltonian of the system is

$$\begin{aligned} H = &\int d^3x\ \hat{\Psi}^\dagger(\mathbf{x})[-\frac{\hbar^2\nabla^2}{2m} + V_{ext}(\mathbf{x})]\hat{\Psi}(\mathbf{x}) \\ &+ \frac{1}{2}\int d^3x\ d^3x'\ \hat{\Psi}^\dagger(\mathbf{x})\hat{\Psi}^\dagger(\mathbf{x}')V(\mathbf{x}'-\mathbf{x})\hat{\Psi}(\mathbf{x}')\hat{\Psi}(\mathbf{x}), \end{aligned} \tag{2.6}$$

where $\hat{\Psi}(\mathbf{x})$ and $\hat{\Psi}^\dagger(\mathbf{x})$ are the field operator, m is the atomic mass, V_{ext} is an external potential such as a lattice or a trap. For dilute atomic gases, the average separation between atoms is large, we can assume the two-body interaction $V(\mathbf{x}'-\mathbf{x})$ only exists on contact,

$$V(\mathbf{x}'-\mathbf{x}) = g\ \delta(\mathbf{x}'-\mathbf{x}), \tag{2.7}$$

where

$$g = \frac{4\pi a_s\hbar^2}{m}, \tag{2.8}$$

and a_s is the s-wave scattering length. Then the Hamiltonian becomes

$$H = \int d^3x\, \hat{\Psi}^\dagger(\mathbf{x})[-\frac{\hbar^2\nabla^2}{2m} + V_{ext}(\mathbf{x})]\hat{\Psi}(\mathbf{x}) + \frac{g}{2}\int d^3x\, \hat{\Psi}^\dagger(\mathbf{x})\hat{\Psi}^\dagger(\mathbf{x})\hat{\Psi}(\mathbf{x})\hat{\Psi}(\mathbf{x}). \quad (2.9)$$

It is usually very difficult to calculate many body systems using the full Hamiltonian Eq. 2.9. To save a tremendous amount of work, people found various approximations to simplify the problem. Which approximation to apply depends on whether the system is at zero temperature or finite temperature, and whether the interaction is strong or weak comparing to the kinetic energy. At low temperature and relatively weak interaction, the mean field theory is used to obtain sensible results about the physical system.

2.3 Interacting Systems: Mean Field Theory

2.3.1 Gross-Pitaevskii Equation

The basic idea of the mean field approach, proposed by Bogoliubov in 1947, is to explicitly separate the contribution from the condensate and the contribution from excited atoms in the field operator [21]

$$\hat{\Psi}(\mathbf{x}, t) = \Phi(\mathbf{x}, t) + \hat{\Psi}'(\mathbf{x}, t), \quad (2.10)$$

where $\Phi(\mathbf{x}, t)$ is defined as the expectation value of the field operator

$$\Phi(\mathbf{x}, t) \equiv \left\langle \hat{\Psi}(\mathbf{x}, t) \right\rangle, \quad (2.11)$$

which corresponds to the condensate, and $\hat{\Psi}'(\mathbf{x}, t)$ corresponds to the excited atoms.

We can think in terms of limiting cases. The two limiting cases are when $T > T_c$ and when $T = 0$. Above the critical temperature, no condensate exists, the gas is

all thermal, we have $\hat{\Psi}(\mathbf{x},t) = \hat{\Psi}'(\mathbf{x},t)$. At zero temperature, all atoms are at the ground state, so $\hat{\Psi}(\mathbf{x},t) = \Phi(\mathbf{x},t)$. For the latter case, the Schrödinger Equation becomes

$$[-\frac{\hbar^2\nabla^2}{2m} + V_{ext}(\mathbf{x}) + g\,|\Phi(\mathbf{x},t)|^2]\Phi(\mathbf{x},t) = i\hbar\frac{\partial}{\partial t}\Phi(\mathbf{x},t), \tag{2.12}$$

known as the Gross-Pitaevskii equation. This equation is the starting point for many mean-field calculations for $T \sim 0$ systems.

We can immediately get some understanding from Eq. 2.12. The density of atoms is

$$n(\mathbf{x},t) = |\Phi(\mathbf{x},t)|^2\,. \tag{2.13}$$

Since the kinetic term $-\frac{\hbar^2\nabla^2\Phi}{2m}$ is proportional to $\nabla^2\sqrt{n}$, the kinetic energy is more significant near the boundary. In a large system where the density distribution across the condensate does not vary drastically, it is acceptable to ignore the kinetic term. Then Eq. 2.12 yields for $\mu > V_{ext}$ (assuming no time dependence)

$$n(\mathbf{x}) = \frac{E - V_{ext}(\mathbf{x})}{g} = \frac{\mu - V_{ext}(\mathbf{x})}{g}, \tag{2.14}$$

where E is the energy of the ground state. In the last step, E is replaced by the chemical potential μ because at ground state they equal, as stated in Sec. 2.1. When $\mu < V_{ext}$, $n = 0$. This is called Thomas-Fermi approximation [21] or Local Density Approximation (LDA). LDA was first applied to cold bosons by [57]. We will make use of LDA in later chapters.

The difference of the Gross-Pitaevskii Equation from the non-interacting Schrödinger Equation is the additional non-linear interaction term which presents the mean interaction from all particles. The interaction is characterized by the interaction parameter g which can be positive or negative, depending on the sign of the s-wave scattering length a_s.

2.3.2 Bogoliubov Approximation

The Gross-Pitaevskii Equation is a zero-temperature theory. For systems at very low temperature, most of the atoms are expected to remain in the condensate, only a small fraction enter into excited states. The Bogoliubov Approximation applies to such low temperature systems[23].

Consider the grand canonical Hamiltonian

$$\hat{K} = \hat{H} - \mu\hat{N}, \tag{2.15}$$

where $\hat{H}$ is expressed in Eq. 2.6. In Bogoliubov approximation, the field operators is taken as the condensate part plus a small perturbation which represents the excited states.

$$\hat{\Psi}(\mathbf{r}, t) = \hat{\Psi}_0(\mathbf{r}, t) + \hat{\Psi}_1(\mathbf{r}, t). \tag{2.16}$$

The field operators can be expanded in single particle states in the momentum space,

$$\hat{\Psi}(\mathbf{r}, t) = \frac{1}{\sqrt{V}} \sum_{\mathbf{k}} \hat{a}_{\mathbf{k}}(t) e^{i\mathbf{k}\cdot\mathbf{r}}, \tag{2.17}$$

where an arbitrary time-dependent operator $\hat{O}(\mathbf{r}, t)$ is given by the Heisenberg picture

$$\hat{O}(\mathbf{r}, t) = e^{\hat{K}t/\hbar} \hat{O}(\mathbf{r}) e^{-\hat{K}t/\hbar}, \tag{2.18}$$

note that the t here is in fact the imaginary time $i\,t$. Assume the condensate is uniform and constant, Ψ_0 is independent of $\mathbf{r}$ and t, we have

$$\Psi_0 = \sqrt{n_0}, \tag{2.19}$$

where n_0 is the condensate density. Because $\hat{a}_0$ and $\hat{a}_0^\dagger$ has the following commutation relationship,

$$[\hat{a}_0, \hat{a}_0^\dagger] = 1 \ll N_0, \tag{2.20}$$

where N_0 is the total number of atoms in the condensate, we can approximate $\hat{a}_0$ and $\hat{a}_0^\dagger$ as $\sqrt{N_0}$. Therefore the field operators are

$$\hat{\Psi}(\mathbf{r}, t) = \hat{a}_0/\sqrt{V} + \hat{\Psi}_1(\mathbf{r}, t); \tag{2.21}$$

$$\hat{\Psi}^\dagger(\mathbf{r}, t) = \hat{a}_0^\dagger/\sqrt{V} + \hat{\Psi}_1^\dagger(\mathbf{r}, t). \tag{2.22}$$

This procedure is known as Bogoliubov prescription. The above substitutions become exact at the thermodynamic limit. The averaged condensed phase is, of course, non-zero, while the excited phase has a vanishing average.

$$\langle \Psi_0(\mathbf{r}, t) \rangle \neq 0; \tag{2.23}$$

$$\langle \Psi_1(\mathbf{r}, t) \rangle = 0. \tag{2.24}$$

With this approximation we can begin simplifying the system's Hamiltonian. From Equations 2.6 and 2.15, the grand canonical Hamiltonian $\hat{K}$ is

$$\hat{K} = \int d^3r \Psi^\dagger(\mathbf{r})[-\frac{\hbar^2}{2m}\nabla^2 - \mu]\Psi(\mathbf{r}) + \frac{1}{2}\int d^3r \int d^3r' \, \Psi^\dagger(\mathbf{r})\Psi^\dagger(\mathbf{r}')V(\mathbf{r}-\mathbf{r}')\Psi(\mathbf{r}')\Psi(\mathbf{r}). \tag{2.25}$$

With details relegated in Appendix. A, for the non-condensate part of $\hat{K}$ we arrive at

$$\hat{K} + \mu N_0 - E_0 = \sum_{\mathbf{k}} \hat{A}_{\mathbf{k}}^\dagger \hat{h}_{\mathbf{k}} \hat{A}_{\mathbf{k}}, \tag{2.26}$$

where the matrix operator is

$$\hat{A}_{\mathbf{k}} = \begin{pmatrix} \hat{a}_{\mathbf{k}} \\ \hat{a}^{\dagger}_{-\mathbf{k}} \end{pmatrix} \tag{2.27}$$

and $\hat{h}_{\mathbf{k}}$ is

$$\frac{1}{2}\begin{pmatrix} E_{\mathbf{k}} - \mu + n_0 V(0) + n_0 V(\mathbf{k}) & n_0 V(\mathbf{k}) \\ n_0 V(\mathbf{k}) & E_{\mathbf{k}} - \mu + n_0 V(0) + n_0 V(\mathbf{k}) \end{pmatrix}. \tag{2.28}$$

Here $V(\mathbf{k})$ and $V(0)$ are Fourier transformed interaction, as defined in Appendix. A.

From Hugenholtz-Pines theorem[23], the lowest order of chemical potential is

$$\mu = n_0 V(0). \tag{2.29}$$

2.3.3 Hartree Fock Approximation

Another mean field approach, which does not exclusively limited to a certain range of temperature, is the Hartree Fock Approximation. This approximation assumes a dependence of the system's self energy on the atomic density.

Consider a translationally invariant system (or at least having discrete translational invariance, such as in a periodic potential). The Dyson's Equation is

$$\begin{aligned} &G(\mathbf{r}, \mathbf{r}'; \tau, \tau') \\ =&G_0(\mathbf{r}, \mathbf{r}'; \tau, \tau') + \int d^3 r_1 d^3 r_2 d\tau_1 d\tau_2 \; G_0(\mathbf{r}, \mathbf{r}_1{}'; \tau, \tau_1)\Sigma(\mathbf{r}_1, \mathbf{r}_2; \tau_1, \tau_2)G(\mathbf{r}_2, \mathbf{r}'; \tau_2, \tau'), \end{aligned} \tag{2.30}$$

where G and G_0 are the Green's functions of spatial coordinates $\mathbf{r}$, $\mathbf{r}'$ and imaginary time τ, τ' respectively for the entire system and for the bare system (defined in Appendix. B), and Σ is the self energy characterizing the contribution from interaction.

On the other hand, we have

$$G(\mathbf{r},\mathbf{r}',\tau,\tau') = -\left\langle T_\tau \Psi(\mathbf{r},\tau)\Psi^\dagger(\mathbf{r}',\tau')T_\tau e^{-\int_0^\beta d\tau H_1(\tau)}\right\rangle, \tag{2.31}$$

where H_1 is expressed in the second term of Eq. 2.9. To derive the Hartree-Fock term, we expand to the first order (denoting $x = (\mathbf{r},\tau)$, and similarly for x' and x_1),

$$G(x,x') = -\left\langle T_\tau \Psi(x)\Psi^\dagger(x')[1-\frac{g}{2}\int dx_1\ \Psi^\dagger(x_1)\Psi^\dagger(x_1)\Psi(x_1)\Psi(x_1)]\right\rangle, \tag{2.32}$$

where the coupling constant $g = 4\pi\hbar^2 a_s/m$ has been defined in Sec. 2.2. In the above Green's function, there are two ways for $\Psi(x)$ to contract with the two $\Psi^\dagger(x_1)$ factors, and there are two ways for $\Psi^\dagger(x')$ to contract with the two $\Psi(x_1)$ factors. Therefore, with $G_0(x,x') = -\left\langle T_\tau \Psi(x)\Psi^\dagger(x')\right\rangle$, we have

$$G(x,x') = G_0(x,x') - 2g\int dx_1\ G_0(x,x_1)G_0(x_1,x_1)G_0(x_1,x'). \tag{2.33}$$

Comparing Eq. 2.33 with Eq. 2.30, we obtain

$$\Sigma(x_1,x_2) = -2gG_0(x_1,x_1)\delta(x_1-x_2). \tag{2.34}$$

Since $G_0(x_1,x_1) = -n(x_1)$, the boson density, we come to

$$\Sigma(x,x') = 2gn(x)\delta(x-x'), \tag{2.35}$$

namely, the Hartree-Fock Approximation.

In the Matsubara space, the Hartree-Fock Approximation is equivalently written as

$$\Sigma(\mathbf{r},\mathbf{r}';i\Omega_m) = 2gn(\mathbf{r})\delta(\mathbf{r}-\mathbf{r}'). \tag{2.36}$$

From Appendix. B, $\Sigma(\mathbf{r},\mathbf{r}';i\Omega_m)$ can be expanded in orthonormal basis

$$\Sigma(\mathbf{r},\mathbf{r}';i\Omega_m)=\sum_{nn'}\sum_{\mathbf{k}}\psi_{n\mathbf{k}}(\mathbf{r})\psi^*_{n'\mathbf{k}}(\mathbf{r}')\Sigma_{nn'}(\mathbf{k};i\Omega_m). \tag{2.37}$$

Using Eqs. 2.36 and 2.37, we have

$$\begin{aligned}&\int d^3rdr'^3\psi^*_{n_1\mathbf{k_0}}(\mathbf{r})\psi_{n_2\mathbf{k_0}}(\mathbf{r}')2gn(\mathbf{r})\delta(\mathbf{r}-\mathbf{r}')\\&=\sum_{nn'}\sum_{\mathbf{k}}\int d^3rdr'^3\psi^*_{n_1\mathbf{k_0}}(\mathbf{r})\psi_{n_2\mathbf{k_0}}(\mathbf{r}')\psi_{n\mathbf{k}}(\mathbf{r})\psi^*_{n'\mathbf{k}}(\mathbf{r}')\Sigma_{nn'}(\mathbf{k};i\Omega_m).\end{aligned} \tag{2.38}$$

(Note that $\Sigma(\mathbf{r},\mathbf{r}';i\Omega_m)$ is in the dimension of energy density, while $\Sigma_{nn'}(\mathbf{k};i\Omega_m)$ is in the dimension of energy.) Then, we use orthogonal relationship to obtain

$$\Sigma_{n_1n_2}(\mathbf{k};i\Omega_m)=2g\int d^3r\psi^*_{n_1\mathbf{k}}(\mathbf{r})\psi_{n_2\mathbf{k}}(\mathbf{r})n(\mathbf{r}). \tag{2.39}$$

In Appendix. B we have proved

$$\mathbf{G}(\mathbf{k};i\Omega_m)=\frac{1}{\mathbf{G}_0^{-1}(\mathbf{k};i\Omega_m)-\mathbf{\Sigma}(\mathbf{k};i\Omega_m)}. \tag{2.40}$$

Specially, for low temperature, we can make the single-band approximation to focus only on the lowest band

$$\begin{aligned}\mathbf{G}(\mathbf{k};i\Omega_m)\approx&G_{00}(\mathbf{k};i\Omega_m)\\=&\frac{1}{i\Omega_m-\varepsilon_{0\mathbf{k}}-\Sigma_{00}(\mathbf{k};i\Omega_m)},\end{aligned} \tag{2.41}$$

where the self energy for the lowest band is

$$\Sigma_{00}(\mathbf{k};i\Omega_m)=2g\int_V d^3r|\psi_{0\mathbf{k}}(\mathbf{r})|^2n(\mathbf{r}). \tag{2.42}$$

With the above discussion on the Hartree Fock approximated self energy, we can examine the total energy of the lowest band to see what role interaction effects play. The dispersions of the kinetic energy and the self energy of the lowest band can be expanded as:

$$\begin{aligned} E_{00}(\mathbf{k}) =& \varepsilon_{0\mathbf{k}} + \Sigma_{00}(\mathbf{k}) \\ =& \varepsilon_{0\mathbf{k}} \mid_{\mathbf{k}=0} + \nabla_{\mathbf{k}} \varepsilon_{0\mathbf{k}} \mid_{\mathbf{k}=0} \cdot \mathbf{k} + \frac{1}{2} \sum_{i,j} \frac{\partial^2 \varepsilon_{0\mathbf{k}}}{\partial k_i \partial k_j} \mid_{\mathbf{k}=0} k_i k_j + ... \\ &+ \Sigma_{00}(\mathbf{k}) \mid_{\mathbf{k}=0} + \nabla_{\mathbf{k}} \Sigma_{00}(\mathbf{k}) \mid_{\mathbf{k}=0} \cdot \mathbf{k} + \frac{1}{2} \sum_{i,j} \frac{\partial^2 \Sigma_{00}(\mathbf{k})}{\partial k_i \partial k_j} \mid_{\mathbf{k}=0} k_i k_j + ... \end{aligned} \tag{2.43}$$

Where $i, j = x, y, z$. First we look at the zeroth order. The zeroth order of the kinetic energy vanishes

$$\varepsilon_{0\mathbf{k}} = \frac{\hbar^2 \mathbf{k}^2}{2m} \mid_{\mathbf{k}=0} = 0. \tag{2.44}$$

For the first order, assuming $\mathbf{k} = 0$ is a minimum for both $\varepsilon_{0\mathbf{k}}$ and $\Sigma_{00}(\mathbf{k})$, both first order terms vanish. When neglecting higher orders in the expansion, we have

$$E_{00}(\mathbf{k}) \approx \frac{1}{2} \sum_{i,j} \frac{\partial^2 \varepsilon_{0\mathbf{k}}}{\partial k_i \partial k_j} \mid_{\mathbf{k}=0} k_i k_j + \Sigma_{00}(\mathbf{k}) \mid_{\mathbf{k}=0} + \frac{1}{2} \sum_{i,j} \frac{\partial^2 \Sigma_{00}(\mathbf{k})}{\partial k_i \partial k_j} \mid_{\mathbf{k}=0} k_i k_j. \tag{2.45}$$

Define effective masses

$$\frac{1}{m_{BANDij}} = \frac{1}{\hbar^2} \frac{\partial^2 \varepsilon_{0\mathbf{k}}}{\partial k_i \partial k_j} \mid_{\mathbf{k}=0}, \tag{2.46a}$$

$$\frac{1}{m_{INTij}} = \frac{1}{\hbar^2} \frac{\partial^2 \Sigma_{00}(\mathbf{k})}{\partial k_i \partial k_j} \mid_{\mathbf{k}=0}, \tag{2.46b}$$

$$\frac{1}{m^*{}_{ij}} = \frac{1}{\hbar^2} \frac{\partial^2 E_{00}(\mathbf{k})}{\partial k_i \partial k_j} \mid_{\mathbf{k}=0}, \tag{2.46c}$$

then

$$\sum_{i,j} \frac{\hbar^2}{2m^*_{ij}} k_i k_j \approx E_{00}(\mathbf{k}) \approx \sum_{i,j} \frac{\hbar^2}{2m_{BANDij}} k_i k_j + \Sigma_{00}(\mathbf{k}) \mid_{\mathbf{k}=0} + \sum_{i,j} \frac{\hbar^2}{2m_{INTij}} k_i k_j. \quad (2.47)$$

Assuming an isotropic system, the above equation can be simplified as

$$\frac{k^2}{2m^*} = \frac{k^2}{2m_{BAND}} + \frac{k^2}{2m_{INT}} + \frac{\Sigma_{00}(\mathbf{k}=\mathbf{0})}{\hbar^2}, \quad (2.48)$$

where k is near 0.

Note that for the Taylor expansion Eq. 2.43 to be valid, the dispersion and the self energy must be smooth, limiting the applicable range to the band bottom away from band gaps.

However, as argued by Ref. [58], the critical temperature of a BEC can not be shifted within the Hartree Fock Approximation. The reason is as follows: at the BEC transition, $\mathbf{G}^{-1}(\mathbf{k}=0; i\Omega_m=0)=0$, therefore $\Sigma(0,0)=0$, or rather, since the system is at the bottom of the band, $\Sigma(0,0)=\mu$. The contribution from Hartree Fock interaction term $2gn_0$ can be simply absorbed into the chemical potential, namely redefining

$$\frac{\hbar^2}{2m\zeta^2} = -(\mu - 2gn_0), \quad (2.49)$$

where ζ describes the mean field correlation length. In the mean field approximation, ζ becomes infinite at T_c, nullifying the contribution from $2gn_0$.

2.4 Interacting Systems: Bose-Hubbard Model

Mean field approximations usually don't work well when interaction becomes quite prominent. For cold atoms, a commonly studied type of strong interacting systems is such systems in period potentials, which we discuss in this section. The

reason to introduce periodic potentials is to mimic the crystalline lattice in electronic materials.. The mostly used periodic potential is optical lattices created by interfering lasers, which will be formally introduced in the next chapter.

As the interaction is tuned stronger and with deep lattice, atoms become more localized in the lattice sites. The single-site Wannier functions are the natural basis for the strong interacting limit. We can express the full Hamiltonian 2.6 by expanding the field operators in the Wannier basis $\hat{\Psi}(\mathbf{r}) = \sum_{i,\mathbf{R}} w_i(\mathbf{r} - \mathbf{R})\hat{b}_i(\mathbf{R})$ (refer to Appendix. C), where $w_i(\mathbf{r})$ is the Wannier function of the particle near lattice site i and $\mathbf{R}$ is a lattice vector. Writing all the integrals over Wannier functions as prefactors, we obtain the Bose-Hubbard model [22]

$$H = -J \sum_{<i,j>} (\hat{b}_i^\dagger \hat{b}_j + h.c.) + \frac{1}{2} U \sum_i \hat{n}_i(\hat{n}_i - 1) - \mu \hat{n}_i, \tag{2.50}$$

where J stands for the tunneling of atoms between sites, U is the on-site repulsion parameter, μ is the chemical potential. $\hat{b}_i$ and $\hat{b}_i^\dagger$ are bosonic field operators, $\hat{n}_i = \hat{b}_i^\dagger \hat{b}_i$ is the bosonic number operator. The angle brackets in $\langle i, j \rangle$ mean only nearest neighbors are included in the summation. Under the tight binding approximation, U and J can be expressed in forms that depends on the optical lattice depth V_0 [18]

$$U(V_0, a_s) = \sqrt{\frac{8}{\pi}} k_{ol}\, a_s\, E_{re} (\frac{V_0}{E_{re}})^{\frac{3}{4}}; \tag{2.51}$$

$$J(V_0) = \frac{4}{\sqrt{\pi}} E_{re} (\frac{V_0}{E_{re}})^{\frac{3}{4}} \exp[-2\sqrt{\frac{V_0}{E_{re}}}]. \tag{2.52}$$

Consider the $J = 0$ limit, the on-site energy is

$$E(n) = -\mu n + \frac{1}{2} U\, n(n-1), \tag{2.53}$$

where n is the on-site particle number. This value is minimized at

$$n = 1 + \mu/U, \tag{2.54}$$

rounded off to the nearest integer. When J is non-zero but still small ($U \gg J$), the tunneling term can be treated perturbatively, and can not overcome the energy cost to increase or decrease n by 1. Therefore there is a region for every n in the $\mu - J$ plane in which the number of particles per site is fixed [22]. This phase is called Mott insulator. Fig. $2-1$ shows the phase diagram of the superfluid-Mott insulator phase transition on the $\mu - J$ plane.

Mott insulator was first confirmed experimentally in 2002 [9]. By tuning the optical lattice depth V_0, experimentalists can adjust the ratio J/U to enter the Mott region. Fig. $2-2$ shows the absorption image of the matter wave interference. It was reported that at large lattice depth (large interaction), a complete lost of coherence was observed, suggesting the system has entered the Mott phase.

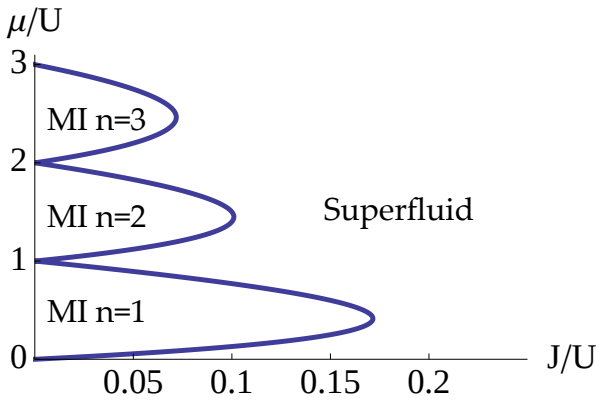

Figure 2-1: Superfluid transits into Mott insulator (MI) phase at strong interaction. Here μ is the chemical potential, J is the tunneling parameter, U is the repulsive interaction. The Mott region is in the shape of lobes, in each lobe only a certain integer number of atoms are allowed per site.

Our research goal, however, is to find a formalism that studies interacting systems using less approximation than the Bose-Hubbard model. Since Bose-Hubbard model only applies for the large interaction, deep lattice regime, effects from weak

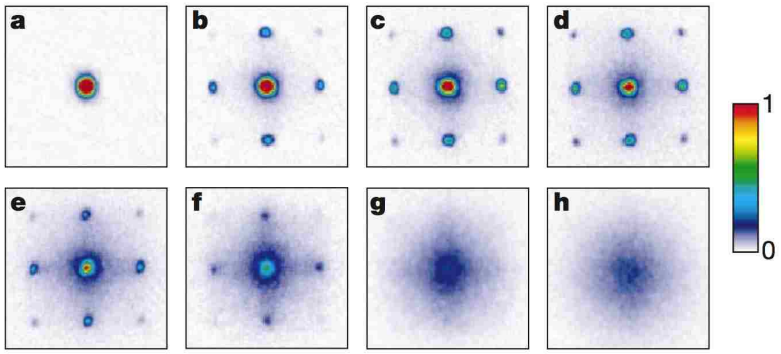

Figure 2-2: The absorption images of rubidium-87 atoms after time-of-flight expansion. The optical lattice depths V_0 for these images are: a, 0 E_{re}; b, 3 E_{re}; c, 7 E_{re}; d, 10E_{re}; e, 13E_{re}; f, 14E_{re}; g, 16E_{re}; h, 20E_{re}. E_{re} is the recoil energy. The authors report a trend into incoherence after $V_0 = 13E_{re}$, and a complete lost of coherence after 22E_{re}. This suggests a transition from superfluid into the Mott insulator phase. Images are taken from Ref. [9].

and medium range interactions may be explained well within mean field criteria. Therefore we choose studying Mathieu Equation, the natural and immediate description for the eigenstates of cold atoms in an optical lattice. Such efforts will be elaborated in Chapter 3.

2.5 Interacting Spinor BEC

In previous sections, there was only one inter-atomic interaction among the same species. In this section, we study interacting spinor BEC systems, in which we need to consider multiple types of interactions between different species.

We choose spin-1 Rubidium, a common choice in atomic experiments, as the subject of our study. The atom-atom interaction is described in the following interaction Hamiltonian[59]

$$\mathcal{H}_{int} = \frac{1}{2}\int d^3r\, [c_0 : \psi_a{}^\dagger \psi_a \psi_{a'}{}^\dagger \psi_{a'} : + c_2 : \psi_a{}^\dagger \mathbf{F}_{ab} \psi_b \cdot \psi_{a'}{}^\dagger \mathbf{F}_{a'b'} \psi_{b'} :], \tag{2.55}$$

where a and b are indices summing over $m = -1, 0, 1$, c_0 and c_2 are interaction parameters, and the Hamiltonian is in normal ordering, indicated by the semi-colons. Here we only discuss a two state subspace, essentially equivalent to the spin-$\frac{1}{2}$ space, projected from this spin-1 space. When projected into $m = -1, 0$ states, we have for the first term in Eq. 2.55,

$$\psi_{a'}{}^{\dagger}\psi_{a'} = \psi_1{}^{\dagger}\psi_1 + \psi_0{}^{\dagger}\psi_0 + \psi_{-1}{}^{\dagger}\psi_{-1} = \Psi_{\uparrow}{}^{\dagger}\Psi_{\uparrow} + \Psi_{\downarrow}{}^{\dagger}\Psi_{\downarrow} = n_{\uparrow} + n_{\downarrow}, \tag{2.56}$$

where $m = -1,\ 0$ states have been relabeled as $|\downarrow\rangle$ and $|\uparrow\rangle$, respectively, and $\psi_1{}^{\dagger}\psi_1$ is simply dropped. In experiments, this can be done using a magnetic field by uplifting the energy of $m = 1$ from the other two states so much that it becomes almost irrelevant. So the first term in Eq. 2.55 becomes

$$\mathcal{H}_{int}|_{c_0} = \frac{c_0}{2}\int d^3r\ :(n_{\uparrow} + n_{\downarrow})^2: . \tag{2.57}$$

For the second term of Eq. 2.55, we first consider in the 3-state space

$$\begin{aligned}
&\psi_a{}^{\dagger}\mathbf{F}_{ab}\psi_b \\
&= \begin{pmatrix} \psi_1{}^{\dagger} \\ \psi_0{}^{\dagger} \\ \psi_{-1}{}^{\dagger} \end{pmatrix}^T \left[\frac{\hat{e}_x}{\sqrt{2}}\begin{pmatrix} 0 & 1 & 0 \\ 1 & 0 & 1 \\ 0 & 1 & 0 \end{pmatrix} + \frac{\hat{e}_y}{\sqrt{2}}\begin{pmatrix} 0 & -i & 0 \\ i & 0 & i \\ 0 & i & 0 \end{pmatrix} + \frac{\hat{e}_z}{\sqrt{2}}\begin{pmatrix} 1 & 0 & 0 \\ 0 & 0 & 0 \\ 0 & 0 & -1 \end{pmatrix}\right]\begin{pmatrix} \psi_1 \\ \psi_0 \\ \psi_{-1} \end{pmatrix},
\end{aligned} \tag{2.58}$$

which, after projection into the $m = -1, 0$ subspace, becomes

$$\psi_a{}^{\dagger}\mathbf{F}_{ab}\psi_b|_{projected} = \frac{\hat{\mathbf{e}}_x}{\sqrt{2}}(\Psi_{\downarrow}{}^{\dagger}\Psi_{\uparrow} + \Psi_{\uparrow}{}^{\dagger}\Psi_{\downarrow}) + \frac{\hat{\mathbf{e}}_y}{\sqrt{2}}(\Psi_{\downarrow}{}^{\dagger}\Psi_{\uparrow} - \Psi_{\uparrow}{}^{\dagger}\Psi_{\downarrow}) - \hat{\mathbf{e}}_z\Psi_{\downarrow}{}^{\dagger}\Psi_{\downarrow}. \tag{2.59}$$

Therefore, the second term of Eq. 2.55 can be simplified as

$$\mathcal{H}_{int}|_{c_2} = \frac{c_2}{2}\int d^3r \ : (2n_\uparrow n_\downarrow + {n_\downarrow}^2) : . \tag{2.60}$$

And finally, with both terms calculated, the total interaction Hamiltonian is

$$\mathcal{H}_{int} = \frac{1}{2}\int d^3r \ [c_0(n_\uparrow + n_\downarrow)^2 + c_2(2n_\uparrow n_\downarrow + {n_\downarrow}^2)]. \tag{2.61}$$

We estimate the interaction parameters c_0 and c_2 to see which term is dominant in realistic spin-1 ^{87}Rb atomic systems. The parameters c_0 and c_2 are related to the scattering lengths a_F (with $F = 0, 2$ being the total spin) via [60].

$$c_0 = \frac{4\pi\hbar^2}{M}\frac{1}{3}(a_0 + 2a_2); \tag{2.62}$$

$$c_2 = \frac{4\pi\hbar^2}{M}\frac{1}{3}(a_2 - a_0), \tag{2.63}$$

where M is the atomic mass of ^{87}Rb. The values of a_0 and a_2 are very close. Theoretical values quoted by [60] are

$$a_0 = 101.78\ a_B; \tag{2.64}$$

$$a_2 = 100.40\ a_B, \tag{2.65}$$

which gives

$$a_2 - a_0 = -1.38\ a_B, \tag{2.66}$$

and their experimental measurement is

$$a_2 - a_0 = -1.07\ a_B, \tag{2.67}$$

where $a_B = 5.29177 \times 10^{-11}$m is the Bohr radius, making c_0 about two orders of magnitude larger than c_2, with an opposite sign. This means in the interaction Hamiltonian Eq. 2.55, the first term provides repulsion, while the second term provides attraction. Moreover, if the number of the two species are not far off, the repulsive force is going to be overwhelmingly dominant. This estimation is atom-specific, the situation will be different if the spinor BEC is made by another kind of atom.

The discussion in this section illustrates the interaction effects in a spinor BEC system, which is potentially much richer than that in a single species BEC, since the competition of more than one interactions can bring in new phases and new matter. In Chapter 6, we will study interacting Spin-Orbit Coupled bosonic systems based on our discussion in this section.

CHAPTER 3
BOSONS IN AN OPTICAL LATTICE

The introduction of a periodic optical lattice potential into a system of cold bosons has a clear motivation: such a periodic potential mimics the crystalline lattice potential seen by electrons in a solid. Thus, although bosonic atoms do not exhibit the Pauli principle like electrons (a fundamental distinction), bosons in a periodic optical lattice can still exhibit many-body phases similar to those of electrons in a crystal.

Optical lattices can bring many changes to the properties of bosons: transition temperatures, condensation fractions, density variations, and they also contribute to the emergence of new phases. Experimental interests on the phase transitions in an optical lattice environment have been strong. Previous experiments include Refs. [9, 24, 25, 26]. As introduced in the preceding chapter, in a lattice, strongly-interacting bosons in a superfluid can enter the Mott insulator phase . In Ref. [26], Trotzky et al. measured the superfluid to normal phase transitions in the regime near the Mott phase, and found that the superfluid critical temperature is suppressed near the Mott regime.

In this chapter, we will discuss bosons in an optical lattice for several cases. We start from introducing the concept of the optical lattice. In the next section we discuss the solution for non-interacting bosons in an optical lattice based on Mathieu functions, and calculate the superfluid transition temperature of bosons in an optical lattice as a function of optical lattice depth. Then we investigate the signature of the phase transition in terms of the density of the cloud after it is released from the trap. Finally we talk about the effects of the inter-atomic interaction on this system. We are most interested in understanding to what extent the higher bands

contribute in phase transition, and how significantly (or not significantly) interaction alters the transition conditions. In this chapter and Chapter 4, we will make frequent comparison with the experimental results in Ref. [26].

3.1 Optical Lattice

To rationalize the use of the optical lattice, one may think about a typical condensed matter system, in which charge carriers like electrons move in a periodic Coulomb potential created by nuclei. To obtain behaviors as rich, we need a similar setting for neutral atoms. An optical lattice produces an artificial periodic potential for cold atoms by using the interference of light.

The optical lattice is made by a set of standing waves, usually formed by interference between two counter-propagating laser beams on each dimension (See Fig. $3-1$) [17],

$$\mathbf{E}(\mathbf{r}) = \mathbf{E}_0[e^{i(\mathbf{k}_{ol}\cdot\mathbf{r}-\omega t)} + h.c.] - \mathbf{E}_0[e^{i(\mathbf{k}_{ol}\cdot\mathbf{r}+\omega t)} + h.c.] = 4\mathbf{E}_0 \sin(\mathbf{k}_{ol}\cdot\mathbf{r}) \sin\omega t, \quad (3.1)$$

where ω is the frequency of the field, $\mathbf{k}_{ol}$ is the wave vector of the field. Since the centers-of-mass of atoms are on a much slower time scale comparing with the laser frequency ω, the atoms can be considered as in a time-averaged field. This field exerts on the atoms the dipole force [18],

$$\mathbf{F} \propto \boldsymbol{\nabla}(|\mathbf{E}(\mathbf{r})|^2), \quad (3.2)$$

therefore on each dimension the single wave creates a potential

$$V(x) = V_0 \sin^2(k_{ol}x), \quad (3.3)$$

where V_0 is the lattice depth. In 3-D the optical lattice potential is

$$V(\mathbf{r}) = V_0[\sin^2(k_{ol}x) + \sin^2(k_{ol}y) + \sin^2(k_{ol}z)], \tag{3.4}$$

where we assumed isotropy of the optical lattice. The micro-wells in the standing wave are called sites, in which atoms tend to situate themselves. In practice an extra magnetic trap is sometimes utilized to confine the atomic gas. Note that we do not take this external trapping potential into consideration in this and the next chapters. Instead, we consider a gas in a square-well potential.

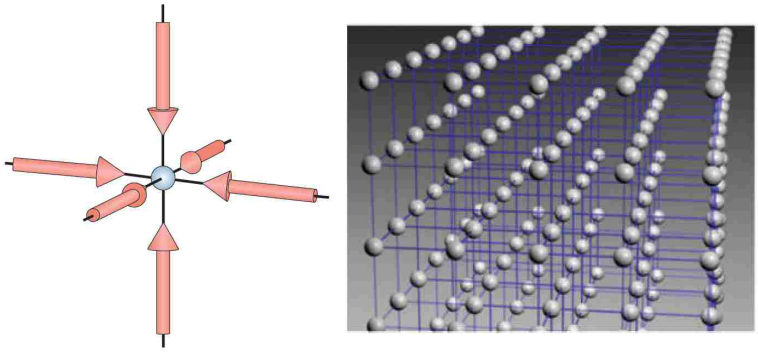

Figure 3-1: Standing wave is created from interference of two counter-propagating laser beams on each dimension, producing an optical lattice. A 3-D optical lattice is shown here. Graph is taken from Ref. [17].

3.2 Superfluid Transition of Bosons in an Optical Lattice

Now we can extend the calculation for the critical condition in Sec. 2.1 for the case when an optical lattice is involved. We aim to find the distinctive thermodynamics and critical behavior for bosons when an optical lattice is present.

Previously we focused on the critical temperature T_c. The lattice depth V_0 affects the phase of atoms, therefore we can define the critical lattice depth V_{0_c} when the atoms cross the phase boundary as the lattice depth is continuously tuned larger. The BEC transition is similar to the no lattice case, but now we need the energy

eigenvalues of the bosons in a periodic potential. Once we know the energy eigenvalues, T_c or V_{0_c} is given by the number equation Eq. 2.1 by letting $\mu = 0$. After that, we can again make use of Eq. 2.1 to find the N_0 and the μ curves, if the filling $f = N/N_s$ (the number of atoms per site), where N_s is the number of sites, is given.

Consider a group of bosons that are placed within a finite volume whose size is L on each dimension, and an isotropic optical lattice potential is imposed.

$$V = V_0(\cos^2 k_{ol}x + \cos^2 k_{ol}y + \cos^2 k_{ol}z - \frac{3}{2}), \tag{3.5}$$

where V_0 is the lattice depth, and

$$k_{ol} = \frac{2\pi}{\lambda}, \tag{3.6}$$

where λ is the wavelength of the laser used to construct the optical lattice. The $3/2$ constant substracted in Eq. 3.5 ensures the Fourier transform of the lattice $V(\mathbf{k} = 0) = 0$. Since each period contains two sites, the number of sites

$$N_s = \left(\frac{2L}{\lambda}\right)^d = \left(\frac{L\,k_{ol}}{\pi}\right)^d, \tag{3.7}$$

where d is the dimension. The Schrödinger Equation for bosons in this 3D optical lattice is

$$(-\frac{\hbar^2}{2m}\nabla^2 + V)\Phi = E\Phi, \tag{3.8}$$

where E is the total energy, Φ is the wave function and $\nabla = \frac{\partial}{\partial x}\hat{\mathbf{x}} + \frac{\partial}{\partial y}\hat{\mathbf{y}} + \frac{\partial}{\partial z}\hat{\mathbf{z}}$. To solve the 3D Schrödinger Equation Eq. 3.8, it is sufficient to start with the corresponding 1D case.

1D solution Under 1D, the optical lattice potential is

$$V = V_0(\cos^2 k_{ol}x - \frac{1}{2}). \tag{3.9}$$

Schrödinger equation converts to the well-known Mathieu Equation after some algebra:

$$\frac{d^2\phi}{du^2} + (a - 2q\cos 2u)\phi = 0, \tag{3.10}$$

where ϕ is the 1D wave function, a is the eigenvalue

$$a = \frac{\varepsilon}{E_{re}}, \tag{3.11}$$

q is the normalized lattice depth

$$q = \frac{V_0}{4E_{re}}, \tag{3.12}$$

and ε is the energy on this axis. Both a and q are dimensionless. The spatial variable (on x axis), also dimensionless, is $u_x = k_{ol}x$, and the recoil energy is defined as $E_{re} = \hbar^2 k_{ol}^2/2m$, which is used to scale all quantities that have an energy dimension.

Mathieu Equation (Eq. 3.10) has the following solution:

$$y = C_1\,\mathrm{ce}(a, q, u) + C_2\,\mathrm{se}(a, q, u), \tag{3.13}$$

where C_1 and C_2 are constants, $\mathrm{ce}(a, q, u)$ is the Mathieu even function, which is even symmetric (analogous to cosine). $\mathrm{se}(a, q, u)$ is the Mathieu odd function (analogous to sine).

The system's dispersion, obtained as the eigenvalue of the Mathieu Equation, can be expressed in terms of the Mathieu Characteristic Function, $a_k(q)$ for the even

Mathieu function, and $b_k(q)$ for the odd Mathieu function, where k is the quasi-momentum, with details given in Appendix D. Fig. $3-2$ compares the Characteristic Function when $V_0/4E_{re} = 0,\ 0.5,\ 1$. We see that the ground state energy at $k = 0$ becomes lower for larger lattice amplitude, indicating that the bosons are able to arrange themselves to lower the energy at large lattice depth.

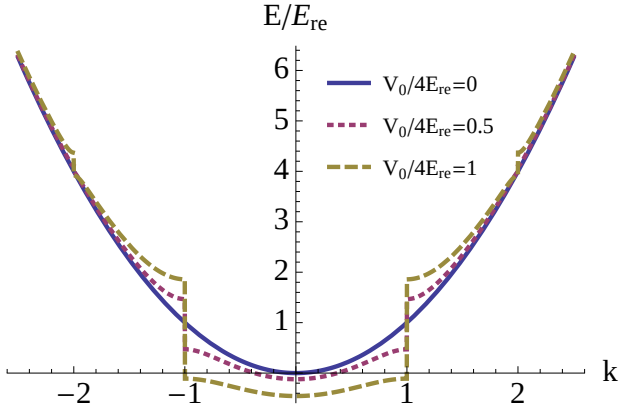

Figure 3-2: Mathieu Characteristic Function for the even Mathieu function gives the dispersion $E(k)$. Here $V_0/4E_{re} = 1, 0.5, 0$. The ground state energy (the bottom of the curves) is lowered as the optical lattice potential V_0 increases. The Characteristic Function is reduced to a parabola when $V_0 = 0$.

Also in Fig. $3-2$, the curvature of the Characteristic Function changes with q as well. For example, the curves at $k = 0$ open up more with increasing q. We define effective mass $m^* = \hbar^2/(\partial^2 E/\partial^2 k)$ to describe the curvature of dispersions, larger effective masses indicate smaller curvature. Here the effective mass is

$$m^*(q) = \frac{\hbar^2}{\partial^2\varepsilon/\partial^2 k} = \frac{\hbar^2}{E_{re}\,\partial^2 a_\nu/\partial^2 k} = \frac{{k_{ol}}^2}{E_{re}}\frac{\hbar^2}{\partial^2 a_\nu/\partial^2\nu} = \frac{2}{\partial^2 a_\nu(q)/\partial^2\nu}m. \tag{3.14}$$

Fig $3-3$ shows the effective mass increases with lattice depth. In particular, when $q = 0$ the effective mass starts at $1m$, agreeing with that of a parabola. This follows from that the effect of increasing optical lattice depth is to induce spatial

variations of the local boson density. Since the bosons are trapped in the local lattice potential minima, making it harder for them to move. This is represented, physically, by an increased effective mass.

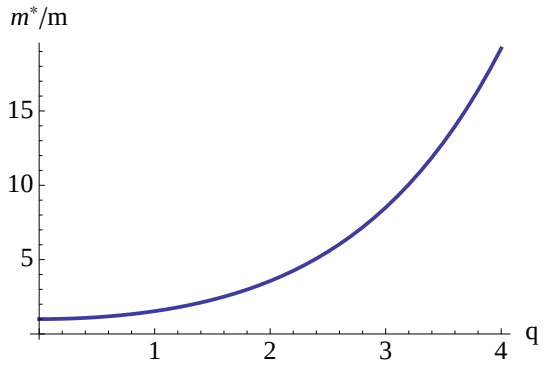

Figure 3-3: The effective mass (in units of the real atomic mass) increases with lattice depth, describing the dispersion when optical lattice is present.

Now we are able to treat the BEC transition when optical lattices are present. Using the solution to the 1D Mathieu Equation, we obtain the single particle solution

$$\Phi = \prod_{i=1}^{d} \phi(a_i, q, u_i), \tag{3.15}$$

which is a product of the 1-D Mathieu equation solutions in each dimension. The total energy is

$$E = \sum_{i=1}^{d} \varepsilon_i = \sum_{i=1}^{d} a_i E_{re}. \tag{3.16}$$

When E_n is given by the Mathieu Characteristic functions, the number equation Eq. 2.1 becomes

$$\begin{aligned} N = &\sum_{\nu_1,\ldots,\nu_d} \frac{1}{\exp[\beta E_{re}(a_{\nu_1} + \ldots + a_{\nu_d} - \mu/E_{re})] - 1} \\ =&N_s \int d\nu_1 \ldots d\nu_d \, \frac{1}{\exp[\beta E_{re}(a_{\nu_1} + \ldots + a_{\nu_d} - \mu/E_{re})] - 1}, \end{aligned} \tag{3.17}$$

where in the last step the continuum limit is applied. We can solve for the superfluid transition temperature T_c from Eq. 3.17.

Because the particle numbers are always positive, it is required that

$$\mu / E_{re} \leq \sum_{\nu_1..\nu_i..\nu_d} a_{\nu_i} = d\, a_0(q), \tag{3.18}$$

where we have replaced the eigenvalues a with Characteristic Function $a_\nu(q)$, and $a_0(q)$ refers to the Characteristic Function's minimum at $\nu = 0$. $a_\nu(q)$ and $b_\nu(q)$ are equivalent at non-integer ν's, but $a_\nu(q)$ is well defined at $\nu = 0$, which makes it a better choice than $b_\nu(q)$.

Since no BEC would be formed in lower dimensions (the integral are divergent, as our calculations show), we will work in 3D only. The system becomes critical when μ reaches its maximum, i.e. the bottom of the bands. So Eq. 3.17 becomes

$$f = \int_\epsilon^\Lambda d\nu_1 d\nu_2 d\nu_3 \, \frac{1}{\exp[E_{re}(a_{\nu_1}(q) + a_{\nu_2}(q) + a_{\nu_3}(q) - 3a_0(q))/k_B T_c] - 1}, \tag{3.19}$$

where $f = N/N_s$ is the filling for atoms *not* in the condensate, which at the critical point equals the total filling, and Λ and ϵ are respectively the upper and lower limits for the integral. To ensure our choices of these limits don't affect the results, we did a precision test, included as Appendix. F.

Next, we will numerically solve Eq. 3.19 to obtain results for the transition temperature for varying optical lattice depth $q = V_0/4E_{re}$.

3.3 BEC Transition Results

3.3.1 Unit Filling $f = 1$

First we analyze the phase transition when the atom filling f is set at 1. As we discussed above, we can solve the number equation Eq. 3.19 to obtain the critical temperature T_c if the filling is given. Using the parameter ranges from the precision tests, we obtain the following results.

Fig. $3-4$ shows the change of T_c as a function of the optical lattice depth q, the decreasing trend is due to that deeper lattice weakens the coherence of BEC. The critical temperature at $q = 0$ (the y-intercept) agrees with Eq. 2.3, the original Einstein's result with no optical lattice.

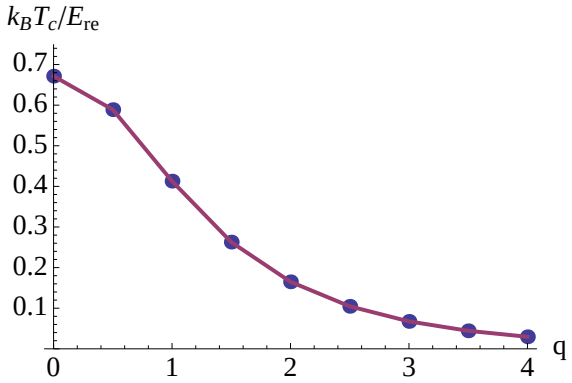

Figure 3-4: The BEC transition temperature decreases with deeper optical lattice, as solved from Eq. 3.19. The plot assumes unit filling. Here $\epsilon = 0.00001$, Λ=5, `MaxRecursion` is automatically set. (See Precision Control in Appendix F).

3.3.2 Multiple Filling $f > 1$

In the following calculation, we still work in the reversed way: assume a critical temperature first, then calculate the filling Eq. 3.19. This is because finding T_c as a root from a numerical integral is computationally challenging.

Now we relax the unit filling requirement and explore larger filling regimes. We examine the relationship between the filling (or density) and the critical temperature (i.e. f vs. T_c) under different q values.

Fig. $3-5$ shows for deeper lattice it requires a lower critical temperature for the same filling (consistent with Fig. $3-4$); and for the same temperature, deeper lattices lead to larger filling. The $q = 0$ curve agrees with Einstein's $n \propto {T_c}^{3/2}$ result for free boson gas.

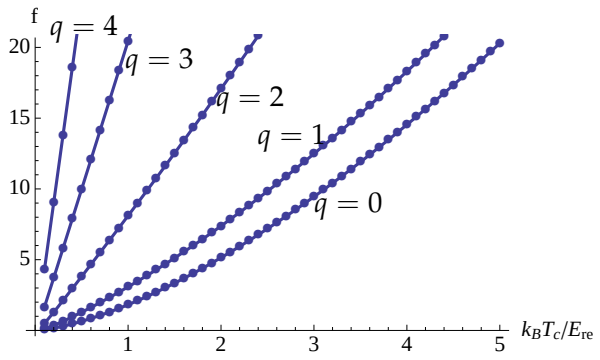

Figure 3-5: This figure shows the trend of the filling f with the critical temperature T_c under different lattice depths. From right to left: $q = 0$, $q = 1$, $q = 2$, $q = 3$, $q = 4$, where $q = V_0/4E_{re}$. Here we integrate between $\epsilon = 0.000001$, $\Lambda = 5$, using `MaxRecursion=4`. We can see for a deeper lattice, it requires a lower critical temperature for the same filling (consistent with Fig. $3-4$); and for the same temperature, deeper lattices lead to larger filling.

3.3.3 In Comparison: Mathieu Approach and Approximating with Effective Mass

In Fig. $3-5$ we calculated the density's trend with the critical temperature directly from the number equation (by using Mathieu function), using brutal numerical force. The Einstein's simple theoretical relationship between the particle density and the critical temperature, Eq. 2.2, is derived with the bare system dispersion, in which the particle is described by its bare mass. When optical lattice is present, we know that the dispersion is altered with the bare mass substituted by an effective mass, namely, $m^*/m = 2(\partial^2 a_\nu/\partial^2 \nu)^{-1}$, from Eq. 3.14. So if the effective mass approximation holds, then the $N - T_c$ relationship $N = 2.612\, V/[\lambda(T_c)]^3$ (Eq. 2.2) will stay untouched, with the de Broglie wavelength now includes the effective mass

$$\lambda(T) = \sqrt{\frac{2\pi\hbar^2}{m^* k_B T}}. \tag{3.20}$$

Therefore we can plot (1) the densities (or fillings) from numerical integrals in Eq. 3.19 and (2) the densities predicted by Eq. 2.2 with effective masses together, as shown in Fig. $3-6$.

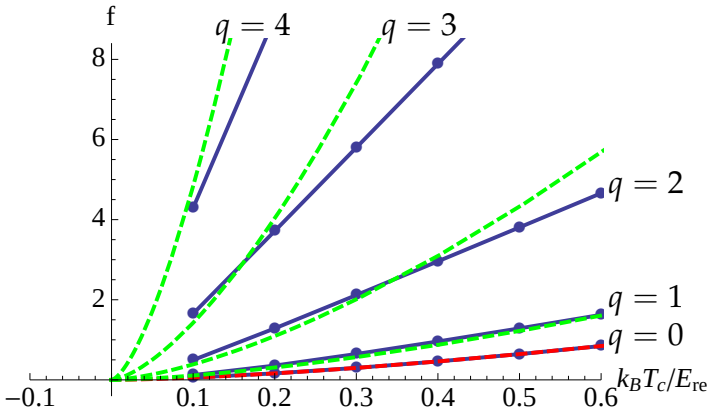

Figure 3-6: We show here the density's (or the filling's) relationship with the critical temperature: the fillings numerically calculated from integrating the number equation are shown in dark blue solid lines, while the fillings from Einstein's theory result $N \propto T_c^{3/2}$ with the original particle mass substituted by the effective mass are shown in red (for $q = 0$) and green (from right to left: $q = 1, 2, 3, 4$) dashed lines. One can see that the overlaid Mathieu and effective mass results agree better at small filling and low critical temperature, but become very different at large filling and high critical temperature.

We can clearly see in Fig. $3-6$ that, the number equation numerical result and the effective mass theoretical result agree better at small T_c and small fillings, but differ a lot at large T_c and large fillings. To look into this we replot with denser sampling rate at the small filling range, as shown in Fig. $3-7$ and Fig. $3-8$. The effective mass theoretical result (dashed line in green) agrees with the number equation numerical result very well at very small filling (Region 1), then becomes lower (Region 2), crosses with the latter (Region 3), and finally departs from the latter (Region 4).

Comparing the agreement of the two curves provides us insight on which models hold in certain regions. In Region 1, at small filling the dispersion is very similar to parabola, and the effective mass approximation is valid. In Region 2, there are corrections to the effective mass approximation, resulting in $T_{c1} < T_{c2}$ for the same filling, where T_{c1} is the numerical result from the number equation (more realistic),

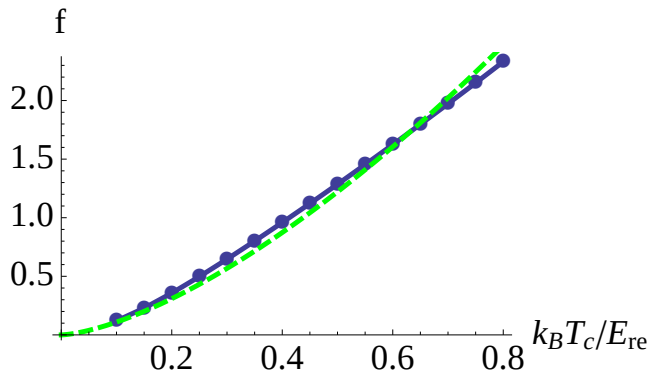

Figure 3-7: At intermediate T_c and fillings (around f=1), the effective mass theoretical result (dashed line in green) is slightly lower than the number equation numerical result (solid line in blue with data points marked as dots), until it crosses with the latter. Here the optical lattice depth $q = 1$, $\epsilon = 0.000001$, $\Lambda = 5$, `MaxRecursion=4`.

and T_{c2} is from the simple effective mass approximation. In Region 3, the two results begin to show significant deviation, indicating higher bands now start to play a role. And in Region 4, the single band approximation completely fails.

The trend can be explained by in Fig. $3-9$ and Fig. $3-10$. The Mathieu Characteristic Function and the free atom dispersion (parabola) agree better in small quasi-momentum ν values. As ν becomes larger, there are more states in the Mathieu dispersion than the free gas dispersion, allowing larger fillings, which corresponds to Region 2. But the jump at integer ν values reduces the possibility of atoms filling the second band, at which point the f-T_c curve is suppressed and eventually crosses with the free particle dispersion in Region 3. As ν further increases the Mathieu Characteristic Function outgrows the free particle dispersion significantly, and thus the f-T_c curve is further suppressed.

3.3.4 Effect of Higher Bands

To further investigate the condensation thermodynamics when higher bands are included (indicated by Λ), we plot the density-T_c relationships when a certain number of bands are included in Fig. $3-11$ and Fig. $3-12$.

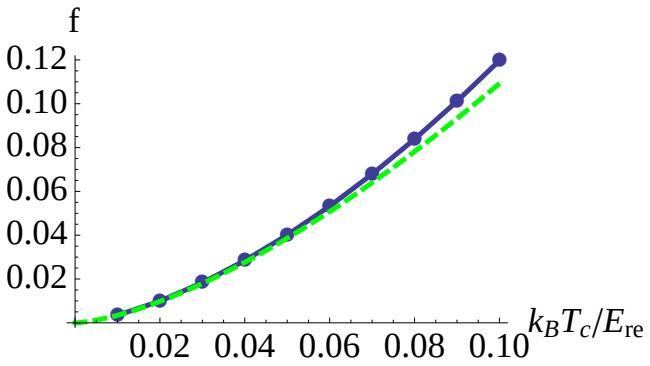

Figure 3-8: At very small critical temperatures and fillings, the effective mass theoretical result (dashed line in green) agrees well with the number equation numerical result (solid line in blue with data points marked as dots), then becomes slightly lower than the latter. Here the optical lattice depth $q = 1$, $\epsilon = 0.000001$, $\Lambda = 5$, `MaxRecursion`=4.

How we obtain the two figures is the same as we did for Fig. $3-5$ through Fig. $3-8$. For an assumed critical temperature, we calculate the corresponding filling. We can see in both plots that as we get into the large filling / high critical temperature regime, more bands need to be included. For example, at unit filling, single band approximation is sufficient because including more bands does not make a difference in Fig. $3-11$. But at $f = 5$, there is already a visible difference between including only the first band and including two bands, and a deviation between $\Lambda = 2$ and $\Lambda = 3$ is also in the making. The splitting between density-temperature curves is verified up to $f = 70$, and there is no reason to believe this trend would stop.

This trend shows that at large filling bosons occupy higher bands when they condensate, therefore we must take higher bands into consideration when studying large filling non-interacting and interacting systems.

3.4 Free Expansion

After calculating the phase transition of bosons in an optical lattice, we aim at theoretical prediction for the nature of the condensate. The superfluid state of

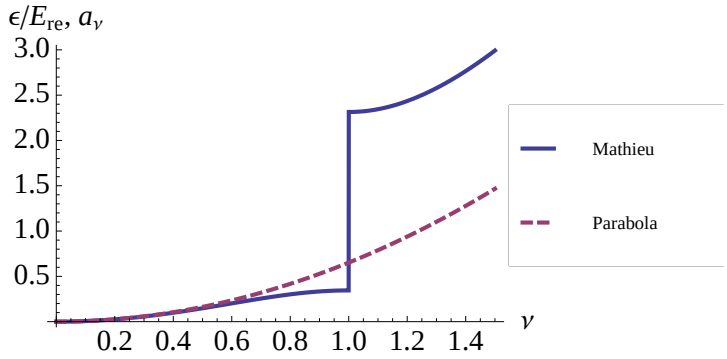

Figure 3-9: The Mathieu Characteristic Function resembles free particle dispersion (parabola, shown in dashed line) in the low energy regimes, and the BEC thermodynamics can be well described by the Einstein result with a straightforward effective mass approximation. As the quasi-momentum ν grows, Mathieu Characteristic Function deviates from a parabola, and corrections have to be made. At $\nu = 1$, Mathieu Characteristic Function has a jump, at which point the single band approximation fails.

bosons is usually shown in experiments by absorption imaging of the freely expanded cloud. In this process, the trapping potential is abruptly turned off, the atomic gas undergoes a period of time-of-flight free expansion. The absorption image provides information about the density profile, which is related to the initial momentum distribution. Atoms that are initially of the same state will gather together in the real space, therefore density peaks in the image indicate Bose-Einstein

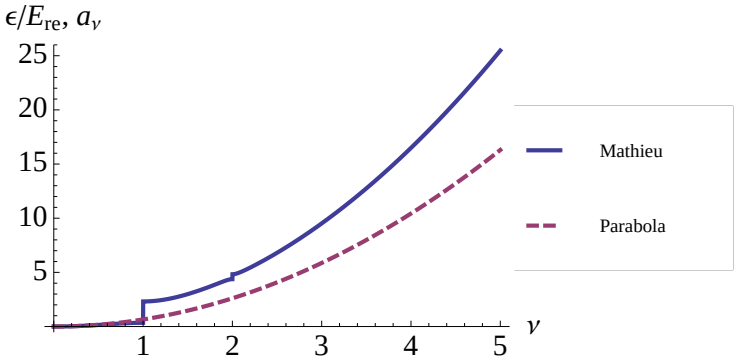

Figure 3-10: Despite agreement in lower bands (indicated by small quasi-momentum ν), the Mathieu Characteristic Function is overwhelmingly larger than the free particle dispersion for higher energy and larger bands.

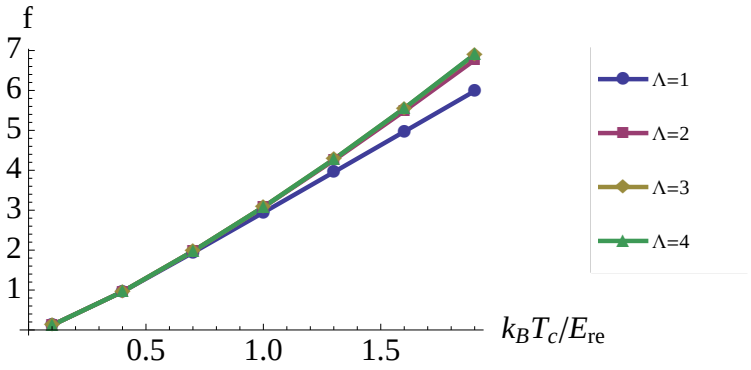

Figure 3-11: This graph shows how the calculated density increases with the critical temperature when different number of bands are included, examining the stability of the particle number integral against inclusion of higher bands. The calculated density-critical temperature dependence including the first band, the first 2 bands, 3 bands and 4 bands are shown here. As the filling and the critical temperature both increase, there are splitting between the lines, indicating part of the particles are already in the higher band, thus it is necessary to include that band. Here the lattice depth $q = V_0/4E_{re} = 1$.

condensate. In this section we show in a concise manner how to calculate the density profile after free expansion. Detailed steps of the derivation are provided in Appendix G.

Assume the trapping potential is turned off at $t = 0$. The time dependent density

$$n(\mathbf{r}, t) = \mathrm{Tr}\rho_{\mathcal{H}}(t)\hat{n}(\mathbf{r}) = \mathrm{Tr}\rho_{\mathcal{H}}(t)\hat{\Phi}^{\dagger}(\mathbf{r})\hat{\Phi}(\mathbf{r}), \tag{3.21}$$

where $\hat{\Phi}(\mathbf{r})$ and $\hat{\Phi}^{\dagger}(\mathbf{r})$ are field operators, $\rho_{\mathcal{H}}$ is the density matrix for the time dependent Hamiltonian which is written as

$$\mathcal{H}(t) = H_0 + \Theta(-t)H_{trap}, \tag{3.22}$$

where

$$\Theta(t) = \begin{cases} 0, & (t \leq 0); \\ 1, & (t > 0). \end{cases} \tag{3.23}$$

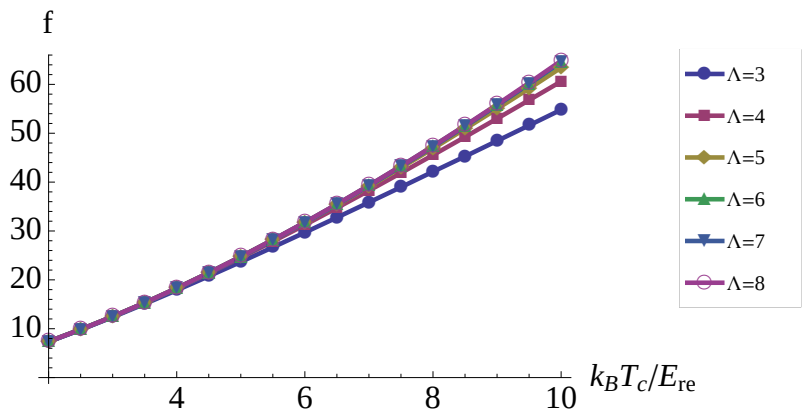

Figure 3-12: This graph shows how the calculated density increases with the critical temperature when different number of bands are included, at the large filing, higher critical temperature regime. Similarly with Eq. 3-11, the splitting between lines continues, indicating the higher the filling is, the more bands we need to consider. Here the lattice depth $q = V_0/4E_{re} = 1$.

The Hamiltonian is entirely time invariant before $t = 0$, we can denote $\mathcal{H}(t < 0) \equiv \mathcal{H}_\infty$. The density after the trap potential is turned off is obtained by

$$n(\mathbf{r}, t > 0) = \text{Tr}\rho_{\mathcal{H}_\infty}\hat{n}(\mathbf{r}, t), \tag{3.24}$$

where $\hat{n}(\mathbf{r}, t) \equiv e^{itH_0}n(\mathbf{r})e^{-itH_0}$. $\rho_{\mathcal{H}_\infty} \equiv \rho_{\mathcal{H}}(t < 0)$ is the initial density matrix at $t = 0$. The field operators $\hat{\Phi}(\mathbf{r})$ can be expanded in the eigenstates of H_0 or in the eigenstates of $\mathcal{H}_\infty$, and the former of which are just plane waves. Therefore we can obtain the density matrix $\rho_{\mathcal{H}_\infty}$ by equating the two expansions, and plug into Eq. 3.24 to solve for the density $n(\mathbf{r}, t > 0)$. The result is

$$n(\mathbf{r}, t) = \sum_i \sum_{\mathbf{k}} \mid e^{itE_{\mathbf{k}} - i\mathbf{k}\cdot\mathbf{r}}\tilde{\phi}_i(\mathbf{k}) \mid^2 n_B(\varepsilon_i - \mu), \tag{3.25}$$

where $\tilde{\phi}_i(\mathbf{k})$ is the Fourier transform of the eigenfunction of $\mathcal{H}_\infty$ to the momentum space. If we translationally move in the momentum space from $\mathbf{k}$ to $\mathbf{k} + \frac{m\mathbf{r}}{t}$, where

$\mathbf{k} \ll \frac{m\mathbf{r}}{t}$, Eq. 3.25 becomes

$$n(\mathbf{r}, t) \approx c \sum_i |\tilde{\phi}_i(\mathbf{r}m/t)|^2 \, n_B(\varepsilon_i - \mu). \tag{3.26}$$

We note that, up to an overall prefactor c, the right side of Eq. 3.26 is the momentum distribution $n(\mathbf{k})$ of the initial trapped gas, measured at momentum $\mathbf{k}_0 = m\mathbf{r}/t$. Thus, the density profile of the expanded cloud allows experimentalists to probe the momentum distribution of the trapped cloud. Detailed steps of the derivation to obtain Eq. 3.26 are provided in Appendix G.

3.5 Non-Interacting Density Profile after Free Expansion Results

The preceding derivation apply to bosons in an arbitrary trapping potential with arbitrary interactions (we assume they do not interact during the free expansion). We now want to apply these formulae to the case of non-interacting bosons in a periodic optical lattice potential. To calculate the density n, we need to know the Fourier transformed eigenfunctions of $\mathcal{H}_\infty$. If the trapping potential is relatively flat, we can neglect the trapping potential, the Hamiltonian is reduced to the Mathieu Hamiltonian, so $\phi_i(\mathbf{r})$ are just Mathieu Functions.

Furthermore, we still need a proper boundary conditions before working on real world problems, since actual experiments take place in finite systems, which affect the shapes of their wave functions. To understand the effect of finiteness on the system, we discuss two kinds of boundary conditions here: vanishing boundary (hard wall) and periodic boundary. The former assumes a box shaped potential well with a flat bottom, while the latter is a theoretical model in which the boundary on one end is made to connect with the other end. Detailed discussion is in Appendix E. Here we give only the results. The 1-D Fourier transformed wave

function for the vanishing boundary condition is

$$\phi(\nu,q,k)=\begin{cases}\frac{2}{L}\int_{-L/2}^{L/2}dx\cos(kx)\mathrm{ce}(a_\nu,q,k_{ol}x) & \nu=\frac{2n}{N_s};\\ \frac{2}{L}\int_{-L/2}^{L/2}dx\sin(kx)\mathrm{se}(b_\nu,q,k_{ol}x) & \nu=\frac{2n+1}{N_s}.\end{cases} \tag{3.27}$$

The 1-D Fourier transformed wave function for the periodic boundary condition is

$$\phi(n,q,k)=\sum_m c_{2m}^{2n/N_s}(q)\delta(\frac{2n}{N_s}+2m,-\frac{k}{k_{ol}}), \tag{3.28}$$

where m and n here are integers respectively indicating the momenta at the lattice scale and the quasi-momenta, and the coefficient

$$c_{2m}^{2n/N_s}(q)=\frac{1}{L}\int_{-L/2}^{L/2}dx\; e^{-(2n/N_s+2m)k_{ol}x}\mathrm{me}(2n/N_s,q,k_{ol}x), \tag{3.29}$$

when $n\neq 0$, and

$$c_{2m}^{0}(q)=\frac{\sqrt{2}}{L}\int_{-L/2}^{L/2}dx\; e^{-2mk_{ol}x}\mathrm{ce}(a_0,q,k_{ol}x), \tag{3.30}$$

when $n=0$. The function *me* in the integrand is a complex function defined from Mathieu functions

$$\mathrm{me}(\nu,q,u)=\mathrm{ce}(a_\nu,q,u)+i\;\mathrm{sgn}(\nu)\mathrm{se}(b_\nu,q,u), \tag{3.31}$$

where *sgn* is the sign function. In both cases, the 3-D wave function is just the product of the wave functions in each dimension.

For the free expansion density at a certain timestamp, we rewrite Eq. G.25 without the t dependence:

$$n(\mathbf{k})=N_0|\Phi_0(\mathbf{k})|^2+\sum_{i\neq 0}|\Phi_i(\mathbf{k})|^2 n_B(\epsilon_i-\mu), \tag{3.32}$$

where $\Phi(\mathbf{k})$ is the Fourier transformed Mathieu wave function.

Fig. $3-13$ is the density profile images of experiments and simulation from the Bloch group (Ref. [26]), where bright spots are density peaks indicating superfluidity. The critical temperature T_c is 26.5nK. The lattice depth $V_0 = 8E_{re}$. With Eq. 3.32, we are able to verify with the experimental data. Our calculation result is shown in Fig. $3-14$, where we use the same T_c and V_0 as in Ref. [26]. We assume a hard wall boundary of $N_s = 10$ on each dimension, where N_s is the number of sites, and the boundary condition is captured by the wave functions $\Phi_i(\mathbf{k})$, as given by Eq. E.4. Superfluidity only appears below T_c, meaning T_c is the onset for superfluidity, which is in consistency with Fig. $3-13$.

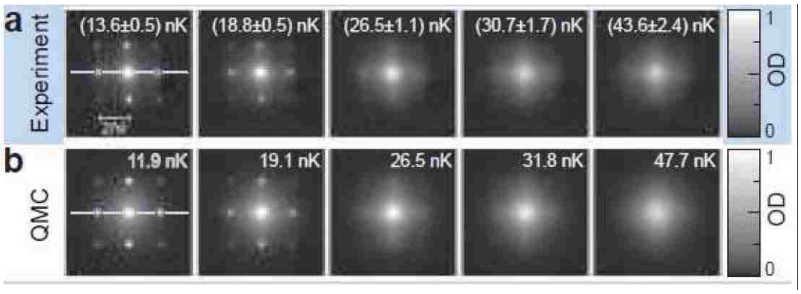

Figure 3-13: The absorption images of the freely expanded atomic cloud that are released from the trap and the optical lattice, taken from Ref. [26], are shown here. The upper panel shows the images from experiments, the lower panel shows images from Quantum Monte Carlo simulation. Temperatures of each case are labeled, the critical temperature $T_c = 26.5$nK, the lattice depth $V_0 = 8E_{re}$, where E_{re} is the recoil energy. Sharp spots indicate superfluidity. It can be seen that the density peaks disappear above the critical temperature T_c.

In Fig. $3-13$ and in Fig. $3-14$ one can see density peaks on the sides around the main peak in the center. These side peaks represent the phase coherent nature of the BEC in a periodic potential: In the expanded cloud bosons from neighboring wells are phase coherent, thus creating an interference pattern in the density distribution after expansion.

Next, we use our theory of freely expanded boson gases to reveal the nature of the side peaks and provide a powerful picture to demonstrate how multiple peaks

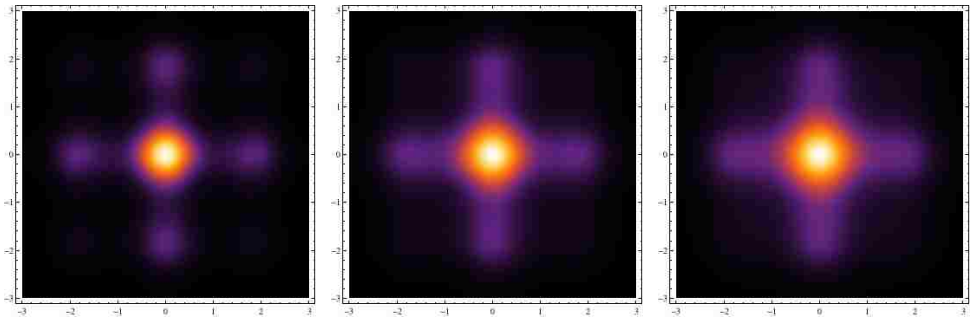

(a) $T = 10$nK (b) $T = 18.3$nK (c) critical $T_c = 26.5$nK

(d) $T = 31.8$nK (e) $T = 48.5$nK

Figure 3-14: The density profiles of the atomic gas after free expansion are calculated using the momentum distributions in the initial cloud with the vanishing boundary condition. Temperatures of each case are indicated, the critical temperature $T_c = 26.5$nK, the lattice depth $V_0 = 8E_{re}$, where E_{re} is the recoil energy. We use a hard wall boundary of $N_s = 10$ on each dimension. Sharp spots are density peaks from the superfluid state. One can see the density becomes diffuse above T_c. These calculations agree with the experiment and simulation results in Fig. $3-13$.

come about in the context of many states, while also being able to quantitatively describe the finite size effect. We choose the periodic boundary condition. Using Eq. G.25 and Eq. E.17, the density profile is

$$\begin{aligned} n_m(\mathbf{k}) \approx & N_0 \left|C[\mathbf{m}, 0, q]\right|^2 \delta(2\mathbf{m}, -\frac{\mathbf{k}}{k_{ol}}) \\ & + \delta_V^2(\mathbf{k} + 2k_{ol}\frac{\mathbf{n}}{N_s} + 2k_{ol}\mathbf{m}) \left|C[\mathbf{m}, -\frac{\mathbf{k}}{2k_{ol}} - \mathbf{m}, q]\right|^2 n_B(\epsilon(\mathbf{k}, \mathbf{m}) - \mu), \end{aligned} \tag{3.33}$$

$$n(\mathbf{k}) = \sum_m n_m(\mathbf{k}), \tag{3.34}$$

where $\mathbf{m}, \mathbf{n}, \mathbf{k}$ are m, n labels and the wave vector in 3-D, respectively. $C[\mathbf{m}, \mathbf{n}, q]$ is the 3-D product of the 1-D Fourier transform coefficient $c_{2m}^{2n/N_s}(q)$. It becomes clear that, the total density is the summation of many components, each of these components contains the ground state density (superfluid) and the excited states density (non-superfluid). Each component contributes mainly to one certain Brillouin zone, which is the reason why we see the grid of density peaks in Fig. $3-13$ and in Fig. $3-14$. Note that the δ-functions in the non-superfluid terms are replaced by δ_V, which is the smeared delta function to describe the width of every peak due to the finite size of the system. If the system were infinite, each peak would have a zero width (corresponding to the original δ-functions), which is not achievable in practice. To correctly reflect all the effects of the finite size, we define these smeared δ_V functions as

$$\begin{aligned} &\delta_V(\mathbf{k} + 2k_{ol}\frac{\mathbf{n}}{N_s} + 2k_{ol}\mathbf{m}) \\ &= \frac{8}{V}\prod_{i=x,y,z}\frac{\sin(L(k_i + 2k_{ol}\frac{n_i}{N_s} + 2k_{ol}m_i)/2)}{k_i + 2k_{ol}\frac{n_i}{N_s} + 2k_{ol}m_i}. \end{aligned} \tag{3.35}$$

Three 1-D graphs, Fig. $3-15$, $3-16$, $3-17$ further explain the different roles of each state and each component in the total density. Here we use a system size of $N_s = 10$ (the number of sites), lattice depth $V_0 = 10E_{re}$, critical temperature $k_B T_c = 0.105E_{re}$, and unit filling. Fig. $3-15$ shows the total density profile. Each peak comes from a component like the $m = 0$ component in Fig. $3-16$. A single peak as in Fig. $3-16$ contains both superfluid and non-superfluid. Also, a single state still contains multiple components, as shown by Fig. $3-17$ in which the ground state $\nu = 0$ contains side peaks besides the central peak. The three graphs are plotted with the same arbitrary temperature well below T_c. The finite widths in these plots are brought by the smeared δ_V function.

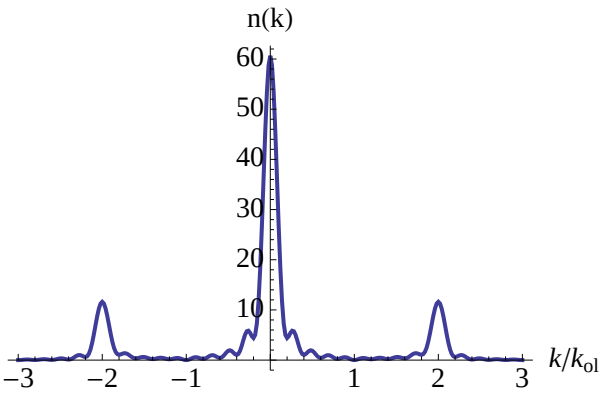

Figure 3-15: This graph shows the 1D total density profile after free expansion with periodic boundary condition. The temperature is below the critical temperature T_c. The total density contains multiple peaks, each peak comes from one component in the summation in Eq. 3.34. Here we use the system size $N_s = 10$, lattice depth $V_0 = 10E_{re}$, critical temperature $k_B T_c = 0.105E_{re}$, and unit filling. Finite size effect has been taken into account with the smeared δ_V function.

Sometimes it may be more convenient to work in Bloch or Wannier bases. To calculate the density of the freely expanded cloud, one only has to expand the field operator into the needed basis, and work through similar steps. Eqs. 3.36 and 3.37 are equations for the densities calculated with Bloch and Wannier bases respectively. The former sums over band indices and momenta, while the latter sums over band indices and lattice sites.

$$\hat{n}(\mathbf{r},t) = (\frac{m}{2\pi\hbar^2 t})^3 \sum_{n\mathbf{q}} \sum_{n'\mathbf{q}'} \tilde{\phi}^*_{n\mathbf{q}}(\frac{m\mathbf{r}}{t})\tilde{\phi}_{n'\mathbf{q}'}(\frac{m\mathbf{r}}{t}) c^\dagger_{n\mathbf{q}} c_{n'\mathbf{q}'}; \tag{3.36}$$

$$\hat{n}(\mathbf{r},t) = (\frac{m}{2\pi\hbar^2 t})^3 \sum_{n\mathbf{R}} \sum_{n'\mathbf{R}'} e^{i\frac{m\mathbf{r}}{t}\cdot\mathbf{R} - i\frac{m\mathbf{r}}{t}\cdot\mathbf{R}'} \tilde{w}^*_n(\frac{m\mathbf{r}}{t})\tilde{w}_{n'}(\frac{m\mathbf{r}}{t}) b^\dagger_n(\mathbf{R}) b_{n'}(\mathbf{R}'). \tag{3.37}$$

Here $\tilde{\phi}$ and $\tilde{w}$ are respectively Fourier transformed Bloch functions and Fourier transformed Wannier functions. $c_{n\mathbf{q}}$ and $b_n(\mathbf{R})$ are the annihilation operators of their respective basis. Appendix C provides details about these two orthonormal bases.

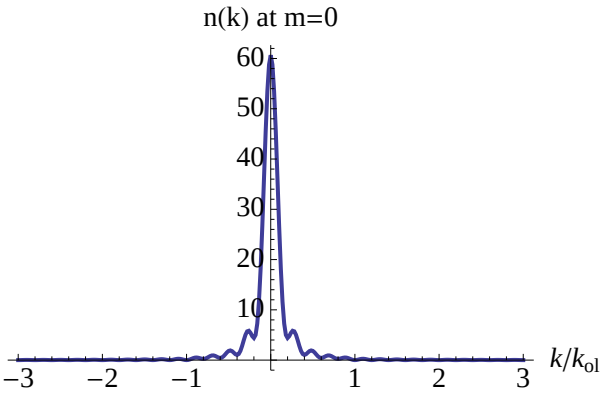

Figure 3-16: This graph shows the 1D free expansion density profile of the $m = 0$ component. Periodic boundary condition is used. The temperature is below the critical temperature T_c. Each component contributes to one peak as the $m = 0$ component does in this graph. Each peak still contains superfluid and non-superfluid parts, the former takes up a significant portion when the temperature is below T_c. Here we use the system size $N_s = 10$, lattice depth $V_0 = 10E_{re}$, critical temperature $k_B T_c = 0.105E_{re}$, and unit filling. Finite size effect has been taken into account with the smeared δ_V function.

3.6 Interacting Bosons in Optical Lattice: Hartree Fock Approximation

Previously we have introduced Hartree Fock Approximation in Sec. 2.3.3. In this Section, we apply Hartree Fock approximation to interacting bosons in an optical lattice. We also assume only the lowest band is included (Single Band Approximation).

From Eq. 2.42, the self energy for the lowest band is

$$\Sigma_{00}(\mathbf{k}; i\Omega_m) = 2g \int_V d^3r |\psi_{0\mathbf{k}}(\mathbf{r})|^2 n(\mathbf{r}), \tag{3.38}$$

where $g = 4\pi\hbar^2 a_s/m$, where a_s is the s-wave scattering length. The integral is the same for all unit cells, so we can downsize the integral to over a single unit cell. By using the Mathieu wave function, we come to

$$\frac{\Sigma_{00}(\mathbf{k}; i\Omega_m)}{E_{re}} = \frac{4mgV}{\hbar^2 {k_{ol}}^2 v} \int_{\tilde{v}} d^3u |\psi_{0\mathbf{k}}(\mathbf{u})|^2 n(\mathbf{u}), \tag{3.39}$$

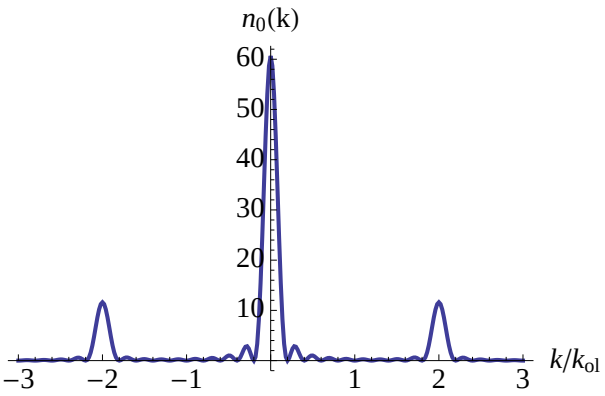

Figure 3-17: The 1D free expansion density of the ground state with periodic boundary condition. Because each component contains part of superfluid, the ground state density is seen in multiple peaks, containing multiple m components. The temperature is well below the critical temperature T_c, almost all the density is from the superfluid, the peak values are similar as compared to Fig. $3-15$. Here we use the system size $N_s = 10$, lattice depth $V_0 = 10E_{re}$, critical temperature $k_B T_c = 0.105E_{re}$, and unit filling. Finite size effect has been taken into account with the smeared δ_V function.

where ψ is the Mathieu function, $\mathbf{u} = k_{ol}\mathbf{r}$ is the dimensionless spatial variable (assuming an isotropic system), and the integral is over a unit cell $\tilde{v}$ in for $\mathbf{u}$ space. The u lattice spacing in 1D is π, so $\tilde{v}$ is a box of π on each side.

Assuming zero temperature, all particles are in the ground state

$$n(\mathbf{r}) = n_0(\mathbf{r}) = N \mid \psi_{0,\mathbf{k}=\mathbf{0}}(\mathbf{r}) \mid^2 \tag{3.40}$$

where N is the total particle number. Combing the above two equations, we are able to calculate the self energy Σ_{00}.

We can judge the extent of the interaction effects under the current approximation by inserting the self energy into Eq. 2.48

$$\frac{k^2}{2m^*} = \frac{k^2}{2m_{BAND}} + \frac{k^2}{2m_{INT}} + \frac{\Sigma_{00}(\mathbf{k}=\mathbf{0})}{\hbar^2} \tag{3.41}$$

where k is near 0, then compare the effective masses that respectively characterize the band dispersion and the interaction. Fig. $3-18$ compares the band effective m_{BAND} mass and the total effective mass m^*, which are almost identical. This means under current approximations, interaction effect is not discernible. Here we use the scattering length $a_s = 5.31$nm, the optical lattice wavelength $\lambda_{ol} = 844$nm, and the system size is $N_s = 10$.

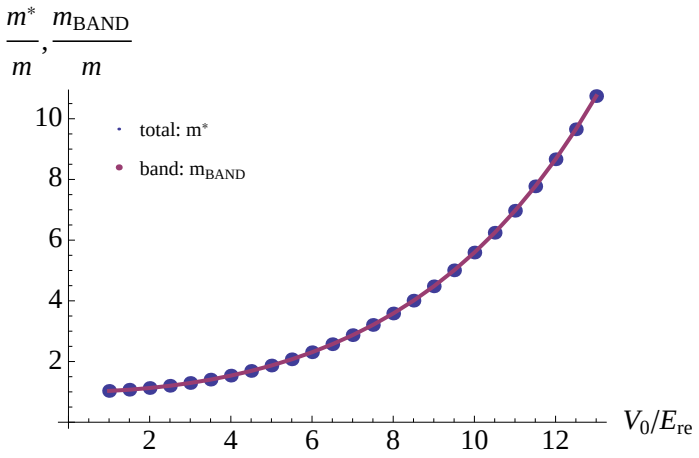

Figure 3-18: This graph compares the calculated band effective and the total effective masses, the former characterizing the band dispersion, the latter characterizing the combined effect from the band and the interaction. Since the two effective masses are almost identical, interaction effect is not discernible in this effective mass approach within the single band Hartree-Fock approximation. Here $a_s = 5.31$nm, $\lambda_{ol} = 844$nm, the system size is $N_s = 10$.

CHAPTER 4
INTERACTING BOSONS IN AN OPTICAL LATTICE: HARTREE FOCK SELF-CONSISTENT SCHEME

Previously in Chapter 2, we introduced the methods to treat interacting boson systems. Specifically, we have shown that interaction effects vanish identically, within the Hartree Fock approximation, for bosons in a uniform potential. In Chapter 3, we introduced optical lattices and showed how they alter the thermodynamic and dispersion properties of bosons. For bosons in a periodic optical lattice, we found that the simplest Hartree Fock approximation gives an extremely small correction to the transition temperature for the superfluid. In this chapter, we study the interaction effects for bosons in an optical lattice using the Hartree Fock self-consistent approach.

We will see that, for bosons in an optical lattice, interaction effects within a self-consistent Hartree-Fock approximation can significantly modify physical observables. Our self-consistent Hartree-Fock approximation is motivated by first noting that, bosons in a periodic cosine-shaped potential will have a local density that is also periodic. Approximately, this density is given by a constant piece plus a spatially-modulated cosine-shaped piece. Because the boson interactions are proportional to the local density, the spatially-modulated piece acts self-consistently like an additional potential for the bosons. Since the boson interactions are repulsive, this means that bosons in a periodic optical lattice with a given optical lattice depth will effectively "see" a lower lattice depth.

In this chapter, we first derive the underlying equations for our self-consistent Hartree-Fock scheme, then proceed to deploy this scheme to make predictions for

experimental observables such as the superfluid transition temperature, condensate fraction, and at last we calculate the real boson density and the boson momentum distribution of this interacting system.

4.1 Model

Self-Consistent Ansatz

We start by noting that, in a boson system with an optical lattice $V(\mathbf{r}) = V_0 v(\mathbf{r})$, where

$$v(\mathbf{r}) = \cos^2 kx + \cos^2 ky + \cos^2 kz - \frac{3}{2}, \tag{4.1}$$

if the lattice amplitude V_0 is small, then the modulus squared of the Mathieu functions asymptotically resembles a constant plus a cosine shape. This follows from the expansion of Mathieu functions for small q (Ref. [16]), where $q = V_0/4E_{re}$ with E_{re} being the recoil energy

$$\begin{aligned}\mathrm{me}(\nu, q, u) = e^{i\nu u} - \frac{q}{4}\Big(\frac{1}{\nu+1}e^{i(\nu+2)u} - \frac{1}{\nu-1}e^{i(\nu-2)u}\Big) \\ + \frac{q^2}{32}\Big[\frac{1}{(\nu+1)(\nu+2)}e^{i(\nu+4)u} + \frac{1}{(\nu-1)(\nu-2)}e^{i(\nu-4)u} - \frac{2(\nu^2+1)}{(\nu^2-1)^2}e^{i\nu u}\Big] + \ldots\end{aligned} \tag{4.2}$$

where $\mathrm{me}(\nu, q, u) = \mathrm{ce}(a_\nu, q, u) + i\ \mathrm{sgn}(\nu)\mathrm{se}(b_\nu, q, u)$, as defined in Appendix E. This formula implies that if lattice depths q are sufficiently small, the only terms that will contribute are the first line of Eq. 4.2. Otherwise, the local density does not have the constant plus cosine form. Nonetheless, we proceed by assuming this form holds, and capture it by

$$n(\mathbf{r}) \approx \frac{f}{a^3}[1 - cv(\mathbf{r})], \tag{4.3}$$

where f is the filling, a is the lattice spacing, and c is an unknown constant to be determined by our self-consistent scheme discussed below. This approximation ensures $\int d^3r\, n(\mathbf{r}) = N$, since the integral of the spatially dependent term over the unit cell vanishes ($\int_{cell} d^3r\, v(\mathbf{r}) = 0$)u. Because $|v(\mathbf{r})| < 3/2$, for the density $n(\mathbf{r})$ to be positive we need $-2/3 < c < 2/3$. We also expect the boson density to reach maxima at the minima of the lattice, which further implies $c > 0$.

Within the Hartree Fock Approximation, the boson self energy can be expressed as an effective single particle Hamiltonian $H_{HF} = 2gn(\mathbf{r})$ (Section 2.3.3), where the coupling constant $g = 4\pi\hbar^2 a_s/m$. Therefore the Schrödinger Equation becomes

$$[-\frac{\hbar^2\nabla^2}{2m} + (V_0 - \frac{2gfc}{a^3})v(\mathbf{r})]\psi_{\mathbf{k}}(\mathbf{r}) = E_{\mathbf{k}}\psi_{\mathbf{k}}(\mathbf{r}), \tag{4.4}$$

which is once again Mathieu Equation. The eigenvalues $E_{\mathbf{k}} = \varepsilon_{\mathbf{k}} - \frac{2gf}{a^3}$, where $\varepsilon_{\mathbf{k}}$ is the real boson energy. The physical density for non-condensate at temperature $T \geq T_c$ is simply

$$n(\mathbf{r}) = \sum_{\mathbf{k}} n_B(E_{\mathbf{k}} - \mu + \frac{2gf}{a^3})\,|\psi_{\mathbf{k}}(\mathbf{r})|^2, \tag{4.5}$$

where n_B is the Bose function.

Comparing with the Mathieu Equation in Chapter 3, Eq. 4.4 describes bosons in an optical lattice that has an effective lattice depth $\bar{q}$

$$\bar{q} = \frac{1}{4E_{re}}[V_0 - \frac{2gfc}{a^3}] = q - \frac{gfc}{2a^3E_{re}}, \tag{4.6}$$

which can be rearranged as

$$\bar{q} = q - \frac{4}{\pi}\frac{a_s}{a}fc, \tag{4.7}$$

suggesting the interaction effect can be seen as canceling part of the optical lattice ($\bar{q} < q$). In the last equation we used $E_{re} = \frac{\hbar^2\pi^2}{2ma^2}$.

Our next task is to use the thermodynamic equations of motion to determine the unknown parameter c that characterizes the effective optical lattice depth for superfluid bosons in optical lattices.

Transition Temperature

In this section, we continue using this Hartree Fock scheme to study the implication of interaction effects for the system's thermodynamic properties. According to our ansatz, the assumed density $n(\mathbf{r})$ should agree with the calculated density from Eq. 4.5. For systems at the critical temperature, this is

$$n(\mathbf{r}) = \sum_{\mathbf{k}} n_B(E_{\mathbf{k}} - E_0) \left|\psi_{\mathbf{k}}(\mathbf{r})\right|^2 = \frac{f}{a^3}[1 - cv(\mathbf{r})], \tag{4.8}$$

where E_0 is the ground state. Note that $2gf/a^3$ has been absorbed. Eq. 4.8 does not hold exactly for non-small q, but we proceed by assuming it approximately holds in an average sense. Consider the spatial average of Eq. 4.8 over the unit cell

$$\frac{1}{V}\int_{cell} d^3r \sum_{\mathbf{n}} n_B(E_{\mathbf{n}} - E_0) \left|\mathrm{me}(\frac{2n_x}{N_s}, \bar{q}, kx)\right|^2 \left|\mathrm{me}(\frac{2n_y}{N_s}, \bar{q}, ky)\right|^2 \left|\mathrm{me}(\frac{2n_z}{N_s}, \bar{q}, kz)\right|^2 = f, \tag{4.9}$$

where $v(\mathbf{r})$ vanished from spatial averaging. Converting the summation $\sum_{\mathbf{n}}$ into integral $\int d^3n$, and substituting with the Mathieu quasi-momentum label $\nu_i = n_i/N_s$, where $i = x,\ y,\ z$, the above equation becomes

$$\frac{{N_s}^3}{V}\int d^3\nu\, n_B(E_{\boldsymbol{\nu}} - E_0) \int_{cell} d^3r \left|\mathrm{me}(2\nu_x, \bar{q}, kx)\right|^2 \left|\mathrm{me}(2\nu_y, \bar{q}, ky)\right|^2 \left|\mathrm{me}(2\nu_z, \bar{q}, kz)\right|^2 = f. \tag{4.10}$$

Now we consider normalization conditions of the Mathieu function to simplify the integral. The orthonormality of the Mathieu function necessitates

$$\int_0^{\pi} du\ \left|\mathrm{me}(2\nu_x, \bar{q}, u)\right|^2 = \pi, \tag{4.11}$$

where the dimensionless spatial variable $u = k_{ol}x$. Through rescaling the integration variable we have,

$$\int_0^a dx \ |\mathrm{me}(2\nu_x, \bar{q}, kx)|^2 = a, \tag{4.12}$$

where we used $k = \pi/a = 2\pi/\lambda_{ol} = k_{ol}$. Therefore, with ${N_s}^3/V = a^{-3}$, the integral in Eq. 4.10 is reduced to

$$\int d^3\nu \ n_B(E_{\boldsymbol{\nu}} - E_0) = f, \tag{4.13}$$

which ensures Eq. 4.8 holds, on average, in each unit cell. Next, we demand that Eq. 4.8 holds for the leading non-uniformity of the local density in each unit cell. To do this, we multiply both sides of Eq. 4.8 by $v(\mathbf{r})$ and integrate over unit cell, obtaining a second self-consistent condition:

$$\int_{cell} d^3r \ n(\mathbf{r})v(\mathbf{r}) = \int_{cell} d^3r \frac{f}{a^3}[1 - cv(\mathbf{r})]v(\mathbf{r}) = -\frac{3}{8}cf. \tag{4.14}$$

On the other hand, with the explicit expression of $n(\mathbf{r})$ formed from the Mathieu functions

$$\begin{aligned}
&\int_{cell} d^3r \ n(\mathbf{r})v(\mathbf{r}) \\
=&\frac{{N_s}^3}{V} \int d^3\nu \ n_B(E_{\boldsymbol{\nu}} - E_0) \int_{cell} d^3r \ v(\mathbf{r}) \left|\mathrm{me}(2\nu_x, \bar{q}, kx)\right|^2 \left|\mathrm{me}(2\nu_y, \bar{q}, ky)\right|^2 \left|\mathrm{me}(2\nu_z, \bar{q}, kz)\right|^2.
\end{aligned} \tag{4.15}$$

We observe that the integration variables x, y, z can be separated

$$\begin{aligned}
&\int_{cell} d^3r \ v(\mathbf{r}) \left|\mathrm{me}(2\nu_x, \bar{q}, kx)\right|^2 \left|\mathrm{me}(2\nu_y, \bar{q}, ky)\right|^2 \left|\mathrm{me}(2\nu_z, \bar{q}, kz)\right|^2 \\
=&a^2[\int_0^a dx \ v(x) \left|\mathrm{me}(2\nu_x, \bar{q}, kx)\right|^2 + \int_0^a dy \ v(y) \left|\mathrm{me}(2\nu_y, \bar{q}, ky)\right|^2 + \int_0^a dz \ v(z) \left|\mathrm{me}(2\nu_z, \bar{q}, kz)\right|^2] \\
=&a^3[I(\nu_x, \bar{q}) + I(\nu_y, \bar{q}) + I(\nu_z, \bar{q})],
\end{aligned} \tag{4.16}$$

where $v(r_i) = \cos^2 kr_i - \frac{1}{2}$, $r_i = x,\ y,\ z$, and

$$I(\nu_i, \bar{q}) = \int_0^1 dl_i \, |\mathrm{me}(2\nu_i, \bar{q}, \pi l_i)|^2 \, (\cos^2 \pi l_i - \frac{1}{2}), \tag{4.17}$$

and $l_i = \frac{r_i}{a}$, $\nu_i = \nu_x,\ \nu_y,\ \nu_z$. Combing the above steps, we get

$$-\frac{3}{8} cf = \int d^3\nu \; n_B(E_{\boldsymbol{\nu}} - E_0)[I(\nu_x, \bar{q}) + I(\nu_y, \bar{q}) + I(\nu_z, \bar{q})]. \tag{4.18}$$

From Eq. 4.18 and Eq.4.7, the effective lattice depth $\bar{q}$ can be solved. Because the filling is known from the number equation Eq. 4.13, the parameter c can also be obtained right away. From these results, the interaction effect on the system's density profile is described.

Next, we describe how the same scheme would work for the non-superfluid phase above T_c and in the superfluid phase below T_c.

Above the Transition Temperature

The effective lattice depth $\bar{q}$ and the parameter c are temperature dependent, following from the fact that interaction effects depend on the density distribution which is temperature dependent. When the system is above T_c, the chemical potential is no longer pinned at the bottom of the band. Integrating Eq. 4.5 over the entire space, we have

$$\int d^3\nu \; n_B(E_{\boldsymbol{\nu}} - \mu + \frac{2gf}{a^3}) = f, \tag{4.19}$$

where all particles in the system are thermal. Note that $2gf/a^3$ can be written as $\frac{16}{\pi}\frac{a_s}{a} f E_{re}$. We can obtain the filling f from Eq. 4.13 for the critical temperature, then solve for the chemical potential μ for $T > T_c$ from the above number equation.

With the filling f and the chemical potential μ known, we will also be able to find c through

$$-\frac{3}{8}cf = \int d^3\nu \; n_B(E_{\boldsymbol{\nu}} - \mu + \frac{16}{\pi}\frac{a_s}{a}fE_{re})[I(\nu_x, \bar{q}) + I(\nu_y, \bar{q}) + I(\nu_z, \bar{q})], \tag{4.20}$$

which paves the way for us to describe the spatial and thermodynamical properties of this interacting system.

Below the Transition Temperature

When the system is below T_c, some of the bosons are in the condensate, therefore the density formulae need to be modified,

$$n(\mathbf{r}) = N_0 \left|\psi_0(\mathbf{r})\right|^2 + \sum_{\mathbf{k}\neq 0} n_B(E_{\mathbf{k}} - \mu + \frac{16}{\pi}\frac{a_s}{a}fE_{re}) \left|\psi_{\mathbf{k}}(\mathbf{r})\right|^2, \tag{4.21}$$

where N_0 is the number of condensed particles. From Appendix. E, the ground state Mathieu function is defined as

$$\psi_0(\mathbf{r}) = (\frac{2}{L})^{3/2}\mathrm{ce}(a_0, \bar{q}, k_{ol}x)\mathrm{ce}(a_0, \bar{q}, k_{ol}y)\mathrm{ce}(a_0, \bar{q}, k_{ol}z). \tag{4.22}$$

Integrating Eq. 4.21 over the whole space, we have

$$f = \frac{N_0}{N_s} + \int d^3\nu \; n_B(E_{\boldsymbol{\nu}} - E_0), \tag{4.23}$$

where N_s is the number of lattice sites. Similarly, Eq. 4.18 becomes

$$-\frac{3}{8}cf = N_0 \int_{cell} d^3r \; \left|\psi_0(\mathbf{r})\right|^2 v(\mathbf{r}) + \int d^3\nu \; n_B(E_{\boldsymbol{\nu}} - E_0)[I(\nu_x, \bar{q}) + I(\nu_y, \bar{q}) + I(\nu_z, \bar{q})]. \tag{4.24}$$

Using the definition of $\psi_0(\mathbf{r})$, we can rewrite the first term as

$$\begin{aligned}\int_{cell} d^3r \ |\psi_0(\mathbf{r})|^2 v(\mathbf{r}) &= \frac{3a^3}{V} \cdot 2 \int_0^1 dl \, |\mathrm{ce}(a_0, \bar{q}, k_{ol}x)|^2 \, (\cos^2 \pi l - \frac{1}{2}) \\ &\equiv \frac{3a^3}{V} I_0(\bar{q}),\end{aligned} \tag{4.25}$$

where in the second line we have defined $I_0(\bar{q})$. We therefore finally arrive at

$$-\frac{3}{8}cf = 3\frac{N_0}{N_s} I_0(\bar{q}) + \int d^3\nu \ n_B(E_{\boldsymbol{\nu}} - E_0)[I(\nu_x, \bar{q}) + I(\nu_y, \bar{q}) + I(\nu_z, \bar{q})], \tag{4.26}$$

from which, combining with Eqs. 4.7 and 4.23, we are able to solve for $\bar{q}$ and c for the interacting system below T_c.

4.2 Results

In the previous section we explained the Hartree Fock self-consistent approach for interacting bosons in optical lattices. We essentially approximated the inter-atom interaction as an effective periodic potential that partially offsets the optical lattice. To see how effective this theory is in describing interaction, we test on a few systems of both unit and large fillings to compute their phase transition temperatures, condensate fractions, and the density profiles after free expansion. We will also use some of our results to compare with the experimental data from Ref. [26]. It should be noted that, since our method is based on the expansion Eq. 4.2 for small lattice amplitude q, it is likely that our method is not able to capture the interaction effects at large q, tiny T limit, such as the suppression of the superfluid transition temperature near the Mott phase.

We did our calculation on a system of ^{87}Rb atoms, and the recoil energy equals 1.334×10^{-11}eV, using the same condition in Ref. [26]. The strength of interaction is directly related to the s-wave scattering length a_s, which can be tuned in a wide

range in experiments since a_s is very sensitive to magnetic field as a result of Feshbach resonance [29]. We use two a_s here. To compare with experimental data in Ref. [26], we use the same scattering length $a_{s1} = 5.31$nm for part of our calculation. To show the effectiveness of our theory at the large interaction limit, we apply $a_{s2} = 42.2$nm, equaling $1/10$ of the lattice spacing (assuming λ_{ol} =844nm lasers for the optical lattice), to other parts of our calculation. We also anticipate smaller interaction effects for few condensate and small filling, and large interaction effect for large condensation fraction and large filling.

To compute the transition temperature and the condensate fraction, in our calculation we tabulated data in the original lattice depth q, effective lattice depth $\bar{q}$, filling f, temperature T and condensate fraction $n_0 = N_0/N$ for $q = 0.5 - 6.1E_{re}$, $\bar{q} = 0.5 - 5.5E_{re}$, $f = 0.02 - 145$, $T = 0.05 - 1E_{re}/k_B$, $n_0 = 0 - 1$. For a_{s2}, the tabulated data extend to $q = 0.5 - 10.3E_{re}$, while other parameter ranges are the same. The data of physical observables are then obtained from interpolation and plotted in Figs. $4-1, 4-2, 4-3, 4-4, 4-5$.

4.2.1 Transition Temperature

The effect of two-body interactions on the superfluid transition temperature has been a theoretical pursuit for decades. Contradicting theories have been presented, including both positive T_c shift and negative T_c shift claims [19]. In the following we will see within our density and interaction regime the transition temperature is increased by interaction, a trend agreeing with most of recent works (see Table. I of Ref. [19] that lists 11 recent analytical and numerical results, also Ref. [28]. These work suggest the increase of T_c is proportional to $(na_s^3)^\gamma$, where n is the number density and $\gamma \approx \frac{1}{3}$).

The physical scenario of this T_c increase can be explained as follows. For the cloud not to collapse, the interaction has to be repulsive, which pushes away the

atoms from each other, expanding the atomic cloud. As a result, bosons are more evenly distributed throughout the system, thus it is more likely for them to exchange with their neighbors in an suitable distance. This is advantageous for the transition into superfluid to occur, which means higher transition temperatures. This density homogenization effect is reflected in our self consistent scheme as the partial offset of the optical lattice by interaction. With a lower effective lattice potential, there is not as much spatial variation in the BEC. Even we only look at the non-interacting T_c vs. q curve, the critical temperature corresponding to a non-interacting system with lattice depth $\bar{q}$ is higher on the curve than in a system with lattice depth q. Therefore it should be no surprise to see the critical temperature raised by interaction. This density homogenization effect of interaction will specifically illustrated later.

We first examine the superfluid transition temperature at unit filling, $a_s = a_{s1}$. Fig. $4-1$ shows the calculated critical temperature T_c decreasing with increasing optical lattice, as expected. At unit filling, there is only one atom per site on average, and interaction is weak. We can see from this figure that there is no discernible difference between the non-interacting T_c and the interacting T_c. Also included is the experimental data from Ref. [26] (indicated as "Trotzky et al."), which is still largely consistent with our calculation, except at $T \to 0$ and large q. This indicates that at unit filling, phase transitions of interacting systems occurring far away from the Mott regime may still be approximately described by non-interacting theories.

When adding more particles into the system, interaction effects are stronger, the transition temperature shows deviation from the non-interacting case, as seen in Fig. $4-2$, where the filling $f = 5$. In Fig. $4-3$, filling $f = 5$, we increase the scattering length to $a_s = a_{s2}$ to display the effect of a stronger interaction. Comparing Fig. $4-1$, Fig. $4-2$ and Fig. $4-3$, we see that interaction indeed increases the superfluid transition temperature.

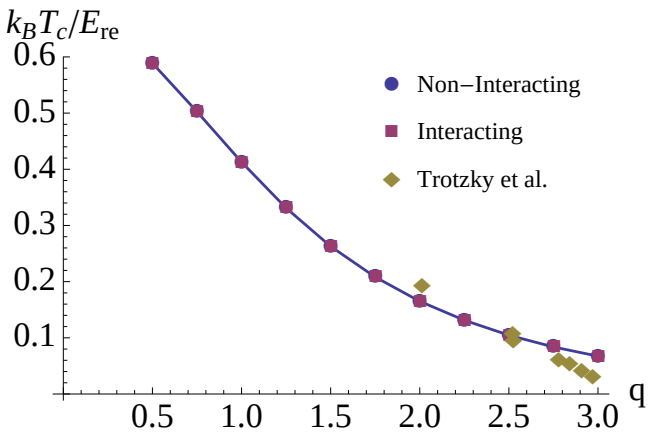

Figure 4-1: We show in this plot the trend of the transition temperature T_c with the optical lattice depth $q = V_0/4E_{re}$, displaying our non-interacting calculation, interacting calculation and experimental data from Ref. [26] (indicated as "Trotzky et al."). When the system is at unit filling and $a_s = a_{s1}$ ($\sim$1.3% of the lattice spacing), the transition temperatures for non-interacting gas and interacting-gas are is almost identical due to the weakness of interaction. Our calculation is consistent with the experiment except at the low temperature, very deep lattice regime.

4.2.2 Condensate Fraction

Now we turn to the temperature regimes below T_c, and calculate how the increase of temperature or lattice potential amplitude depletes the condensate. In the unit filling case Fig. $4-4$, we show the condensate fraction N_0/N decreasing with increasing q, suggesting the interaction effect for the condensate fraction is already noticeable even at unit filling. In Fig. $4-5$, $f = 5$, we show the condensate fraction decreasing with increasing temperature. A significant difference caused by interaction is observable in this graph. Here, $a_s = a_{s1}$ in both figures.

Note that the condensation fractions for the non-interacting gas and interacting gas are most separated away at intermediate T or q values between 0 and the critical values. This follows from that interaction effects are strongest when the local density deviates far from uniformity. For relatively low temperatures or lattice depths (comparing with T_c or q_c), many bosons are in the condensate wave function and exhibit a local non-uniform density. As $T \to T_c$ or $q \to q_c$, the bosons occupy many

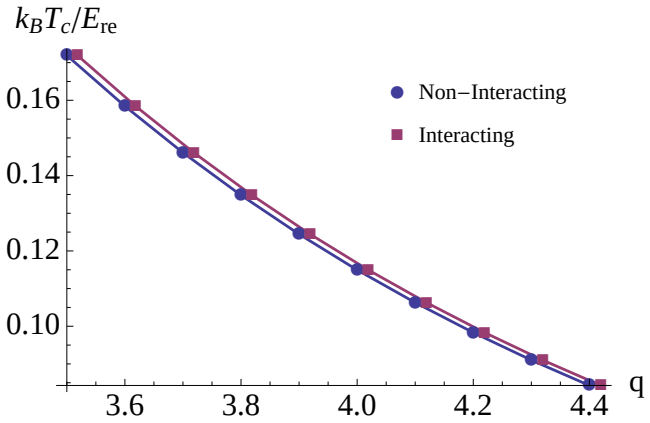

Figure 4-2: In this graph, we show the trend of the transition temperature T_c with varying lattice depth $q = V_0/4E_{re}$. When the system is at filling $f = 5$ and $a_s = a_{s1}$(∼1.3% of the lattice spacing), the high filling enhances interaction, which causes the discernible difference between the transition temperatures for non-interacting gas and interacting-gas, comparing with Fig. $4-1$.

levels and the non-uniformity is "washed out". The lack of spatial variation is also the reason for the minimal interaction effects exhibited at $q \to 0$. However, condensation fractions of interacting and non-interacting gases coinciding $T = 0$ has a different reason: all bosons in the gas must condense to the ground state at zero temperature ($N_0/N = 1$).

4.2.3 Boson Density

Using our scheme to obtain the wave functions of interacting bosons (expressed in Mathieu functions), we are able to plot the boson densities in the real space and delineate interaction effects by comparing densities of interacting bosons and non-interacting bosons.

We show our results in Figs. 4-6, 4-7 and 4-8. Here we examine a system at the transition temperature $T_c = 59.56$nK, filling $f = 2.83$, optical lattice depth $V_0 = 8E_{re}$, laser wavelength $\lambda_{ol} = 844$nm, scattering length $a_s = a_{s2} = 42.2$nm. Fig. 4-6 and Fig. 4-7 show the boson density as a function of the spatial variable x in a unit cell, for cuts at the center $y = \pi/2$, $z = \pi/2$, and near the edge $y = \pi/8$, $z = \pi/8$,

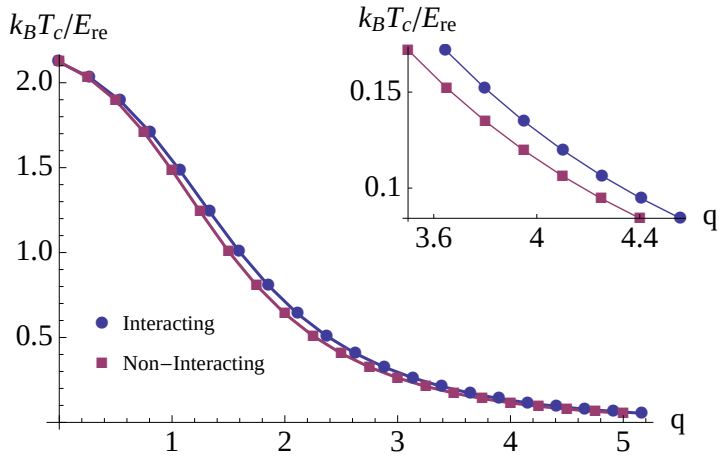

Figure 4-3: In this graph, the main plot shows the transition temperatures of non-interacting gas and interacting gas as a function of the optical lattice depth $q = V_0/4E_{re}$. We see the difference of the two temperatures is bigger at intermediate values of lattice depth. The inset panel shows a zoom-in version at regimes comparable with Fig. $4-2$, showing a bigger difference between the interacting and non-interacting T_c due to the larger interaction. Here the filling $f = 5$ and $a_s = a_{s2}$(1/10 of the lattice spacing).

respectively. At the center, the density of interacting bosons is significantly lower than the density of non-interacting bosons, whereas the two densities are reversed near the edge of a unit cell. This means, due to interaction effects the density is suppressed where it is high, and raised where it is low, thus evening out the density of the whole system.

Fig. 4-8 shows the contour plot of boson densities for a slice at $z = \pi/3$ in the unit cell. Fig. $4-8a$ and Fig. $4-8b$ are interacting and non-interacting boson densities, respectively. Fig. $4-8c$ is the difference between the non-interacting density and the interacting density. In Fig. $4-8c$, we take the difference of the non-interacting and interacting densities. The dashed circle in Fig. $4-8c$ indicates the zero contour, where the non-interacting and interacting densities equal. Inside the zero contour, the density of non-interacting bosons is larger, whereas outside the zero contour, the density of interacting bosons is larger. These contour plots are equivalent to Figs. 4-6 and 4-7, and also confirms that interaction does make a more uniform boson gas.

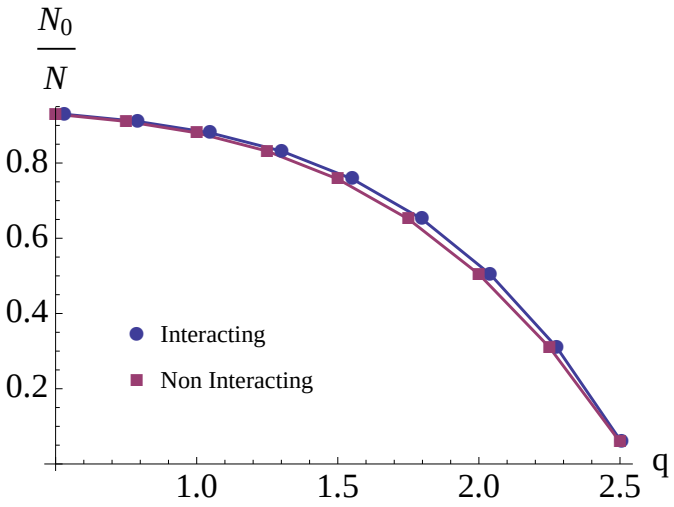

Figure 4-4: In this graph, we show the condensation fraction N_0/N for both interacting and non-interacting gases, as a function of the lattice depth $q = V_0/4E_{re}$. The condensate fraction decreases with increasing lattice depth q, approaching the critical point. We also observe that the condensation fraction for the interacting gas is larger than that of he non-interacting gas. Here the system is at unit filling and $a = a_{s1}$(∼1.3% of the lattice spacing).

4.2.4 Density Profile after Free Expansion

By integrating our theory into the free expansion calculation in Chap.3, we are able to obtain the density profiles after free expansion through momentum distribution for interacting systems. Note that we are not considering interaction during the expansion.

Fig. $4-9$ shows our calculation for the same unit filling system in Ref. [26], at the same temperatures: 10nK, 18.3nK, 26.5nK, 31.8nK and 48.5nK, in which 26.5nK is the critical temperature according to the reference. We still use the hard wall boundary condition. Comparing with Fig. $3-14$, there is not a visually recognizable difference that can be observed from these expanded density profiles, although there is indeed a quantitatively subsistent difference caused by interaction effects, which results in a smaller effective $\bar{q}$ (indicated in the caption of Fig. $4-9$) and increases the chemical potential.

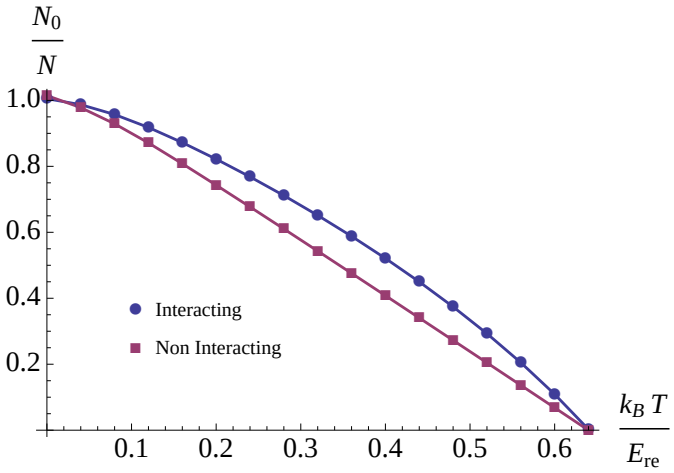

Figure 4-5: Here we plot the condensation for both non-interacting and interacting gases, as a function of the critical temperature, over the temperature range from $T = 0$ to T_c (where the fraction becomes zero). The condensate fraction N_0/N decreases with increasing temperature, as expected. With interaction, the system contains more condensate at a given temperature. We also note that the larger filling has clearly enhanced the interaction effect. Here $f = 5$ and $a = a_{s1}$($\sim$1.3% of the lattice spacing).

To illustrate this difference, it is better to switch to 1D density profile in the momentum distribution, as displayed in Fig. $4-10$. We still use the hard wall boundary condition. After separately normalizing the densities to the maximum density, we see that interacting bosons exhibit lower side peaks, as shown in Fig. $4-10a$, when comparing with the non-interacting boson densiy in Fig. $4-10b$. In the expanded density, the side peaks are signs of different momentum states, so the suppressing of side peaks in the expanded density of interacting bosons implies a more uniform cloud, which corroborates with the above results of the real boson density.

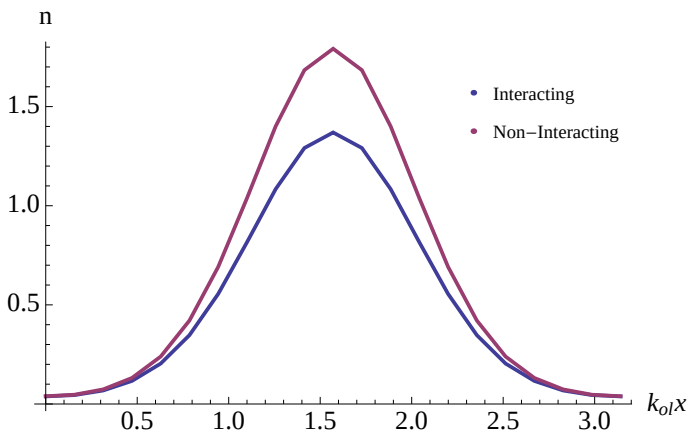

Figure 4-6: This plot shows the boson density as a function of the spatial variable x in a unit cell at $y = \pi/2$, $z = \pi/2$. The density is suppressed by interaction at the center of a unit cell. Here $T = T_c = 59.56$nK, $f = 2.83$, $V_0 = 8E_{re}$, $a_s = 10\%$ lattice spacing.

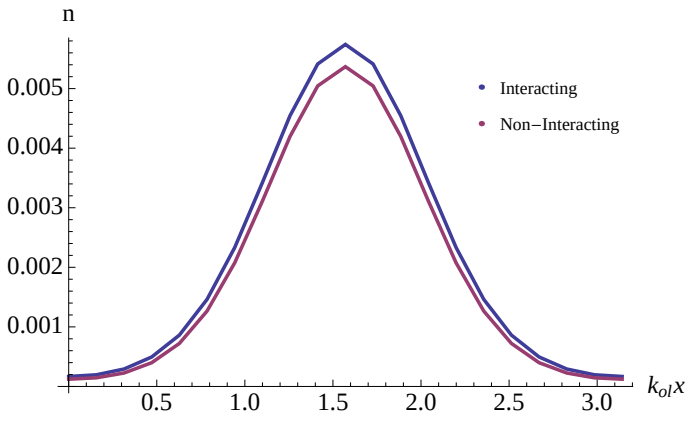

Figure 4-7: This plot shows the boson density as a function of the spatial variable x in a unit cell at $y = \pi/8$, $z = \pi/8$. The density is raised by interaction near the edge of a unit cell. Here $T = T_c = 59.56$nK, $f = 2.83$, $V_0 = 8E_{re}$, $a_s = 10\%$ lattice spacing.

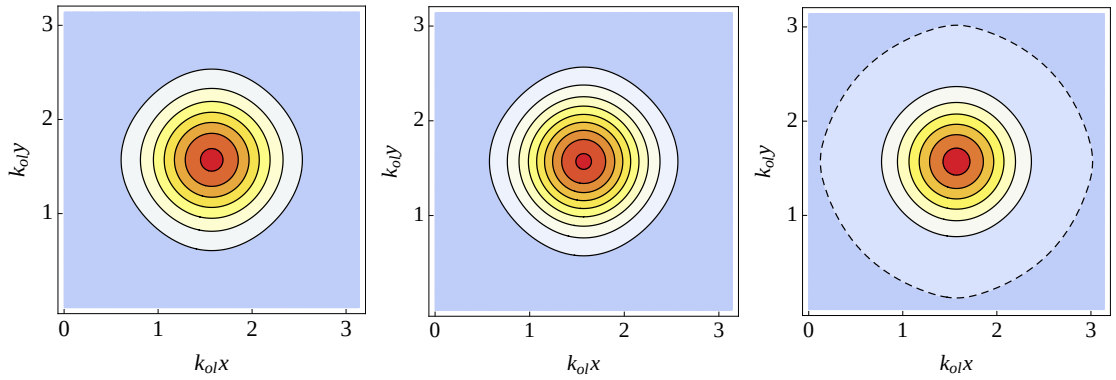

(a) Interacting (b) Non-Interacting (c) Non-interacting - Interacting

Figure 4-8: The contours of the boson densities are shown here for a slice at $z = \pi/3$ in the unit cell. Fig. $4-8a$ and Fig. $4-8b$ are interacting and non-interacting boson densities, respectively. Fig. $4-8c$ is the difference between the non-interacting density and the interacting density. The dashed line is the zero contour, indicating the locations where the non-interacting and interacting densities equal. Here $T = T_c = 59.56$nK, $f = 2.83$, $V_0 = 8E_{re}$, $a_s = 10\%$ lattice spacing.

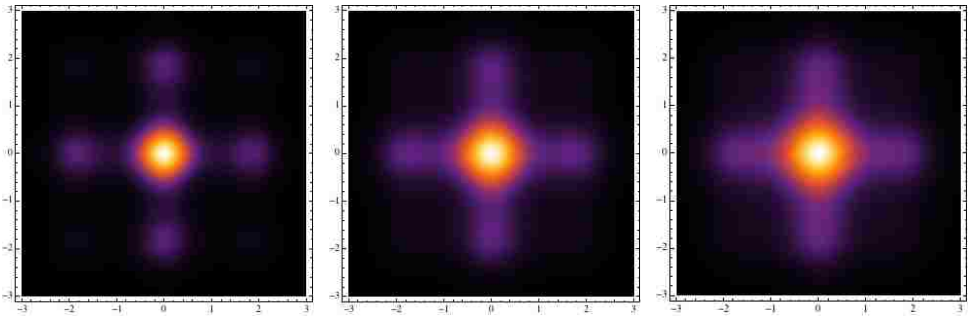

(a) $T = 10nK$, $\bar{q} = 1.9360$ (b) $T = 18.3nK$, $\bar{q} = 1.9635$ (c) critical $T_c = 26.5nK$, $\bar{q} = 1.9968$

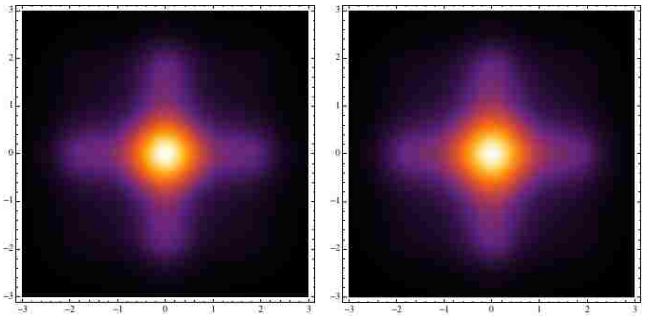

(d) $T = 31.8nK$, $\bar{q} = 1.9971$ (e) $T = 48.5nK$, $\bar{q} = 1.9974$

Figure 4-9: Here we display the the density profile of interacting bosons based on the momentum distribution after free expansion, using the Hartree-Fock self-consistent method, at the cut $k_{ol}z = 1$. The sampled temperatures are the same as in Ref. [26] and in Fig. 3-14 for comparison. We also give the calculated effective lattice depth $\bar{q}$ here, which describes the periodic potential the bosons "see" when considering interacting effects, for an imposed lattice depth of $q = V_0/4E_{re} = 2$. The sharp bright spots indicate BEC. While the density profiles show the expected trend from sharp to diffuse as the temperature increases, the distributions are actually slightly more uniform in the interacting case, as compared to Fig. 3-14. Here the filling $f = 1.046$, $a_s = a_{s1}$($\sim$1.3% of the lattice spacing).

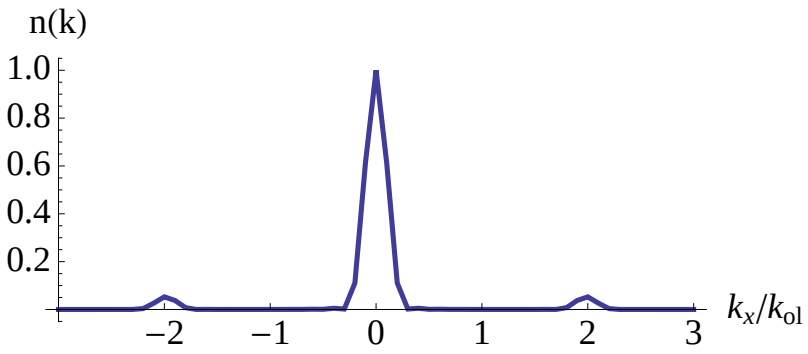

(a) Interacting

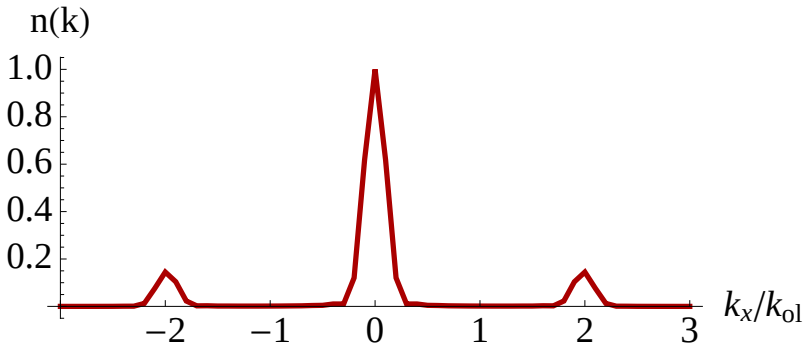

(b) Non-interacting

Figure 4-10: The density profile after free expansion for a cut at $k_y = k_z = 0$. Densities in two graphs are separately scaled to 0 to 1.The upper panel Eq. 4-10a shows the side peaks are suppressed, comparing with the lowered panel Eq. 4-10b. Here $T < T_c = 40.75$nK, $f = 2.83$, $V_0 = 8E_{re}$, $a_s = 10\%$ lattice spacing.

CHAPTER 5
SETUP FOR BOSONS WITH SPIN-ORBIT COUPLING

In previous chapters, we have mainly discussed the phase transitions of non-interacting and interacting BEC's in optical lattices. Beginning from this chapter, we study the phases and dynamics of bosons with light-induced artificial spin-orbit coupling (SOC). SOC in electronic materials is a relativistic effect, in which an electron moving in a potential gradient effectively "sees" an effective magnetic field. To mimic this in a cold-atom experiment, the Spielman group at NIST has developed methods of using light to artificially create an effective spin orbit coupling potential for trapped cold atomic gases [34].

In this chapter, we first review the experimental setup utilized in the Spielman group experiment for achieving artificial SOC for bosons and, more generally, for creating artificial gauge fields. Then we derive the effective boson Hamiltonian for the SOC. In Chapter 6, we analyze the band structure of this Hamiltonian, examine its implications for the phases that arise in interacting bosons with SOC, and discuss experimental signatures that could help identify the featured phases.

5.1 Background

Spin-orbit coupling for bosons is interesting for two distinct reasons. Firstly, we can closely mimic, in cold atom experiments, electronic systems in which spin-orbit coupling plays a central role. Secondly, since SOC modifies the low energy dispersion, it can tremendously amplify the effect of inter-atomic interactions, Therefore, with SOC, interaction effects can be important even the interaction itself is small [30].

The pioneering experiment of bosons with light-induced SOC was conducted by the Spielman group at NIST on a ^{87}Rb Bose-Einstein condensate (BEC) [34], in which dressed atomic spin states with emergent SOC are engineered via coupling to Raman lasers. This experimental knob further expands the space of Hamiltonians for cold atom systems to realize, and opens the possibility of simulating solid-state systems in which SOC plays a role, including the spin Hall effect [41], Majorana fermions [64], and topological insulating phenomena [39, 43]. The Spielman group has made earlier achievements that paved their way to this breakthrough, such as artificial gauge fields [31] and artificial magnetic fields [32] for cold atoms.

Theoretical interest in bosons with SOC has been strong for many years, although many early papers focused on the case of Rashba-type spin-orbit coupling [38, 62, 65, 66, 67, 68, 69], a type of SOC seen in electronic materials that can be described in the form $\hat{p}_x\sigma_y - \hat{p}_y\sigma_x$, where $\hat{p}_x$, $\hat{p}_y$ are respectively the momentum operators on $\hat{\mathbf{x}}$ and $\hat{\mathbf{y}}$ dimensions, and σ_x and σ_y are Pauli matrices acting in the space of dressed spins. However, The NIST Raman setup instead realizes SOC only along one direction, i.e., the SOC Hamiltonian is of the form $\hat{H}_{\mathrm{SOC}} \propto \sigma_z\hat{p}_x$. Subsequent experiments have observed dipole oscillations of bosons with artificial SOC [49] and studied their phases at finite temperature [70], have realized light-induced SOC for cold fermionic gases [52, 53], and have employed a similar setup to observe Zitterbewegung of bosons described by an effective Dirac Hamiltonian [46, 47]

Using ^{87}Rb atoms, Ref. [34] starts in the spin space of three hyperfine states $|F, m_F\rangle$ with $F = 1$ and $m = 1, 0, -1$, then transforms two of the three states $|\uparrow\rangle = |1, 0\rangle$ and $|\downarrow\rangle = |1, -1\rangle$ into dressed spin states $|\uparrow'\rangle$ and $|\downarrow'\rangle$. A key observation of Ref. [34] was the phase transition from a mixed BEC phase, with condensates of both $|\downarrow'\rangle$ and $|\uparrow'\rangle$, into a regime of phase separation, with spatially separated $|\downarrow'\rangle$ and $|\uparrow'\rangle$ condensates. Theoretically this mixed phase is predicted to exhibit "stripe

order" in the form of density modulations along the x axis, due to the system condensing in a superposition of states with different momenta [35, 71, 72], although such density modulations may be difficult to observe. Our aim is to determine the extent of such density modulations (to see if they can possibly be observed experimentally) and to find other experimental consequences of the mixed BEC phase.

5.2 Raman Scheme

We start by noting that the total Hamiltonian of a system written in matrices is

$$\mathcal{H} = \mathcal{H}_0 + \mathcal{H}_1 - \hat{\mu}\hat{N}, \tag{5.1}$$

acting on $\Psi = (\psi_1, \psi_0, \psi_{-1})^T$, of which the three components correspond with $m = 1$, $m = 0$, $m = -1$ states, respectively. $\mathcal{H}_0 = \int d^3r\ \Psi^\dagger H_0 \Psi$ is the bare Hamiltonian, $\mathcal{H}_1$ is the interaction Hamiltonian, $\hat{\mu}$ and $\hat{N}$ are chemical potentials and particle numbers of the species, written as vectors.

The interaction Hamiltonian for a two-species spinor BEC has been obtained in Sec. 2.5 as

$$\mathcal{H}_1 = \frac{1}{2}\int d^3r\ [c_0(n_\uparrow + n_\downarrow)^2 + c_2(2n_\uparrow n_\downarrow + {n_\downarrow}^2)], \tag{5.2}$$

where n_σ are the densities of the two species, with $\sigma = \uparrow, \downarrow$, and c_0 and c_2 are interaction parameters. In the following, we focus on obtaining the expression for the non-interacting part H_0 through the Raman scheme, starting from the full three component spin space.

Two Raman lasers of frequencies ω_L and $\omega_L + \Delta\omega_L$, propagating along $\hat{\mathbf{x}} + \hat{\mathbf{y}}$ and $\hat{\mathbf{y}} - \hat{\mathbf{x}}$, as shown in Fig. $5-2$, couple the hyperfine states of $F = 1$ of ^{87}Rb atoms. The level diagram of these hyperfine states is shown in Fig. $5-1$, where ϵ is the quadratic Zeeman shift, and δ is the Raman detuning. These states $|m_F, k_x\rangle$ differ in internal angular momentum (m_F) by $\hbar$, and in linear momentum ($\hbar k_x$) by $2\hbar k_r$,

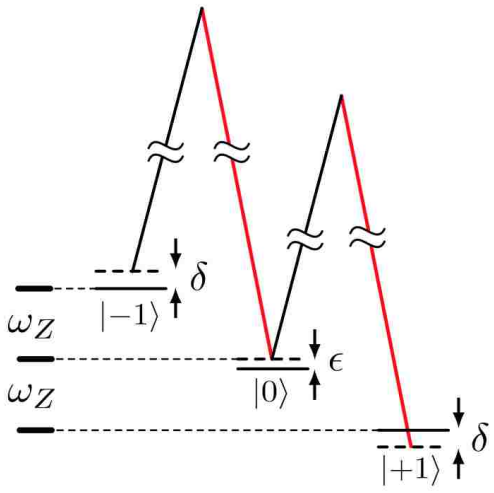

Figure 5-1: In the NIST scheme to create artificial SOC, the three hyperfine states of ^{8}7Rb are used. Laser field couples the $|F=1, m=-1\rangle$ state with $|F=1, m=0\rangle$, and $|F=1, m=0\rangle$ with $|F=1, m=1\rangle$. ω_Z is the Zeeman effect, ϵ is the quadratic Zeeman shift, and δ is the Raman detuning. Image from Ref. [32].

where $\hbar k_r = h/\lambda$ is the single photon recoil momentum, with λ being the laser wavelength.

The bare Hamiltonian consists of the kinetic term, the Zeeman term and the Raman term. The Raman Hamiltonian H_R is [34]

$$H_R = \frac{\Omega_R}{\sqrt{2}} F_z [e^{i(2k_L x + \Delta\omega_L t)} + h.c.], \tag{5.3}$$

where Ω_R is the Rabi Frequency (details about Rabi Oscillation is in Appendix H), F_z is one of the three Pauli matrixes, together with F_x and F_y

$$F_x = \frac{1}{\sqrt{2}} \begin{pmatrix} 0 & -i & 0 \\ i & 0 & -i \\ 0 & i & 0 \end{pmatrix}, \; F_y = \begin{pmatrix} 1 & 0 & 0 \\ 0 & 0 & 0 \\ 0 & 0 & -1 \end{pmatrix}, F_z = \frac{1}{\sqrt{2}} \begin{pmatrix} 0 & 1 & 0 \\ 1 & 0 & 1 \\ 0 & 1 & 0 \end{pmatrix}. \tag{5.4}$$

Because the magnetic field is at $\hat{\mathbf{y}}$ direction, we have rotated the reference frame so that F_y is diagonal.

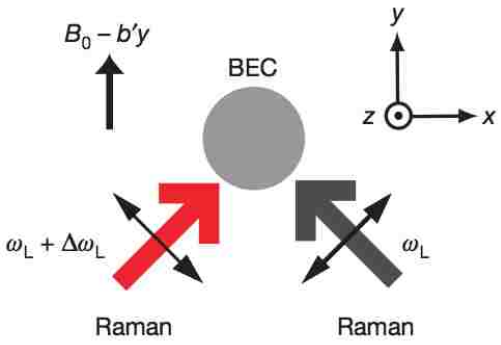

Figure 5-2: This graph schematically shows the setup geometry used in the experiment of inducing spin-orbit coupling for bosons. Two Raman lasers intersect with a right angle on the $x-y$ plane with a frequency difference of $\Delta\omega_L$. There is a spatial gradient contained in the external magnetic field. Image from Ref. [32].

With the above Raman Hamiltonian, we make a unitary transformation

$$V = \begin{pmatrix} e^{i\Delta\omega_L t} & 0 & 0 \\ 0 & 1 & 0 \\ 0 & 0 & e^{-i\Delta\omega_L t} \end{pmatrix} = e^{i\Delta\omega_L t F_y}, \tag{5.5}$$

which gives,

$$V^\dagger F_z V = \frac{1}{\sqrt{2}} \begin{pmatrix} 0 & e^{-i\Delta\omega_L t} & 0 \\ e^{i\Delta\omega_L t} & 0 & e^{-i\Delta\omega_L t} \\ 0 & e^{i\Delta\omega_L t} & 0 \end{pmatrix}. \tag{5.6}$$

Thus,

$$e^{i\Delta\omega_L t} V^\dagger F_z V \approx \frac{1}{\sqrt{2}} \begin{pmatrix} 0 & 1 & 0 \\ 0 & 0 & 1 \\ 0 & 0 & 0 \end{pmatrix} = \frac{1}{2} F_+ ; \tag{5.7}$$

$$e^{-i\Delta\omega_L t} V^\dagger F_z V \approx \frac{1}{\sqrt{2}} \begin{pmatrix} 0 & 0 & 0 \\ 1 & 0 & 0 \\ 0 & 1 & 0 \end{pmatrix} = \frac{1}{2} F_- , \tag{5.8}$$

where we have discarded the terms with $e^{\pm 2i\Delta\omega_L t}$ by virtue of the Rotating Wave Approximation. Now the transformed Raman Hamiltonian is

$$V^\dagger H_R V = \frac{1}{2}\Omega_R(F_z \cos 2k_L x - F_x \sin 2k_L x). \tag{5.9}$$

Also, we have

$$iV^\dagger \frac{d}{dt} V = i\frac{d}{dt} - \Delta\omega_L F_y. \tag{5.10}$$

The single particle Hamiltonian is $H_K = \frac{\mathbf{p}^2}{2m} F_0$, where F_0 is the 3 by 3 identity matrix, plus the Zeeman effect, yielding the following Hamiltonian

$$H_K + H_Z = \begin{pmatrix} \frac{\mathbf{p}^2}{2m} - \omega_Z + \omega_q & 0 & 0 \\ 0 & \frac{\mathbf{p}^2}{2m} & 0 \\ 0 & 0 & \frac{\mathbf{p}^2}{2m} + \omega_Z \end{pmatrix}, \tag{5.11}$$

where ω_z and ω_q represent the Zeeman shift and the quadratic Zeeman shift, respectively.

With the above equations, the full effective Hamiltonian is

$$H_{eff} = \begin{pmatrix} \frac{\mathbf{p}^2}{2m} + \omega_q + \delta & 0 & 0 \\ 0 & \frac{\mathbf{p}^2}{2m} & 0 \\ 0 & 0 & \frac{\mathbf{p}^2}{2m} - \delta \end{pmatrix} + \frac{1}{2}\Omega_R(F_z \cos 2k_L x - F_x \sin 2k_L x), \tag{5.12}$$

where $\delta = \Delta\omega_L - \omega_Z$. Since Ref. [34] works in a spin-$\frac{1}{2}$ subspace, we project the Hamiltonian into the bottom right 2 by 2 matrix, i.e. the $m = 0$ and $m = -1$ subspace (denoted as H_0)

$$H_0 = \frac{\mathbf{p}^2}{2m}\sigma_0 + \frac{\delta}{2}\sigma_z + \frac{\Omega}{2}(\sigma_x \cos 2k_L x - \sigma_y \sin 2k_L x), \tag{5.13}$$

where we have added an overall constant $\delta/2$. $\Omega = \Omega_R/\sqrt{2}$ characterizes the Raman coupling, and σ_x, σ_y, σ_z are the usual 2 by 2 Pauli Matrix. The bare Hamiltonian in its matrix form is:

$$H_0 = \begin{pmatrix} \frac{\hat{p}^2}{2m} + \frac{\delta}{2} & \frac{1}{2}\Omega e^{2ik_L x} \\ \frac{1}{2}\Omega e^{-2ik_L x} & \frac{\hat{p}^2}{2m} - \frac{\delta}{2} \end{pmatrix}, \tag{5.14}$$

for the spin-$\frac{1}{2}$ subspace wave functions

$$\Psi(\mathbf{r}) = \begin{pmatrix} \Psi_\uparrow(\mathbf{r}) \\ \Psi_\downarrow(\mathbf{r}) \end{pmatrix}. \tag{5.15}$$

In the Hamiltonian Eq. 5.14, we see that all atomic kinetic energy and Zeeman effect enter the diagonal terms, while the off-diagonal terms capture the Raman coupling of the spin-$\uparrow$ and spin-$\downarrow$ states.

The spin-orbit coupling form of the Hamiltonian emerges once we make a unitary rotation. We define the unitary rotation matrix as

$$\hat{U} = e^{ik_L x \sigma_z} = \begin{pmatrix} e^{ik_L x} & 0 \\ 0 & e^{-ik_L x} \end{pmatrix} = \mathrm{e}^{i\mathbf{k}_L \cdot \mathbf{r}\sigma_z}. \tag{5.16}$$

Let

$$\tilde{\Psi}(\mathbf{r}) = \hat{U}^\dagger \Psi(\mathbf{r}), \tag{5.17}$$

and call the transformed eigenfunctions $\tilde{\Psi}$ the rotated basis or the dressed states (with respect to the 'original basis' before rotation). Since

$$\hat{U}^\dagger H_0 \hat{U} = \begin{pmatrix} \frac{\hat{p}^2}{2m} + \frac{\hbar k_L \hat{p}_x}{m} + \frac{\hbar^2 {k_L}^2}{2m} + \frac{\delta}{2} & \frac{1}{2}\Omega \\ \frac{1}{2}\Omega & \frac{\hat{p}^2}{2m} - \frac{\hbar k_L \hat{p}_x}{m} + \frac{\hbar^2 {k_L}^2}{2m} - \frac{\delta}{2} \end{pmatrix}, \tag{5.18}$$

the bare Hamiltonian can be rewritten as

$$\mathcal{H}_0 = \int d^3r\, \tilde{\Psi}^\dagger (\frac{\hat{p}^2}{2m}\sigma_0 + 2\hbar\alpha\hat{p}_x\sigma_z + \frac{\delta}{2}\sigma_z + \frac{\Omega}{2}\sigma_x)\tilde{\Psi}, \tag{5.19}$$

where the second term represents spin-orbit coupling. A constant $\hbar^2{k_L}^2/2m$ has been dropped in the above Hamiltonian. Here $\alpha = k_L/2m$ and $\hbar^2{k_L}^2/2m \equiv E_L$ is defined as the recoil energy. This Hamiltonian is the starting point in Ref. [34] after a rotation of axes $\hat{\mathbf{x}} \to \hat{\mathbf{z}}$, $\hat{\mathbf{z}} \to \hat{\mathbf{y}}$, $\hat{\mathbf{y}} \to \hat{\mathbf{x}}$.

Meanwhile, let's look at the transformed wave function in the momentum space:

$$\begin{aligned}\tilde{\Psi}(\mathbf{p}) &= \int d^3r\, e^{-i\mathbf{p}\cdot\mathbf{r}}\tilde{\Psi}(\mathbf{r}) = \int d^3r\, e^{-i\mathbf{p}\cdot\mathbf{r}} U^\dagger \begin{pmatrix} \Psi_\uparrow(\mathbf{r}) \\ \Psi_\downarrow(\mathbf{r}) \end{pmatrix} \\ &= \int d^3r \begin{pmatrix} e^{-i\mathbf{p}\cdot\mathbf{r}-ik_Lx}\Psi_\uparrow(\mathbf{r}) \\ e^{-i\mathbf{p}\cdot\mathbf{r}+ik_Lx}\Psi_\downarrow(\mathbf{r}) \end{pmatrix} = \begin{pmatrix} \Psi_\uparrow(\mathbf{p}+k_L\mathbf{x}) \\ \Psi_\downarrow(\mathbf{p}-k_L\mathbf{x}) \end{pmatrix}\end{aligned} \tag{5.20}$$

where standard Fourier transform is applied. This means the corresponding wave-function in the momentum space is shifted or "boosted" by $\pm k_L$, depending on the spin, by the same transformation.

In the next chapter, we will construct an effective low-energy theory for both the bare and interacting parts of the Hamiltonian in the space of the dress states, and apply the effective theory to investigate the phases transitions in bosons with spin-orbit coupling.

CHAPTER 6
PHASES IN BOSONS WITH SPIN-ORBIT COUPLING

In the previous chapter, we briefly introduced the experimental and theoretical aspects of bosons with spin-orbit coupling. In this chapter, we study the Hamiltonian realized in Ref. [34] in detail, with the aim of discerning experimental signatures of the mixed-BEC state. In this phase, the system condenses into a superposition of two plane wave states. This phase, which should exhibit real-space density modulations (due to interference of these two plane waves), is stable for sufficiently small light-atom coupling. We then invoke the local density approximation to argue that, generally, the phase diagram at fixed chemical potential implies an unusual density dependence of the trapped mixed-BEC phase. Finally, we calculate the frequency of Bogoliubov sound modes for the mixed BEC phase, showing that this vanishes as the phase transition out of the mixed phase is approached (as a function of light-atom coupling. Most of the results in this chapter has been published in Ref. [61].

6.1 Model

6.1.1 Band Structure of the Bare Hamiltonian

In this section, we analyze the band structure of the bare Hamiltonian Eq. 5.19 to construct a low-energy effective Hamiltonian. We begin by writing the bare Hamiltonian equivalently as,

$$\hat{H}_r(\mathbf{p},\delta) = \frac{1}{2m}(\mathbf{p}^2 + \mathbf{k}_L^2) + \frac{1}{2}\delta\sigma_z + \frac{1}{2}\Omega\sigma_x + \frac{1}{m}k_L\sigma_z\hat{p}_x, \tag{6.1}$$

This chapter was adapted from Q.-Q. Lü and Daniel E. Sheehy, Phys. Rev. A **88**, 043645 (2013).

with the final term being the effective light-induced spin-orbit coupling $\hat{H}_{\mathrm{SOC}} = \frac{1}{m}k_L\sigma_z\hat{p}_x$. In Eq. 6.1 and below, we choose units such that $\hbar = 1$.

It is straightforward to obtain the eigenvalues of $\hat{H}_r(\mathbf{p}, \delta)$ (which are also the eigenvalues of Eq. 5.14):

$$\varepsilon_{\pm}(\mathbf{p}) = \frac{\mathbf{p}^2 + k_L^2}{2m} \pm \sqrt{\frac{\Omega^2 + \delta^2}{4} + \frac{k_L^2 p_x^2}{m^2} + \frac{\delta k_L p_x}{m}}, \tag{6.2}$$

plotted in Fig. 6-1 for the case of $\delta = 0$ (solid curves) and $\delta > 0$ (dashed curves). For each of the two cases, there are one upper band and one lower band, the latter of which interests us the most, since it possesses the double-well shape shown in Fig. $6-1$ (for sufficiently small Ω and δ). At the $\delta = 0$ limit, the lower band has two degenerate ground states

$$\varepsilon_-(\pm\mathbf{p}_0) = -\frac{\Omega^2}{16E_L} \approx 0, \tag{6.3}$$

at

$$\pm\, p_0 = \pm k_L\sqrt{1 - \frac{\Omega^2}{16{E_L}^2}} \approx \pm k_L, \tag{6.4}$$

where both approximated results assume the limit $\Omega \ll E_L$. When $\delta \neq 0$, by solving $\frac{d\varepsilon_-(\mathbf{p})}{d\mathbf{p}} = 0$ we find the minima of the lower band at

$$p_{r,\ell} \simeq \pm k_L\sqrt{1 - \hat{\Omega}^2} + k_L\hat{\delta}\frac{\hat{\Omega}^2}{1 - \hat{\Omega}^2}, \tag{6.5}$$

where the dimensionless coupling $\hat{\Omega} \equiv \Omega/4E_L$, and the dimensionless Zeeman energy difference $\hat{\delta} = \delta/4E_L$, with the recoil energy $E_L \equiv k_L^2/2m$. Note that $\mathbf{p}_{r,\ell}$ are not symmetric about $p = 0$ for non-zero δ. The energies of the local minima are

$$\varepsilon_-(\mathbf{p}_{r/\ell}) = E_L(\hat{\Omega}^2 \pm 2\hat{\delta}), \tag{6.6}$$

with the $-$ $(+)$ corresponding to the right (left) minima.

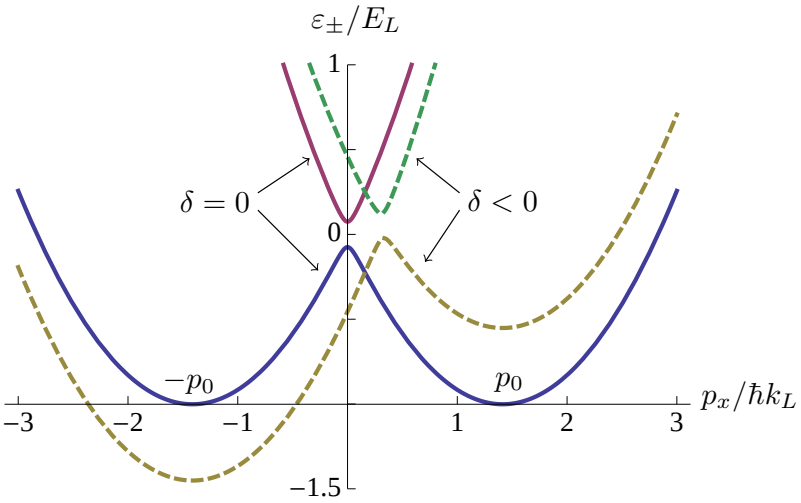

Figure 6-1: This plot shows the eigenvalues $\varepsilon_\pm(\mathbf{p})$, at $p_y = p_z = 0$ and as a function of p_x. The solid lines are the case of $\delta = 0$, while the dashed lines show the experimentally-relevant case of $\delta < 0$. The left and right minima are the $\uparrow'$ and $\downarrow'$ dressed states. In the absence of interactions, the system will condense into the left minimum (the $\uparrow'$ dressed state).

In the absence of interactions, for $\delta = 0$, this system would have two degenerate ground states at the minima of the double well shown in Fig. $6-1$.

Our aim is to determine the phase diagram of this system as a function of the tunable parameters of this system, which are the energy difference δ and the light-atom coupling Ω. In the next section we begin this task by analyzing the low energy states of H_r occuring near the minima of Fig. $6-1$.

6.1.2 Low-Energy Effective Hamiltonian

Following Lin et al [32], we proceed to construct a low-energy Hamiltonian focusing on states near these two minima. The dressed spin states operators are constructed from the original states operators as: $\psi_{\uparrow'}(\mathbf{p}) \equiv \psi_-(\mathbf{p} + \mathbf{p}_\ell)$ and $\psi_{\downarrow'}(\mathbf{p}) \equiv \psi_-(\mathbf{p} + \mathbf{p}_r)$. Here, $\psi_\sigma(\mathbf{p})$ $(\sigma = \uparrow', \downarrow')$ is an annihilation operator for a dressed spin

state. With the details relegated to the Appendix I, we find the approximate form of the single-particle Hamiltonian:

$$\mathcal{H}_0 = \sum_{\mathbf{p}} \sum_{\sigma=\uparrow',\downarrow'} (\varepsilon_\sigma(\mathbf{p}) - \mu_\sigma)\psi^\dagger_\sigma(\mathbf{p})\psi_\sigma(\mathbf{p}), \tag{6.7}$$

where we included a chemical potential μ that couples to the density and defined $\mu_{\uparrow'} = \mu - \frac{1}{2}\delta$ and $\mu_{\downarrow'} = \mu + \frac{1}{2}\delta$. The effective dispersion is

$$\varepsilon(\mathbf{p}) = \frac{1}{2m^*}p_x^2 + \frac{1}{2m}(p_y^2 + p_z^2), \tag{6.8}$$

equal to the bare dispersion in the y and z directions, and reflecting the curvature of the minima of $\varepsilon_-(\mathbf{p})$, that satisfies $(m^*)^{-1} = m^{-1}(1 - \hat{\Omega}^2)$, in the x direction. As discussed in Appendix I, Eq. 6.7 is valid at sufficiently small atom-light coupling and Zeeman energy difference, i.e., $\hat{\Omega} \ll 1$ and $\hat{\delta} \ll 1$.

Having obtained an approximate form for the effective single-particle Hamiltonian, we perform a similar analysis on the interaction Hamiltonian. From Chapter 2.5, the interaction Hamiltonian for a BEC with two species of bosons is

$$\begin{aligned}\mathcal{H}_{int} &= \frac{1}{2}\int d^3r\, [c_0(n_\uparrow + n_\downarrow)^2 + c_2(2n_\uparrow n_\downarrow + {n_\downarrow}^2)] \\ &= \frac{1}{2}\int d^3r \Big[(c_0 + c_2)n_\downarrow^2 + c_0 n_\uparrow^2 + 2(c_0 + c_2)n_\uparrow n_\downarrow\Big],\end{aligned} \tag{6.9}$$

where c_0 and c_2 are interaction parameters, $n_\sigma = \Psi^\dagger_\sigma \Psi_\sigma$ with $\sigma = \uparrow, \downarrow$ and normal ordering is implied. The single particle Hamiltonian Eq. 6.7 possesses an exact degeneracy, at $\delta = 0$, among the $\uparrow'$ and $\downarrow'$ states; however the interaction Hamiltonian does not possess this symmetry.

With details in Appendix. *I*, by approximating the low energy expansion of the original wave function and inserting into Eq. 6.9, the interaction Hamiltonian for

the dressed spins is obtained as:

$$\mathcal{H}_1 = \frac{1}{2}\int d^3r \left[g_{\uparrow'\uparrow'}|\psi_{\uparrow'}(\mathbf{r})|^4 + g_{\downarrow'\downarrow'}|\psi_{\downarrow'}(\mathbf{r})|^4 + 2g_{\uparrow'\downarrow'}|\psi_{\uparrow'}(\mathbf{r})|^2|\psi_{\downarrow'}(\mathbf{r})|^2 \right], \tag{6.10}$$

where $\psi_\sigma(\mathbf{r})$ is the corresponding field operator, the Fourier transform of $\psi_\sigma(\mathbf{p})$. The interaction parameters are [34]:

$$g_{\uparrow'\uparrow'} = c_0, \tag{6.11}$$

$$g_{\downarrow'\downarrow'} = c_0 + c_2, \tag{6.12}$$

$$g_{\uparrow'\downarrow'} = c_0 + c_2 + \frac{c'_{\uparrow\downarrow}}{2} \tag{6.13}$$

with the couplings $c_0 = 4\pi(a_0 + 2a_2)/3m$ and $c_2 = 4\pi(a_2 - a_0)/3m$ [60]. In the regimes of this experiment, $c'_{\uparrow\downarrow} = 2c_0\hat{\Omega}^2 > 0$. We have noted in Sec. 2.5 that for ^{87}Rb the scattering lengths a_2 and a_0 are almost equal. Ref. [60] quoted the theoretical results $a_0 = 101.78a_B$, $a_2 = 100.40a_B$ (implying $a_2 - a_0 = -1.38a_B$) and experimentally measured the difference as $a_2 - a_0 = -1.07a_B$ (implying $a_2 = 100.71a_B$), with $a_\mathrm{B} = 5.29177 \times 10^{-11}$m the Bohr radius. Plugging the theoretical values of a_0 and a_2, we obtain the theoretical value of c_0

$$\frac{c_0}{h} = 7.80 \times 10^{-12}\mathrm{Hz\,cm^3}, \tag{6.14}$$

and the theoretical value of c_2

$$\frac{c_2}{h} = -3.55 \times 10^{-14}\mathrm{Hz\,cm^3}. \tag{6.15}$$

Both theoretical values are consistent with the values quoted by Ref. [34] ($c_0/h = 7.79 \times 10^{-12}\mathrm{Hz\,cm^3}$ and $c_2/h = -3.61 \times 10^{-14}\mathrm{Hz\,cm^3}$.). It is possible that other

works use interaction parameters c_0 and c_2 based on experimental values of a_0 and a_2, but again the two groups of values are still close to each other.

From the above calculation, we see in the experimental regimes of Ref. [34], we have $c_0 > 0$, $c_2 < 0$, and $|c_2| \ll c_0$. Therefore the $\uparrow$ bosons having a larger intraspecies repulsion than the $\downarrow$ bosons. This imbalance has important implications for the allowed phases in the boson gas.

6.2 Phase Diagram

In the present section, we derive the phase diagram for the two species, using the mean-field approximation. Our full system Hamiltonian is $\mathcal{H} = \mathcal{H}_0 + \mathcal{H}_1$, with $\mathcal{H}_0$ given in Eq. 6.7 and $\mathcal{H}_1$ given in Eq. 6.10. We assume spatially uniform expectation values $\langle \psi_\sigma \rangle$ and analyze the expectation values of the Hamiltonian.

There are two equivalent approaches to describe a system: fixing the particle number (or fixed density since the volume does not change) or fixing the chemical potential. Next, we derive the phase diagrams of each ensemble, then discuss the connections between the two diagrams and their implications.

In this section, we do not limit ourselves in the specific regimes of interaction parameters in the Spielman experiment [34]. Instead, we assume a wider range of interaction parameters $c'_{\uparrow\downarrow}/c_0$ and c_2/c_0, both could be positive or negative, so that the phase transitions can occur in the full parameter space. Then we look into the experimental range for discussion.

6.2.1 Fixed Density Phase Diagram

In this part, we derive the phase diagram when the particle numbers $N_{\uparrow'}$ and $N_{\downarrow'}$ are independently fixed. In a boson gas of two species, there are two possible

phases: a mix of the two states (Phase Mixed, indicated by PM below), and a separation between the two states (Phase Separated, indicated by PS). We analyze the expectation value of $\mathcal{H}_1$ by assuming each of the two cases.

In the mixed phase, each species occupies the entire volume V, so the expectation of the densities $\langle n_{\uparrow'} \rangle = N_{\uparrow'}/V$ and $\langle n_{\downarrow'} \rangle = N_{\downarrow'}/V$. The expectation value of the interaction Hamiltonian becomes

$$\begin{aligned} \langle \mathcal{H}_1 \rangle_{PM} =& \frac{1}{2V}[(c_0 + \frac{c_2}{2})N^2 + \frac{c_2}{2}({N_{\downarrow'}}^2 - {N_{\uparrow'}}^2) + (c_2 + c'_{\uparrow\downarrow})N_{\uparrow'}N_{\downarrow'}] \\ =& \frac{1}{2V}[(c_0 + c_2){N_{\downarrow'}}^2 + c_0{N_{\uparrow'}}^2 + 2(c_0 + \frac{c'_{\uparrow\downarrow}}{2} + c_2)N_{\uparrow'}N_{\downarrow'}], \end{aligned} \tag{6.16}$$

where $N = N_{\uparrow'} + N_{\downarrow'}$ is the total particle number.

Meanwhile, when the phases are separated, each species occupies their own space, respectively $V_{\uparrow'}$ and $V_{\downarrow'}$. The expectation value of the interaction Hamiltonian is

$$\begin{aligned} \langle \mathcal{H}_1 \rangle_{PS} &= \frac{1}{2}[(c_0 + \frac{c_2}{2})(V_{\uparrow'}\frac{{N_{\uparrow'}}^2}{V_{\uparrow'}^2} + V_{\downarrow'}\frac{{N_{\downarrow'}}^2}{V_{\downarrow'}^2}) + \frac{c_2}{2}(V_{\downarrow'}\frac{{N_{\downarrow'}}^2}{V_{\downarrow'}^2} - V_{\uparrow'}\frac{{N_{\uparrow'}}^2}{V_{\uparrow'}^2})] \\ &= \frac{c_0}{2}\frac{{N_{\uparrow'}}^2}{V_{\uparrow'}} + \frac{c_0 + c_2}{2}\frac{{N_{\downarrow'}}^2}{V_{\downarrow'}}, \end{aligned} \tag{6.17}$$

where the total volume $V = V_{\uparrow'} + V_{\downarrow'}$. The expectation values of cross terms proportional to $n_{\uparrow'}n_{\downarrow'}$ vanish because the two species occupy separate volumes. We don't know what $V_{\uparrow'}$ and $V_{\downarrow'}$ are, but because they are not independent, we can choose one of them as the independent variable and minimize $\langle \mathcal{H}_1 \rangle_{PS}$ with respect to it. Thus we obtain the stationary condition

$$-\frac{1}{2}c_0\frac{{N_{\uparrow'}}^2}{{V_{\uparrow'}}^2} + \frac{1}{2}(c_0 + c_2)\frac{{N_{\downarrow'}}^2}{(V - V_{\uparrow'})^2} = 0, \tag{6.18}$$

from which we solve for $V_{\uparrow'}$. Therefore, the minimum $\langle \mathcal{H}_1 \rangle_{PS}$ is

$$\langle \mathcal{H}_1 \rangle_{PS} = \frac{1}{2V}[(c_0 + c_2){N_{\downarrow'}}^2 + c_0{N_{\uparrow'}}^2 + 2\sqrt{c_0(c_0 + c_2)}N_{\uparrow'}N_{\downarrow'}]. \tag{6.19}$$

For the system to be in the phase mixed state, it is required that

$$\langle \mathcal{H}_1 \rangle_{PM} < \langle \mathcal{H}_1 \rangle_{PS}\,, \tag{6.20}$$

which is

$$\sqrt{c_0(c_0 + c_2)} > c_0 + c_2 + \frac{c'_{\uparrow\downarrow}}{2}. \tag{6.21}$$

This agrees with Ref. [34].

The phase diagram showing the phase mixed and phase separated states is shown in Fig. $6-2$. The blue curve is the phase boundary described in Eq. 6.21. The other root of the condition Eq. 6.20, is $\sqrt{c_0(c_0 + c_2)} < -c_0 - c_2 - \frac{c'_{\uparrow\downarrow}}{2}$, plotted as the red line in Fig. $6-2$. It is the boundary between the phase mixed and an unstable region, which will be explained below.

6.2.2 Fixed Chemical Potential Phase Diagram

We now analyze the phase separation condition at fixed chemical potential. We keep the chemical potentials $\mu_{\uparrow'}$ and $\mu_{\downarrow'}$ (related with the chemical potential μ when the two species are balanced, i.e. $\delta = 0$, by $\mu_{\uparrow'} = \mu - \frac{\delta}{2}$ and $\mu_{\downarrow'} = \mu + \frac{\delta}{2}$) unchanged, and find the minimizing condition for the grand free energy. After obtaining the phase boundary, we then discuss the phase diagram for different values of chemical potentials.

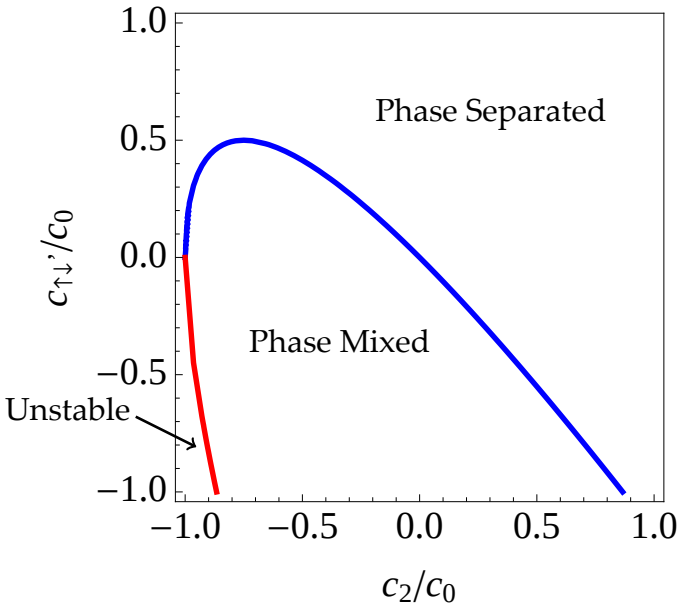

Figure 6-2: Phase diagram for bosons with SOC at fixed density (fixed particle number), showing the phases of the bosons as a function of interaction parameters c_2/c_0 and $c'_{\uparrow\downarrow}/c_0$. The blue curve is the phase boundary between the phase mixed and the phase separated, as described in Eq. 6.21, the red curve is the boundary between the phase mixed and an unstable region (explained below).

Solving for the Phases

The grand free energy is $\mathcal{F} = \int d^3r\, F$, where

$$F = -\mu_{\uparrow'} \left|\psi_{\uparrow'}\right|^2 - \mu_{\downarrow'} \left|\psi_{\downarrow'}\right|^2 + H_1, \tag{6.22}$$

where the kinetic energy in the low-energy effective Hamiltonian Eq. 6.7 has been omitted due to the assumption of the wave functions' spatial uniformity, and the interaction term is

$$H_1 = \frac{c_0}{2}|\psi_{\uparrow'}|^4 + \frac{c_0 + c_2}{2}|\psi_{\downarrow'}|^4 + (c_0 + c_2 + \frac{c'_{\uparrow\downarrow}}{2})|\psi_{\uparrow'}|^2|\psi_{\downarrow'}|^2. \tag{6.23}$$

From Euler-Lagrange equation, we minimize the grand potential with respect to the two species $\frac{\partial F}{\partial \psi_{\uparrow'}} = 0$ and $\frac{\partial F}{\partial \psi_{\downarrow'}} = 0$. Besides the trivial solution $\psi_{\uparrow'} = 0, \psi_{\downarrow'} = 0$,

we obtain

$$\mu_{\uparrow'} = c_0|\psi_{\uparrow'}|^2 + (c_0 + c_2 + \frac{c'_{\uparrow\downarrow}}{2})|\psi_{\downarrow'}|^2, \tag{6.24a}$$

$$\mu_{\downarrow'} = (c_0 + c_2)|\psi_{\downarrow'}|^2 + (c_0 + c_2 + \frac{c'_{\uparrow\downarrow}}{2})|\psi_{\uparrow'}|^2, \tag{6.24b}$$

from which we solved three distinct solutions. Together with the trivial noncondensed solution, the four solutions are

$$1. \quad \psi_{\uparrow'} = 0, \psi_{\downarrow'} = 0 \tag{6.25a}$$

$$2. \quad \psi_{\uparrow'} = 0, \left|\psi_{\downarrow'}\right|^2 = \frac{\mu_{\downarrow'}}{c_0 + c_2} \tag{6.25b}$$

$$3. \quad \left|\psi_{\uparrow'}\right|^2 = \frac{\mu_{\uparrow'}}{c_0}, \psi_{\downarrow'} = 0 \tag{6.25c}$$

$$4. \quad \left|\psi_{\uparrow'}\right|^2 = \frac{(c_0 + c_2)\mu_{\uparrow'} - (c_0 + c_2 + \frac{c'_{\uparrow\downarrow}}{2})\mu_{\downarrow'}}{(c_0 + c_2)c_0 - (c_0 + c_2 + \frac{c'_{\uparrow\downarrow}}{2})^2},$$

$$\left|\psi_{\downarrow'}\right|^2 = \frac{c_0\mu_{\downarrow'} - (c_0 + c_2 + \frac{c'_{\uparrow\downarrow}}{2})\mu_{\uparrow'}}{(c_0 + c_2)c_0 - (c_0 + c_2 + \frac{c'_{\uparrow\downarrow}}{2})^2}. \tag{6.25d}$$

The corresponding minimized grand free energies are

$$F_1 = 0 \tag{6.26a}$$

$$\frac{F_2}{V} = -\frac{1}{2}\frac{{\mu_{\downarrow'}}^2}{c_0 + c_2} \tag{6.26b}$$

$$\frac{F_3}{V} = -\frac{1}{2}\frac{{\mu_{\uparrow'}}^2}{c_0} \tag{6.26c}$$

$$\frac{F_4}{V} = -\frac{\frac{1}{2}(c_0 + c_2){\mu_{\uparrow'}}^2 - (c_0 + c_2 + \frac{c'_{\uparrow\downarrow}}{2})\mu_{\uparrow'}\mu_{\downarrow'} + \frac{c_0}{2}{\mu_{\downarrow'}}^2}{(c_0 + c_2)c_0 - (c_0 + c_2 + \frac{c'_{\uparrow\downarrow}}{2})^2}. \tag{6.26d}$$

Two of these solutions refer to the case in which only one of $\psi_{\downarrow'}$ or $\psi_{\uparrow'}$ is condensed. We call these two solutions BEC $\downarrow'$ and BEC $\uparrow'$ phases, respectively (or simply, $\downarrow'$ and $\uparrow'$), referring to the condensed species. The last solution is the mixed phase,

in which both species are condensed. Written in the matrix form, the mixed phase solution is (defining $n_\sigma = |\psi_\sigma|^2$ for the mean-field densities of the two species)

$$\begin{pmatrix} n_{\uparrow'} \\ n_{\downarrow'} \end{pmatrix} = \frac{1}{D} \begin{pmatrix} c_0 + c_2 & -c_0 - c_2 - \frac{c'_{\uparrow\downarrow}}{2} \\ -c_0 - c_2 - \frac{c'_{\uparrow\downarrow}}{2} & c_0 \end{pmatrix} \begin{pmatrix} \mu_{\uparrow'} \\ \mu_{\downarrow'} \end{pmatrix}, \tag{6.27}$$

where we defined the denominator

$$D = (c_0 + c_2)c_0 - (c_0 + c_2 + \frac{c'_{\uparrow\downarrow}}{2})^2, \tag{6.28}$$

which, in the fixed number ensemble, determines the phase separation boundary which is $D = 0$ (as discussed below).

Stability

The stable state of the four solutions in Eq. 6.25 is decided by the lowest of the free energies in Eq. 6.26. Since $c_0 > 0$, F_1 cannot be the minimum anywhere due to the fact that the $\uparrow'$ solution always has lower energy (the chemical potentials being positive do not allow the trivial solution to occur either). Now we discuss the remaining three solutions.

Since the free energies depend on the values of chemical potentials $\mu_{\sigma'}$, we have to discuss different chemical potential values to determine the phases of the system, hence giving a complete phase diagram. But without going into specific discussion, we can first identify the stable regime of the mixed phase by utilizing an analysis of the Hessian Matrix.

A stable mixed phase necessitates that the determinant of the Hessian $H(\psi_i, \psi_j) = \frac{\partial^2 F}{\partial \psi_i \partial \psi_j}$ is positive, and that $\frac{\partial^2 F}{\partial \psi^2_{\uparrow'}} > 0$ or $\frac{\partial^2 F}{\partial \psi^2_{\downarrow'}} > 0$. Since

$$\frac{\partial^2 F}{\partial \psi_{\uparrow'}^2} = 2\frac{\partial F}{\partial n_{\uparrow'}} + (2\psi_{\uparrow'})^2 \frac{\partial^2 F}{\partial n_{\uparrow'}^2}, \tag{6.29}$$

$$\frac{\partial^2 F}{\partial \psi_{\downarrow'}^2} = 2\frac{\partial F}{\partial n_{\downarrow'}} + (2\psi_{\downarrow'})^2 \frac{\partial^2 F}{\partial n_{\downarrow'}^2}, \tag{6.30}$$

$$\frac{\partial^2 F}{\partial \psi_{\uparrow'} \partial \psi_{\downarrow'}} = 4\psi_{\downarrow'}\psi_{\uparrow'} \frac{\partial^2 F}{\partial n_{\uparrow'} \partial n_{\downarrow'}}. \tag{6.31}$$

When F is minized, $\frac{\partial F}{\partial n_{\uparrow'}} = \frac{\partial F}{\partial n_{\downarrow'}} = 0$. We have the following proportional relationship for Hessians at the stationary points

$$\frac{\partial^2 F}{\partial \psi_{\uparrow'}^2}\frac{\partial^2 F}{\partial \psi_{\downarrow'}^2} - (\frac{\partial^2 F}{\partial \psi_{\uparrow'} \partial \psi_{\downarrow'}})^2 = 16 n_{\uparrow'} n_{\downarrow'} [\frac{\partial^2 F}{\partial n_{\uparrow'}^2}\frac{\partial^2 F}{\partial n_{\uparrow'}^2} - (\frac{\partial^2 F}{\partial n_{\uparrow'} \partial n_{\downarrow'}})^2]. \tag{6.32}$$

Therefore the stability requirement is equivalent to evaluating all the derivatives with respect to $n_{\uparrow'}$ and $n_{\downarrow'}$. The determinant of the Hessian matrix

$$\det H(n_{\uparrow'}, n_{\downarrow'}) = \frac{\partial^2 F}{\partial n_{\uparrow'}^2}\frac{\partial^2 F}{\partial n_{\uparrow'}^2} - (\frac{\partial^2 F}{\partial n_{\uparrow'} \partial n_{\downarrow'}})^2 = c_0(c_0 + c_2) - (c_0 + c_2 + \frac{{c'_{\uparrow\downarrow}}^2}{2})^2 > 0. \tag{6.33}$$

The conditions $\frac{\partial^2 F}{\partial n_{\uparrow'}^2} > 0$ and $\frac{\partial^2 F}{\partial n_{\downarrow'}^2}$ imply $c_0 > 0$ and $c_0 + c_2 > 0$. Together with $c_0(c_0 + c_2) - (c_0 + c_2 + \frac{{c'_{\uparrow\downarrow}}^2}{2})^2 > 0$, the boundaries for the region in which the mixed phase is stable are set.

When outside the mixed phase, however, the above analysis does not hold, since one of $\psi_{\sigma'}$ is zero. Therefore, any place in the parameter space of c_2/c_0 and $c'_{\uparrow\downarrow}$, we need to compare the grand free energies for the three solutions F_2, F_3, and F_4 to find the stable phase, which is, without further ado, discussed in the following. Note that we assume positive chemical potentials unless otherwise noted. The case of negative chemical potential is individually discussed towards the end of the analysis.

Phase Diagram: $\mu_{\downarrow'}$=$\mu_{\uparrow'}$

Now we determine the stable phase for the case of equal chemical potential and derive the phase diagram. When setting $\mu_{\downarrow'}$ and $\mu_{\uparrow'}$ equal, by equating F_2, F_3 and F_4, the phase boundary is determined as

$$c_2 = 0, c'_{\uparrow\downarrow} = 0, c'_{\uparrow\downarrow} = -2c_2 \tag{6.34}$$

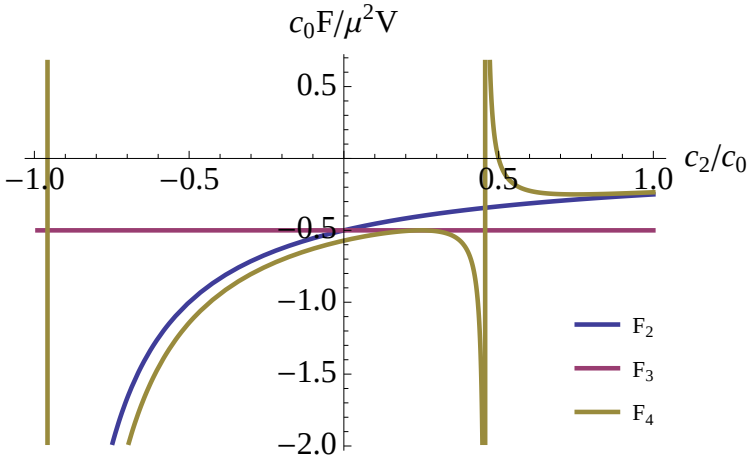

Figure 6-3: In this graph we compare the three free energy solutions F_2, F_3, F_4, which correspond to the $\downarrow'$, the $\uparrow'$ and the phase mixed states, respectively. We plot the solutions against varying c_2 when $c'_{\uparrow\downarrow} = -0.5c_0$. The stable phase of the system is determined by the lowest grand potential, unless under that solution the density becomes unphysically negative (as occurred in some intervals in this graph, see analysis in the main text). Here we work in the fixed chemical potential ensemble and assume $\mu_{\uparrow'} = \mu_{\downarrow'} = \mu$.

Fig. $6-3$ compares the three free energy solutions F_2, F_3, F_4 with varying c_2 and $c'_{\uparrow\downarrow} = -0.5c_0$. We see that: for the case $c'_{\uparrow\downarrow} < 0$, when $c_2 < -c'_{\uparrow\downarrow}/2$, F_4 is smallest, the mixed phase is the stable state; when $c_2 > -c'_{\uparrow\downarrow}/2$, F_3 is smallest, $\uparrow'$ is the stable phase. Note that in the region of c_2 immediately larger than $-c'_{\uparrow\downarrow}/2$, although F_4 appears to be the lowest state, the density of the atoms becomes negative beyond this point, indicating that the mixed state is unstable here and the true boundary is at $c_2 = -c'_{\uparrow\downarrow}/2$.

From Eq. 6.25, the boson densities of the two species for equal chemical potential are: for the $\downarrow'$ region, $\psi_{\uparrow'} = 0$, $|\psi_{\downarrow'}|^2 = \frac{\mu}{c_0+c_2}$; for the $\uparrow'$ region, $|\psi_{\uparrow'}|^2 = \frac{\mu}{c_0}$, $\psi_{\downarrow'} = 0$; for the phase mixed region,

$$|\psi_{\uparrow'}|^2 = \frac{-\frac{c'_{\uparrow\downarrow}}{2}\mu}{(c_0+c_2)c_0 - (c_0+c_2+\frac{c'_{\uparrow\downarrow}}{2})^2}, \quad |\psi_{\downarrow'}|^2 = \frac{-(\frac{c'_{\uparrow\downarrow}}{2}+c_2)\mu}{(c_0+c_2)c_0 - (c_0+c_2+\frac{c'_{\uparrow\downarrow}}{2})^2}.$$

Fig. $6-4$ shows the change of densities when c_2 is gradually tuned larger and $c'_{\uparrow\downarrow}$ is kept unvaried at $-0.5c_0$.

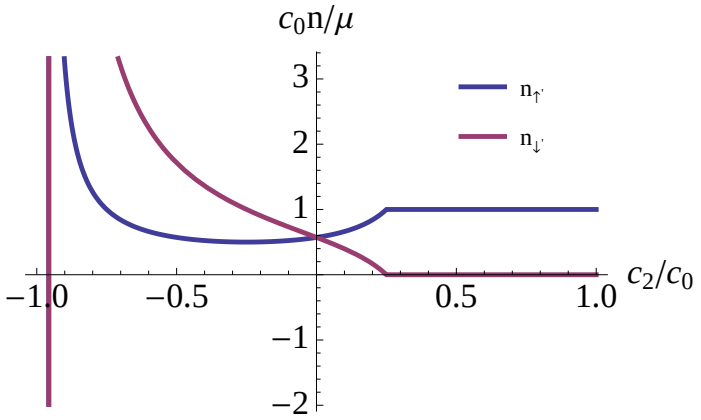

Figure 6-4: This graph shows at fixed chemical potentials $\mu_{\uparrow'} = \mu_{\downarrow'} = \mu$, the densities of the two dressed spin state species $n_{\uparrow'}$ and $n_{\downarrow'}$ change when c_2 is varied and $c_{\uparrow\downarrow'}$ is kept at$-0.5c_0$. When both densities are non-zero, the system is in the mixed-BEC state.

Similarly, for the case $c'_{\uparrow\downarrow} > 0$, when $c_2 < 0$, F_2 is smallest, $\uparrow'$ is the stable state; when $c_2 > 0$, F_3 is smallest, $\uparrow'$ is the stable phase. The false minimum of F_4 still needs to be taken into account. Fig. $6-5$ shows the trend of densities with varying c_2 when $c'_{\uparrow\downarrow}$ is at $0.25c_0$. We see, for this case, there is no mixed-BEC state. An entirely analogous analysis can be done for the stable state when c_2 is kept unchanged and $c_{\uparrow\downarrow'}$ varies too.

Combining all the above discussion, we are able to determine the stable phase in the entire phase diagram for fixed chemical potential. Fig. $6-6$ shows the diagram

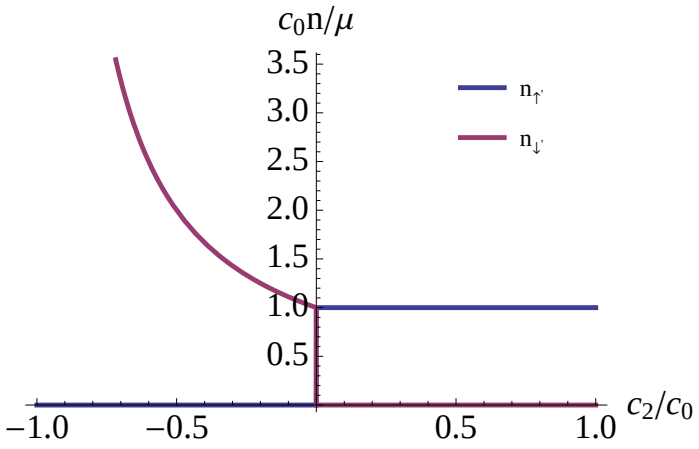

Figure 6-5: This graph shows at fixed chemical potentials $\mu_{\uparrow'} = \mu_{\downarrow'} = \mu$, the densities of the two dressed spin state species $n_{\uparrow'}$ and $n_{\downarrow'}$ change when c_2 is varied and $c_{\uparrow\downarrow'}$ is at $0.25c_0$.

when $\mu_{\uparrow'} = \mu_{\downarrow'}$. The phase diagrams Fig. $6-2$ and Fig. $6-6$ are interconnected in such a way that the contour in Fig. $6-2$ is where F_4 blows up in Fig. $6-6$.

Consider a system right in the center of the fixed μ phase diagram Fig. $6-6$ at $c_2 = 0$, $c'_{\uparrow\downarrow} = 0$. F_2, F_3 and F_4 are equal at this point, meaning a system that transits from phase mixed to phase separated with both $\uparrow'$ and $\downarrow'$ species present has to pass through this point since this is the only condition with which these states can co-exist. Therefore, this center point has to fall on the phase boundary curve in the fixed particle number diagram Fig. $6-2$.

According to Eq. $6.25d$, the spin-$\uparrow'$ and the spin-$\downarrow'$ densities diverge when the denominator vanishes, along the phase boundary in Fig. $6-2$. The divergence along the upper blue curve at $\mu_{\uparrow'} = \mu_{\uparrow'} > 0$ represents the phase transition into the mixed, meanwhile the divergence along the lower red curve marks the transition into the unstable regime, as proved by the analysis of the Hessian matrix. We also include that section of the phase boundary into the phase diagram Fig. $6-2$.

Next, we discuss the phase diagram for the general case $\mu_{\downarrow'} \neq \mu_{\uparrow'}$.

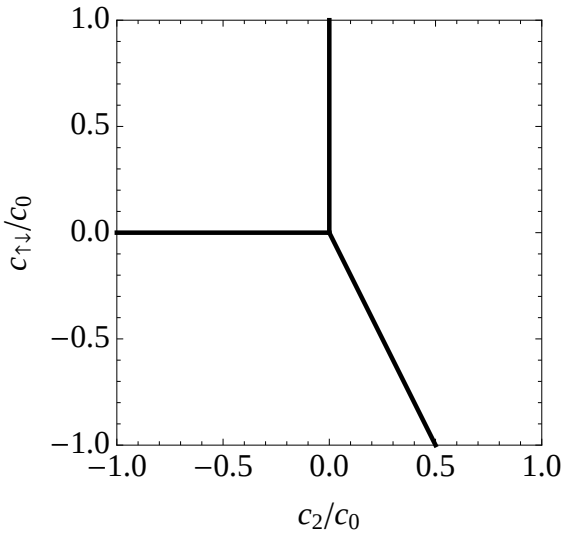

Figure 6-6: This graph shows the phase diagram at fixed chemical potential $\mu_{\uparrow'} = \mu_{\downarrow'}$. The diagram is divided in the space of interaction parameters c_2/c_0 and $c_{\uparrow\downarrow'}/c_0$, among the $\uparrow'$ state, the $\downarrow'$ state and the phase mixed state.

PHASE DIAGRAM: $\mu_{\downarrow'} \neq \mu_{\uparrow'}$

The phase diagrams when the chemical potentials are unequal are obtained similarly. We again equate any two of the three grand free energy values F_2, F_3 and F_4, and obtain the following phase boundaries:

$$c_2 = \frac{{\mu_{\downarrow'}}^2 - {\mu_{\uparrow'}}^2}{{\mu_{\uparrow'}}^2} c_0 \tag{6.35}$$

$$c_0 \mu_{\downarrow'} = (c_0 + c_2 + \frac{c'_{\uparrow\downarrow}}{2}) \mu_{\uparrow'} \tag{6.36}$$

$$(c_0 + c_2) \mu_{\uparrow'} = (c_0 + c_2 + \frac{c'_{\uparrow\downarrow}}{2}) \mu_{\downarrow'}. \tag{6.37}$$

Note that the last two boundaries also follow that the the numerators for the densities vanishes in Eq. 6.25*d*, i.e. one of the two spin states' density becomes zero, eliminating the phase mixed state. The above three boundary lines intersect at the point

$$c_2 = \frac{{\mu_{\downarrow'}}^2 - {\mu_{\uparrow'}}^2}{{\mu_{\uparrow'}}^2} c_0, \ \frac{c'_{\uparrow\downarrow}}{2} = \frac{\mu_{\downarrow'}\mu_{\uparrow'} - {\mu_{\downarrow'}}^2}{{\mu_{\uparrow'}}^2} c_0, \tag{6.38}$$

which always satisfy

$$c_0(c_0+c_2)=(c_0+c_2+\frac{c'_{\uparrow\downarrow}}{2})^2, \tag{6.39}$$

or $D=0$, suggesting the intersection is always on the phase boundary for the fixed particle number phase diagram. This can be explained by the following argument: the mixed phase at fixed particle numbers $N_{\downarrow'}$ and $N_{\uparrow'}$ (or fixed $N_\uparrow$ and $N_\downarrow$) can be regarded as having resulted from a system at fixed $\mu_{\uparrow'}$ and $\mu_{\downarrow'}$ with the chemical potentials adjusted to satisfy the fixed-number requirement. Starting from the mixed phase, as $c'_{\uparrow\downarrow}$ is adjusted upwards, $\mu_{\uparrow'}$ and $\mu_{\downarrow'}$ will adjust to maintain the imposed values of $N_{\downarrow'}$ and $N_{\uparrow'}$. However, beyond the boundary $D=0$, it is no longer possible for the chemical potentials to adjust to attain a stable mixed phase, and the system phase separates into uniform BEC $\uparrow'$ and BEC $\downarrow'$ to satisfy the fixed-number constraint.

The stable regimes for spin-$\uparrow'$ state, spin-$\downarrow'$ state and the phase mixed state can be determined simply by comparing with the equal chemical potential phase diagram Fig. $6-6$. Thus we have Fig. $6-7$, showing the combined phase diagram of fixed chemical potential (indicated by solid lines) and fixed particle number (indicated by colored regions) when $\mu_{\downarrow'}=0.4\mu_{\uparrow'}$, $0.6\mu_{\uparrow'}$, $0.8\mu_{\uparrow'}$, $1.0\mu_{\uparrow'}$ and $1.2\mu_{\uparrow'}$.

Based on the above discussion, we see the fixed particle number phase diagram and the fixed chemical potential diagram are indeed equivalent, meaning every point on one diagram has its counterpart on the other diagram. As the $\mu_{\downarrow'}/\mu_{\uparrow'}$ ratio is varied, the fixed chemical potential phase boundary lines sweep the entire PM region in the fixed particle number phase diagram.

Finally, we discuss the phase digram in the context of existing experiments, focusing on the current parameter regimes $c_0>0$, $c_2<0$, $c'_{\uparrow\downarrow}=2c_0\hat{\Omega}^2>0$. According to our phase diagrams, in this parameter range for the case of $\mu_{\uparrow'}=\mu_{\downarrow'}$, the mixed phase is never stable, and the system always exhibits the $\downarrow'$ phase. This

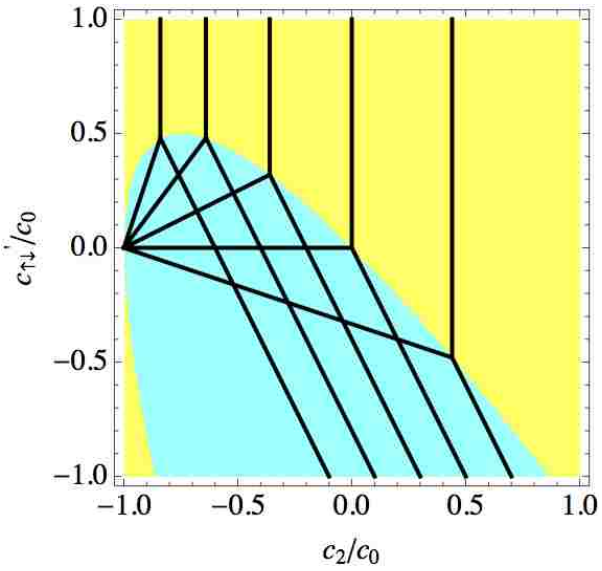

Figure 6-7: This phase diagram combines the diagrams for fixed density (phase regimes indicated by colors) and for fixed chemical potential (phase boundaries indicated by solid lines) at fixed chemical potentials $\mu_{\downarrow'} = 0.4\mu_{\uparrow'}, 0.6\mu_{\uparrow'}, 0.8\mu_{\uparrow'}, 1.0\mu_{\uparrow'}, 1.2\mu_{\uparrow'}$(from left to right). The yellow colored region represents the phase separated for fixed density, the cyan colored region indicates the phase mixed for fixed density. For each set of the boundary lines for fixed chemical potential that divides the c_2/c_0 - $c_{\uparrow\downarrow}'$ plane, the upper left is for the $\downarrow'$ phase, the upper right is for the $\uparrow'$ phase, while in the bottom region is the mixed-BEC. The intercepts of the phase boundaries for fixed chemical potential are located right at the phase boundary for fixed density.

can be traced to the fact that, as noted above, the interaction Hamiltonian is intrinsically ``imbalanced'', favoring the $\downarrow'$ state, indicating a nonzero chemical potential imbalance $\delta < 0$, or $\mu_{\downarrow'} < \mu_{\uparrow'}$ is needed to attain the mixed phase.

The phase diagram for the experimental parameter range is replotted in Fig. 6 − 8, where the vertical axis is now showing $\hat{\Omega}^2$. The solid lines in Fig. 6-8 show the ground-state phase diagram in the fixed chemical potential ensemble, at $\mu_{\downarrow'}/\mu_{\uparrow'} = 0.73$, showing regimes of $\downarrow'$ superfluid (upper-left, green), $\uparrow'$ superfluid (upper right, blue) and mixed superfluid (bottom center, red) phases. Thus, for $c_2/c_0 < 0$

and sufficiently large in magnitude, the mixed phase is stable in a triangular region of the phase diagram, exhibiting continuous phase transitions, with increasing normalized light-atom coupling $\hat{\Omega}$, to the $\downarrow'$ superfluid (for large $|c_2|/c_0$, to the left in the phase diagram) and to the $\uparrow'$ superfluid (for small $|c_2|/c_0$, to the right in the phase diagram). The same structure of the phase diagram holds for any ratio $\mu_{\downarrow'}/\mu_{\uparrow'}$, with the three curves that separate the phases moving as a function of the chemical potential ratio $\mu_{\downarrow'}/\mu_{\uparrow'}$; the two sets of dashed lines in Fig. 6-8 indicate the locations of these boundaries for $\mu_{\downarrow'}/\mu_{\uparrow'} = 0.37$ and $\mu_{\downarrow'}/\mu_{\uparrow'} = 0.93$.

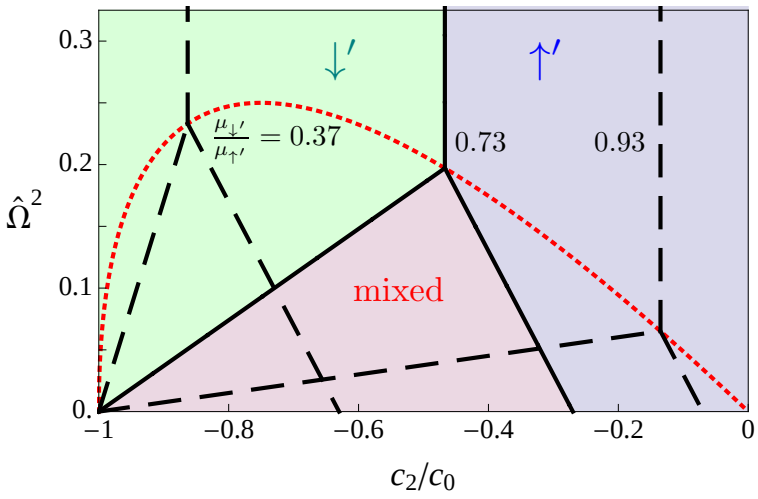

Figure 6-8: This diagram shows the phases for the experimentally relevant regime. The solid lines show the phase diagram, at fixed $\mu_{\downarrow'}/\mu_{\uparrow'} = 0.73$, separating regions of BEC $\downarrow'$ (upper left, green), BEC $\uparrow'$ (upper right, blue), and a mixed BEC of both species (lower triangle, red). The two sets of dashed lines show the phase diagram at two additional values of $\mu_{\downarrow'}/\mu_{\uparrow'}$, showing the evolution of the phase diagram at fixed chemical potential. For experiments at fixed particle number, the relevant phase boundary is the dotted line: Below this dotted line, the mixed BEC is stable, while above this dotted line the system will phase separate into regions of uniform $\uparrow'$ superfluid and uniform $\downarrow'$ superfluid.

Phase Diagram: Transition into the Unstable Region

Previous discussions are all based on the assumption that both $\mu_{\sigma'}$ are positive. But this is not absolutely necessary. Positive chemical potentials are indeed required for the case $\mu_{\uparrow'} = \mu_{\downarrow'}$ for fixed chemical potential, following from that the

densities can not be negative (Eq. 6.35). However, for unequal chemical potentials $\mu_{\uparrow'} \neq \mu_{\downarrow'}$, positive densities do not impose both chemical potentials to be positive (Eq. 6.25). One of the two chemical potentials can be allowed to have negative values. The phases boundaries are still determined by the vanishing of the densities. We obtain the boundaries as

$$(c_0 + c_2)\mu_{\uparrow'} = (c_0 + c_2 + \frac{c'_{\uparrow\downarrow}}{2})\mu_{\downarrow'} \tag{6.40}$$

$$c_0\mu_{\downarrow'} = (c_0 + c_2 + \frac{c'_{\uparrow\downarrow}}{2})\mu_{\uparrow'}. \tag{6.41}$$

To ensure the two sides of the above equations to have the same sign, we need $c_0 + c_2 + \frac{c'_{\uparrow\downarrow}}{2} < 0$.

These phase boundary lines, together with the phase boundary lines when both chemical potentials are positive, are shown in Fig. $6-9$. The two sets of phase boundary lines are divided by $c_0 + c_2 + \frac{c'_{\uparrow\downarrow}}{2} = 0$ (which is also the phase boundary line when the ratio $\mu_{\downarrow'}/\mu_{\uparrow'} = 0$), indicated by the red line. By allowing one chemical potential to be negative, the unstable regime becomes accessible to our approach.

6.3 Trapped Bosons with SOC

In the preceding section, we determined the phase diagram for a uniform boson gas with artificial light-induced SOC , showing how it can be used to obtain the boundary to the regime of phase separation both in the fixed density ensemble and in the fixed number ensemble. In the present section, we turn to the density distribution of the two boson species in a parabolic (harmonic) trap, making use of the fixed $\mu_{\uparrow'}$ and $\mu_{\downarrow'}$ results of Section 6.2.2.

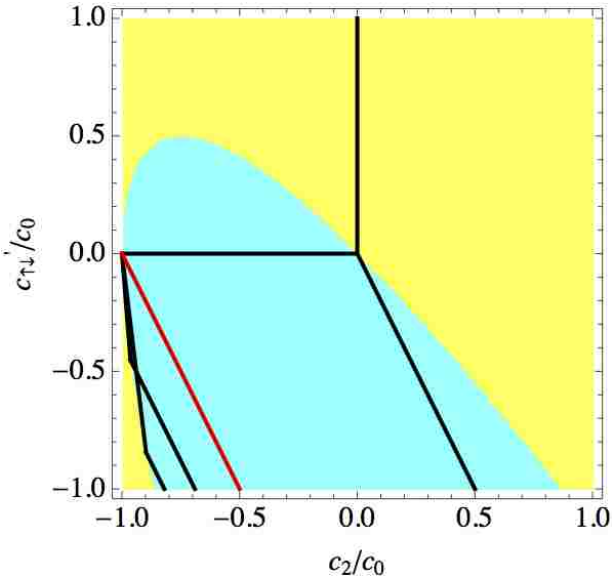

Figure 6-9: Phase boundaries for fixed chemical potentials when one chemical potential is negative, shown on the background of fixed density phase diagram. Above the red line ($c_0 + c_2 + \frac{c_{\uparrow\downarrow}'}{2} = 0$), the phase boundary lines are for the equal chemical potential case $\mu_{\downarrow'}/\mu_{\uparrow'} = 1$. For the phase boundary lines below the red line, one chemical potential is negative, the ratios are $\mu_{\downarrow'}/\mu_{\uparrow'} = -0.19, -0.32$.

6.3.1 Model with Local Density Approximation

We consider an anisotropic trapping geometry,

$$V_{\text{trap}}(\mathbf{r}) = \frac{1}{2}m(\Omega_z{}^2 z^2 + \Omega_s{}^2 s^2), \tag{6.42}$$

where $s^2 = x^2 + y^2$. Below, we'll make the choice $\Omega_z > \Omega_s$ for the trapping frequencies, such that an oblate ``pancake'' cloud shape is expected.

Our analysis of the density distributions in the presence of the trap uses the local density approximation (LDA). Within the LDA, the densities $|\psi_{\uparrow'}|^2$ and $|\psi_{\downarrow'}|^2$ are given by the uniform-case results Eq. 6.27 but with $\mu_{\sigma'} \to \mu_{\sigma'} - V_{\text{trap}}(\mathbf{r})$ (where now $\mu_{\sigma'}$ is the chemical potential at the trap center, $r = 0$). In the phase mixed state,

the densities can be written as:

$$|\psi_{\uparrow'}|^2 = \frac{\tilde{\mu}_{\uparrow'}}{\tilde{g}_{\uparrow'}} - \frac{1}{\tilde{g}_{\uparrow'}}(\frac{m}{2}{\Omega_z}^2 z^2 + \frac{m}{2}{\Omega_s}^2 s^2), \tag{6.43a}$$

$$|\psi_{\downarrow'}|^2 = \frac{\tilde{\mu}_{\downarrow'}}{\tilde{g}_{\downarrow'}} - \frac{1}{\tilde{g}_{\downarrow'}}(\frac{m}{2}{\Omega_z}^2 z^2 + \frac{m}{2}{\Omega_s}^2 s^2), \tag{6.43b}$$

where we defined effective interaction parameters $\tilde{g}_{\uparrow'} = -2D/c'_{\uparrow\downarrow}$ and $\tilde{g}_{\downarrow'} = -2D/(2c_2 + c'_{\uparrow\downarrow})$, with D defined in Eq. 6.28, and the effective chemical potentials

$$\tilde{\mu}_{\uparrow'} = \frac{(c_0 + c_2 + \frac{c'_{\uparrow\downarrow}}{2})\mu_{\downarrow'} - (c_0 + c_2)\mu_{\uparrow'}}{c_0\hat{\Omega}^2}, \tag{6.44a}$$

$$\tilde{\mu}_{\downarrow'} = \frac{(c_0 + c_2 + \frac{c'_{\uparrow\downarrow}}{2})\mu_{\uparrow'} - c_0\mu_{\downarrow'}}{c_2 + c_0\hat{\Omega}^2}, \tag{6.44b}$$

Similarly, for the phase separated states, after substitutions $\mu_{\sigma'} \to \mu_{\sigma'} - V_{\text{trap}}(\mathbf{r})$ we obtain densities

$$|\psi_{\uparrow'}|^2 = \frac{\mu_{\uparrow'} - V_{trap}}{c_0} = \frac{\mu_{\uparrow'}}{c_0} - \frac{1}{c_0}(\frac{m}{2}{\Omega_s}^2 s^2 + \frac{m}{2}{\Omega_z}^2 z^2), \tag{6.45a}$$

$$|\psi_{\downarrow'}|^2 = \frac{\mu_{\downarrow'} - V_{trap}}{c_0 + c_2} = \frac{\mu_{\downarrow'}}{c_0 + c_2} - \frac{1}{c_0 + c_2}(\frac{m}{2}{\Omega_s}^2 s^2 + \frac{m}{2}{\Omega_z}^2 z^2). \tag{6.45b}$$

An overall constraint is that the densities have to be positive at the spatial center $\mathbf{r} = 0$. This is already intrinsically satisfied in the above expressions. If the center is phase separated, from Eq. 6.45*a* and 6.45*b*, $\mu_{\downarrow'} \geq 0$ and $\mu_{\uparrow'} \geq 0$ ensure the central density to be positive. If the center is in the phase mixed state, the positive density requires $\frac{\tilde{\mu}_{\uparrow'}}{\tilde{g}_{\uparrow'}} > 0$ and $\frac{\tilde{\mu}_{\downarrow'}}{\tilde{g}_{\downarrow'}} > 0$, which are also satisfied through:

$$\frac{\tilde{\mu}_{\uparrow'}}{\tilde{g}_{\uparrow'}} = \frac{-(c_0 + c_2 + \frac{c'_{\uparrow\downarrow}}{2})\mu_{\downarrow'} + (c_0 + c_2)\mu_{\uparrow'}}{(c_0 + c_2)c_0 - (c_0 + c_2 + \frac{c'_{\uparrow\downarrow}}{2})^2} > 0, \tag{6.46}$$

$$\frac{\tilde{\mu}_{\downarrow'}}{\tilde{g}_{\downarrow'}} = \frac{c_0\mu_{\downarrow'} - (c_0 + c_2 + \frac{c'_{\uparrow\downarrow}}{2})\mu_{\uparrow'}}{(c_0 + c_2)c_0 - (c_0 + c_2 + \frac{c'_{\uparrow\downarrow}}{2})^2} > 0, \tag{6.47}$$

considering the aforementioned conditions for the phase mixed state. The ratios $\tilde{\mu}_\sigma/\tilde{g}_\sigma > 0$ for both $\uparrow'$ and $\downarrow'$ being positive guarantee the densities in Eq. 6.43 are positive, even the individual values of $\tilde{\mu}_{\sigma'}$ and $\tilde{g}_{\sigma'}$ may not be positive.

Given the values of c_2 and $c'_{\uparrow\downarrow}$ of a system, the system will fall in one of the following regions of the phase diagram, as divided by regimes of these interaction parameters:

1. Region I: $D > 0$, $c'_{\uparrow\downarrow}/c_0 > 0$. $\mu_{\uparrow'} > 0$, $\mu_{\downarrow'} > 0$, $\mu_{\uparrow'}/\mu_{\downarrow'} > 1$.
2. Region II: $D > 0$, $c_2 + \frac{c'_{\uparrow\downarrow}}{2} > 0$. $\mu_{\uparrow'} > 0$, $\mu_{\downarrow'} > 0$, $\mu_{\uparrow'}/\mu_{\downarrow'} < 1$.
3. Region III: $D > 0$, $c'_{\uparrow\downarrow}/c_0 < 0$, $c_2 + \frac{c'_{\uparrow\downarrow}}{2} < 0$, $c_0 + c_2 + \frac{c'_{\uparrow\downarrow}}{2} > 0$. $\mu_{\uparrow'} > 0$, $\mu_{\downarrow'} > 0$, $\mu_{\uparrow'}/\mu_{\downarrow'} < 1, = 1$ or > 1.
4. Region IV: $D < 0$. $\mu_{\uparrow'} = 0$ or $\mu_{\downarrow'} = 0$.
5. Region V: $D > 0$, $c_0 + c_2 + \frac{c'_{\uparrow\downarrow}}{2} < 0$. $\mu_{\uparrow'} < 0$ or $\mu_{\downarrow'} < 0$.

The regions are schematically indicated in the phase diagram in Fig. $6-10$. We are not including the unstable region that was discussed previously.

To solve for the density dependences, the procedure for each region is similar. Here we only discuss Region III and Region I.

6.3.2 Results

We present here our discussion about Region III and Region I, which exhibit contrasting spatial distributions. From the center going outward (i.e. with increasing radius), for Region III, both dressed spin states have decreasing density, just as expected in a Thomas-Fermi density profile. However, in Region I, one dressed spin state shows increasing density with increasing radius in the mixed BEC phase. Note that Region I is the regime that describes the physical properties of current experiments, which we will investigate in detail.

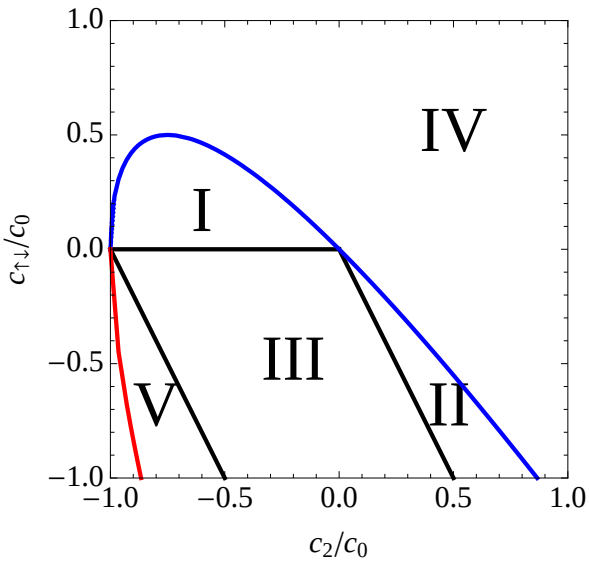

Figure 6-10: The five cases for a trapped BEC with SOC depending on the interaction parameters c_2/c_0 and $c'_{\uparrow\downarrow}$, marked on the fixed density phase diagram. Region I is the experimentally relevant case. Density distributions and phase makeups are different in each region.

Region III

In this region, the first conclusions that we can arrive at are: from $c'_{\uparrow\downarrow} < 0$, $\tilde{g}_{\uparrow'} > 0$. From $c_2 + c'_{\uparrow\downarrow}/2 < 0$, $\tilde{g}_{\downarrow'} > 0$. These ensure $\tilde{\mu}_{\uparrow'} > 0$ and $\tilde{\mu}_{\downarrow'} > 0$ due to Eqs. 6.46 and 6.47. Following from the signs of these parameters, both $\uparrow'$ and $\downarrow'$ bosons achieve maximum density in the center. For the phase mixed state, defining the characteristic radii

$$\begin{aligned} \tilde{R}_{z\uparrow'} &\equiv \sqrt{\frac{2\tilde{\mu}_{\uparrow'}}{m{\Omega_z}^2}},\ \tilde{R}_{s\uparrow'} \equiv \sqrt{\frac{2\tilde{\mu}_{\uparrow'}}{m{\Omega_s}^2}}, \\ \tilde{R}_{z\downarrow'} &\equiv \sqrt{\frac{2\tilde{\mu}_{\downarrow'}}{m{\Omega_z}^2}},\ \tilde{R}_{s\downarrow'} \equiv \sqrt{\frac{2\tilde{\mu}_{\downarrow'}}{m{\Omega_s}^2}}, \end{aligned} \tag{6.48}$$

then the densities Eq. 6.43 can be written as

$$|\psi_{\uparrow'}|^2 = \frac{\tilde{\mu}_{\uparrow'}}{\tilde{g}_{\uparrow'}}(1 - \frac{z^2}{\tilde{R}^2_{z\uparrow'}} - \frac{s^2}{\tilde{R}^2_{s\uparrow'}}), \tag{6.49a}$$

$$|\psi_{\downarrow'}|^2 = \frac{\tilde{\mu}_{\downarrow'}}{\tilde{g}_{\downarrow'}}(1 - \frac{z^2}{\tilde{R}^2_{z\downarrow'}} - \frac{s^2}{\tilde{R}^2_{s\downarrow'}}), \tag{6.49b}$$

in which bosons of each spin state exist in an ellipsoid with the elliptic radii given by the characteristic radii defined above. The radii of different spin states are generally not equal, thus the volume of the phase mixed state is defined by the space in which the $\uparrow'$ ellipsoid and the $\downarrow'$ ellipsoid overlap. Because $\tilde{R}_{z\downarrow'}/\tilde{R}_{s\downarrow'} = \tilde{R}_{z\uparrow'}/\tilde{R}_{s\uparrow'}$, the smaller volume is entirely encapsulated in the larger volume, meaning there is no partial overlapping. The clouds are schematically indicated in Fig. 6 – 11.

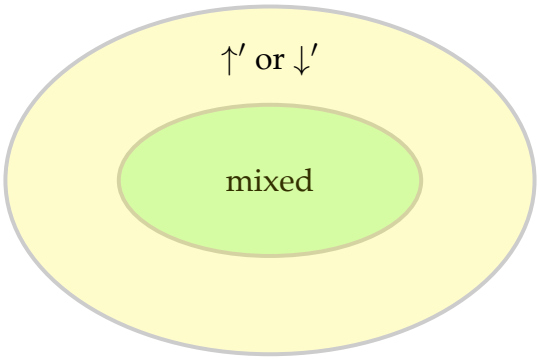

Figure 6-11: A schematic 2D projection showing the phases in the cloud in Region III ($D > 0, c'_{\uparrow\downarrow}/c_0 < 0, c_2 + \frac{c'_{\uparrow\downarrow}}{2} < 0, c_0 + c_2 + \frac{c'_{\uparrow\downarrow}}{2} > 0$). The inner volume is occupied by the mixed phase, and the outer shell is the $\uparrow'$ phase or $\downarrow'$ phase.

However, outside the phase mixed volume, only one spin state exist, and the above length scales using phase mixed density formulas are not valid. To correct this, we define similar length scales for the phase separated regime,

$$\begin{aligned} R_{z\uparrow'} &\equiv \sqrt{\frac{2\mu_{\uparrow'}}{m{\Omega_z}^2}}, \; R_{s\uparrow'} \equiv \sqrt{\frac{2\mu_{\uparrow'}}{m{\Omega_s}^2}}, \\ R_{z\downarrow'} &\equiv \sqrt{\frac{2\mu_{\downarrow'}}{m{\Omega_z}^2}}, \; R_{s\downarrow'} \equiv \sqrt{\frac{2\mu_{\downarrow'}}{m{\Omega_s}^2}}, \end{aligned} \tag{6.50}$$

utilizing the density formulas for the phase separated state Eq. 6.45, which now can be written as

$$|\psi_{\sigma'}|^2 = \frac{\mu_{\sigma'}}{c_{\sigma'}}(1 - \frac{z^2}{{R_{z\sigma'}}^2} - \frac{s^2}{{R_{s\sigma'}}^2}), \tag{6.51}$$

where $\sigma' = \uparrow', \downarrow'$, and $c_{\uparrow'} = c_0$, $c_{\downarrow'} = c_0 + c_2$. From the above analysis, we see the boson gas in the trap exhibits a shell structure, where the inner core is phase mixed, and the outer shell is phase separated. The volumes of the PM core and the PS shell are given by

$$\begin{aligned} \text{PM}: \ & 0 < |z| < R_{z0}, \ 0 < |s| < R_{s0}; \\ \text{PS}: \ & R_{z0} < |z| < R_{z1}, R_{s0} < |s| < R_{s1}, \end{aligned} \tag{6.52}$$

where $R_{z0} \equiv \min[\tilde{R}_{z\downarrow'}, \tilde{R}_{z\uparrow'}]$, $R_{s0} \equiv \min[\tilde{R}_{s\downarrow'}, \tilde{R}_{s\uparrow'}]$, and $R_{z1} \equiv R_{z\downarrow'}$ or $R_{z\uparrow'}$, $R_{s1} \equiv R_{s\downarrow'}$ or $R_{s\uparrow'}$, depending on which species occupies the outer shell.

Region I

In this region, $c'_{\uparrow\downarrow} = 2c_0\hat{\Omega}^2 > 0$, so $\tilde{g}_{\uparrow'} < 0$, while $\tilde{g}_{\downarrow'} > 0$. Since the ratio $\tilde{g}_{\downarrow'}/\tilde{\mu}_{\uparrow'}$ needs to be positive, we have $\tilde{\mu}_{\uparrow'} < 0$. This brings important implications for systems in this regime. The phase mixed state densities can be written as

$$|\psi_{\uparrow'}|^2 = \frac{\tilde{\mu}_{\uparrow'}}{\tilde{g}_{\uparrow'}}(1 + \frac{z^2}{\tilde{R}^2_{z\uparrow'}} + \frac{s^2}{\tilde{R}^2_{s\uparrow'}}), \tag{6.53a}$$

$$|\psi_{\downarrow'}|^2 = \frac{\tilde{\mu}_{\downarrow'}}{\tilde{g}_{\downarrow'}}(1 - \frac{z^2}{\tilde{R}^2_{z\downarrow'}} - \frac{s^2}{\tilde{R}^2_{s\downarrow'}}). \tag{6.53b}$$

The radii $\tilde{R}_{s\sigma}$ and $\tilde{R}_{z\sigma}$ which determine the spatial variation of the densities in the plane of the "pancake" shaped cloud and perpendicular to it, respectively, are given by

$$\tilde{R}_{z\uparrow'} = \sqrt{\frac{-2\tilde{\mu}_{\uparrow'}}{m{\Omega_z}^2}}, \ \tilde{R}_{s\uparrow'} = \sqrt{\frac{-2\tilde{\mu}_{\uparrow'}}{m{\Omega_s}^2}}, \tag{6.54}$$

$$\tilde{R}_{z\downarrow'} = \sqrt{\frac{2\tilde{\mu}_{\downarrow'}}{m{\Omega_z}^2}}, \ \tilde{R}_{s\downarrow'} = \sqrt{\frac{2\tilde{\mu}_{\downarrow'}}{m{\Omega_s}^2}}. \tag{6.55}$$

Although Eqs. 6.53 are similar to the usual LDA form for the density variation of a trapped BEC, one unusual feature stands out: While $|\psi_{\downarrow'}|^2$ decreases with increasing radius, the $\uparrow'$ density *increases* with increasing radius. Therefore the $\downarrow'$ always occupies a smaller volume than $\uparrow'$. The volume for the phase mixed V_{PM} is determined by the vanishing of $|\psi_{\downarrow'}|^2$. Beyond the volume, $|\psi_{\downarrow'}|^2 \to 0$, and the system is locally in a BEC of the spins-$\uparrow'$. The clouds are schematically represented by Fig. $6-12$.

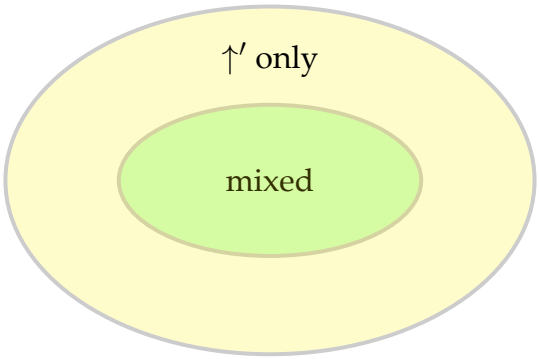

Figure 6-12: A schematic 2D projection graph showing the phases in the cloud in Region I ($D > 0$, $c'_{\uparrow\downarrow}/c_0 > 0$). The inner volume is occupied by the mixed phase, and the outer shell is always the $\uparrow'$ phase. This parameter region is experimentally relevant.

The characteristic radii for the phase separated outer shell are the same as defined in Eq. 6.50, and the shell structure of the boson gas is described by

$$\begin{aligned} \text{PM: } & |z| < \tilde{R}_{z\downarrow'}, |s| < \tilde{R}_{s\downarrow'} \\ \text{PS: } & \tilde{R}_{z\downarrow'} < |z| < R_{z\uparrow'}, \tilde{R}_{s\downarrow'} < |s| < R_{s\uparrow'} \end{aligned} \tag{6.56}$$

Now we make use of the above result about the shell structure of the boson gas of two spin states, and calculate the density profiles.

The actual boson densities $|\Psi_\uparrow|^2$ and $|\Psi_\downarrow|^2$ are related to the dressed state bosons $|\psi_{\uparrow'}|^2$ and $|\psi_{\downarrow'}|^2$ via

$$|\Psi_\uparrow(\mathbf{r})|^2 = |\psi_{\uparrow'}(\mathbf{r}) - \frac{1}{2}\hat{\Omega}e^{2ik_L x}\psi_{\downarrow'}(\mathbf{r})|^2, \tag{6.57}$$

$$|\Psi_\downarrow(\mathbf{r})|^2 = |\psi_{\downarrow'}(\mathbf{r}) - \frac{1}{2}\hat{\Omega}e^{-2ik_L x}\psi_{\uparrow'}(\mathbf{r})|^2, \tag{6.58}$$

which follow from Eq. I.18 in the limit of small $\hat{\Omega}$ and $\hat{\delta}$. In Eqs. 6.57 and 6.58, we take $\psi_{\uparrow'}(\mathbf{r})$ to be real and positive $\psi_{\downarrow'}(\mathbf{r})$. The relative phase between these condensates, yielding the minus signs in these expressions, follows by assuming the system will minimize the interaction energy density (and therefore $|\Psi_\uparrow(\mathbf{r})|^2$ and $|\Psi_\downarrow(\mathbf{r})|^2$) at the trap center.

Note that, since $\hat{\Omega} \ll 1$ to stabilize the mixed phase, the density of $n_\sigma(\mathbf{r})$ is approximately equal to the corresponding primed density plus an $\mathcal{O}(\hat{\Omega})$ term (the cross term upon expanding the modulus squared), leading to a $\cos 2k_L x$ spatial modulation (or, the stripe order [62]).

Therefore, the original boson numbers can be obtained from integrating over the total space, which includes the PM regime and the PS regime,

$$N_\uparrow = \int_{V_{PM}} dr^3\, |\psi_{\uparrow'}(\mathbf{r}) - \tfrac{1}{2}\hat{\Omega}e^{2ik_L x}\psi_{\downarrow'}(\mathbf{r})|^2 + \int_{V_{PS_{\uparrow'}}} dr^3\, \left|\psi_{\uparrow'}(\mathbf{r})\right|^2 \tag{6.59a}$$

$$N_\downarrow = \int_{V_{PM}} dr^3\, |\psi_{\downarrow'}(\mathbf{r}) - \tfrac{1}{2}\hat{\Omega}e^{-2ik_L x}\psi_{\uparrow'}(\mathbf{r})|^2 + \frac{\hat{\Omega}^2}{4}^2 \int_{V_{PS_{\uparrow'}}} dr^3\, \left|\psi_{\uparrow'}(\mathbf{r})\right|^2, \tag{6.59b}$$

in which

$$\int_{V_{PM}} dr^3\, \left|\psi_{\uparrow'}(\mathbf{r})\right|^2 = \frac{8\sqrt{2}\pi\tilde{\mu}_{\downarrow'}^{3/2}}{m^{3/2}} \frac{1}{{\Omega_s}^2\Omega_z}\left(\frac{\tilde{\mu}_{\uparrow'}}{3\tilde{g}_{\uparrow'}} - \frac{\tilde{\mu}_{\downarrow'}}{5\tilde{g}_{\uparrow'}}\right), \tag{6.60}$$

$$\int_{V_{PM}} dr^3\, \left|\psi_{\downarrow'}(\mathbf{r})\right|^2 = \frac{16\sqrt{2}\pi}{15} \frac{1}{{\Omega_s}^2\Omega_z} \frac{\tilde{\mu}_{\downarrow'}^{5/2}}{\tilde{g}_{\downarrow'} m^{3/2}}, \tag{6.61}$$

$$\int_{V_{PS_{\uparrow'}}} dr^3\, \left|\psi_{\uparrow'}(\mathbf{r})\right|^2 = \frac{16\sqrt{2}\pi}{15} \frac{{\mu_{\uparrow'}}^{5/2}}{c_0 m^{3/2}} \frac{1}{{\Omega_s}^2\Omega_z} - \frac{8\sqrt{2}\pi\tilde{\mu}_{\downarrow'}^{3/2}}{m^{3/2}} \frac{1}{{\Omega_s}^2\Omega_z}\left(\frac{\mu_{\uparrow'}}{3c_0} - \frac{\tilde{\mu}_{\downarrow'}}{5c_0}\right). \tag{6.62}$$

From Eq. 6.59 we can solve for $\mu_{\uparrow'}$ and $\mu_{\downarrow'}$, and insert the chemical potentials back into to Eq. 6.43 to obtain the density profiles of the two species.

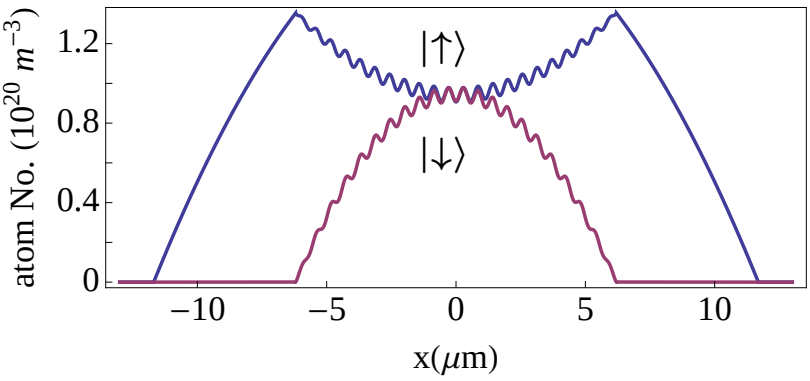

Figure 6-13: The plot shows the densities of spin-↑ atoms and spin-↓ atoms at $y = z = 0$ as a function of the spatial coordinate x. A central core of mixed BEC and an outer shell of $\uparrow'$ BEC are shown in the density profile. The ↑ atom density exhibits a non-monotonic trend in the mixed region, while the ↓ atom density decreases in the expected Thomas-Fermi dependence.

In Fig. 6-13 (1D), Fig. 6-14 and Fig .6-15 (2D), we show the calculated bosons densities $\left|\Psi_{\uparrow}\right|^2$ and $\left|\Psi_{\downarrow}\right|^2$. The unusual density dependence of ↑ bosons in the phase mixed central core is shown, together with the density decrease with increasing radius in the usual Thomas-Fermi fashion for the ↓ bosons in the phase mixed central core and ↑ bosons in the outer shell. The graph also exhibits a small oscillatory variation in the phase mixed region, expected as the 'stripe order'.

In Fig. 6-16 (1D) and Fig. 6-17 (2D), we plot the contrasting profiles of the total density $n_{\uparrow} + n_{\downarrow}$ and magnetization $n_{\uparrow} - n_{\downarrow}$. It is worth noting that tn the total density the stripes become more prominent from contribution of both species, while in the magnetization the oscillation is cancelled.

In these figures of density distribution, we chose parameters identical with those of Ref. [34]: Trapping frequencies $\Omega_s = 2\pi \times 50$ Hz, $\Omega_z = 2\pi \times 140$ Hz, interaction parameters $c_0 = h \times 7.79 \times 10^{-12}$ Hz cm^3, $c_2 = -h \times 3.61 \times 10^{-14}$ Hz cm^3, the wavevector $k_L = \sqrt{2}\pi/1000$nm, and we used the spin-orbit coupling parameter

$\hat{\Omega} = 0.15$. The chemical potentials $\mu_{\downarrow'} = 1469$Hz and $\mu_{\uparrow'} = 1472$Hz were chosen to achieve a total particle number $N = 180,000$ and reflect an effective Zeeman field $|\delta| = |\mu_{\uparrow'} - \mu_{\downarrow'}| = 3$Hz (values that are also consistent with Ref. [34]).

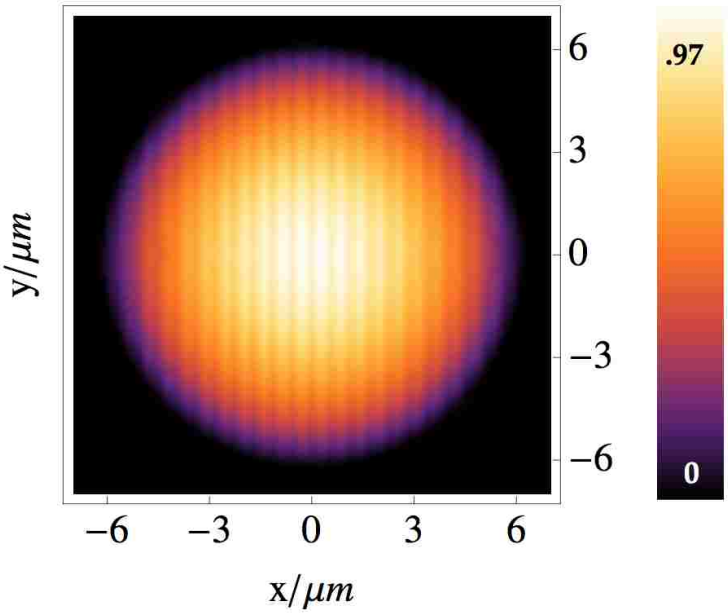

Figure 6-14: This plot shows a top view of the spin-↑ density at $z = 0$, showing this species is densest around the center of the cloud (the maximum is not exactly at the center due to the oscillation), and decreases to zero density at the edge. The density scale is atom number in 10^{20}m^{-3}.

Next we present a physical picture of the density profile results. In addition to the oscillatory spatial variation of the local densities of the two bosons species, the spin-↑ density is seen to exhibit a local maximum near the point where $|\Psi_{\downarrow}(\mathbf{r})|^2 \to 0$. As mentioned above, this is because Eq. 6.53a applies in the mixed phase, implying an increasing density of spins-↑ with increasing radius in the mixed region. The sequence of phases, within the LDA, in fact follows directly from the structure of the fixed-μ phase diagram. To see this, we note that, as seen in Fig. 6-8, the "triangle" of stable mixed phase moves to the left with decreasing $\mu_{\downarrow'}/\mu_{\downarrow'}$, with the $\downarrow'$ condensate always occuring to the left of this triangle and the $\uparrow'$ condensate always

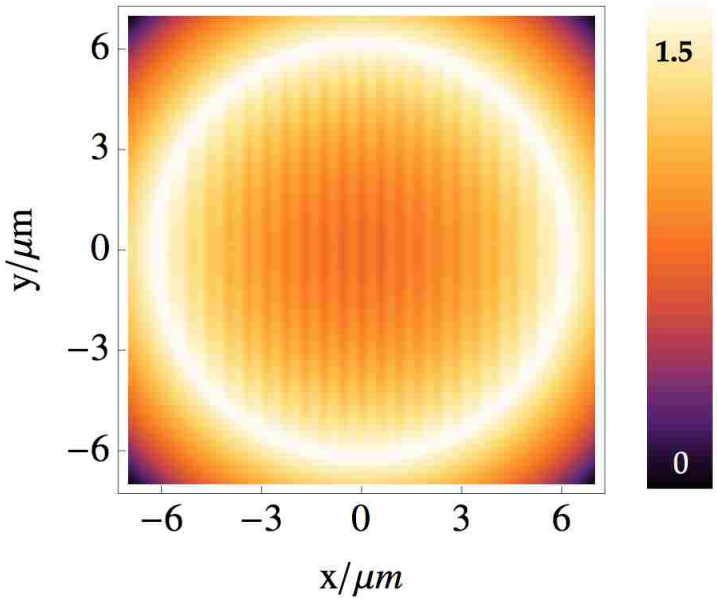

Figure 6-15: This plot shows a top view of the spin-↑ density at $z = 0$, showing the density reaches a local minimum at the center of the cloud, then increases to maximum before drops to zero at the edge. This non-monotonous spatial dependence can be an experimental signature for the mixed-BEC state in bosons with spin-orbit coupling. The density scale is atom number in $10^{20}\mathrm{m}^{-3}$.

occuring to the right. Within the LDA, then, the quantity to consider is the spatially-varying effective chemical potential ratio $\gamma(\mathbf{r}) \equiv [\mu_{\downarrow'} - V_{\mathrm{trap}}(\mathbf{r})]/[\mu_{\uparrow'} - V_{\mathrm{trap}}(\mathbf{r})]$, which decreases with increasing $\mathbf{r}$ (when $\mu_{\downarrow'} < \mu_{\uparrow'}$, which is required for stability of the mixed phase). If the mixed phase is stable in the center, then this implies that, at $\mathbf{r} = 0$, the system parameters must put it in the triangle of mixed BEC phase of Fig. 6-8. Increasing radius will decrease $\gamma(\mathbf{r})$, moving the triangle of mixed BEC phase to the left, leaving the system locally in the $\uparrow'$ phase at the edge. Another logical possibility, in which the $\downarrow'$ phase is stable in the center, followed by the mixed phase at intermediate radii, followed by the $\uparrow'$ phase at large radii, turns out to be difficult to achieve using experimentally-realistic parameters.

The outer shell of $\uparrow'$ condensate is described by the standard local density approximation for a single-species BEC, with $\left|\psi_{\uparrow'}(\mathbf{r})\right|^2 = (\mu_{\uparrow'} - V_{\mathrm{trap}}(\mathbf{r}))/c_0$. As we

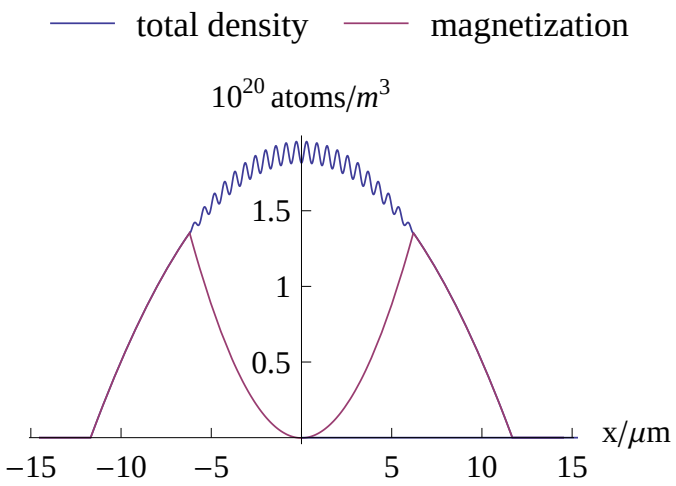

Figure 6-16: We show here a 1D plot of the total density $n_\uparrow + n_\downarrow$ and magnetization $n_\uparrow - n_\downarrow$ in the x direction, at $y = 0$, $z = 0$. The oscillation ("stripe" order) is enhanced in the total density by the two spin states, but is offset in the magnetization.

have already mentioned, the existence of the outer shell of $\uparrow'$ BEC is generally expected, since the mixed phase is stabilized by interactions. At large radii, where the atom densities are small, interactions can be neglected, and the system condenses into the lowest state, i.e., the left minimum of Fig. 6-1, which is the $\uparrow'$ phase. Therefore, we generally expect the outer shell of $\uparrow'$ condensate. With decreasing radius, coming in from the outside of the cloud, interaction effects eventually favor the population of the right minimum of Fig. 6-1, so that the system locally enters the mixed phase.

To understand the behavior of the densities in the central mixed BEC region, we transform the interaction Hamiltonian Eq. (6.10) to the basis of magnetization ($M = n_{\uparrow'} - n_{\downarrow'}$) and total density ($n = n_{\uparrow'} + n_{\downarrow'}$) :

$$\mathcal{H}_1 = \frac{1}{2}\int d^3r \Big[(c_0 + \frac{1}{2}c_0\hat{\Omega}^2 + \frac{3}{4}c_2)n^2(\mathbf{r}) - (\frac{1}{4}c_2 + \frac{1}{2}c_0\hat{\Omega}^2)M^2(\mathbf{r}) - \frac{1}{2}c_2 M(\mathbf{r})n(\mathbf{r}) \Big]. \tag{6.63}$$

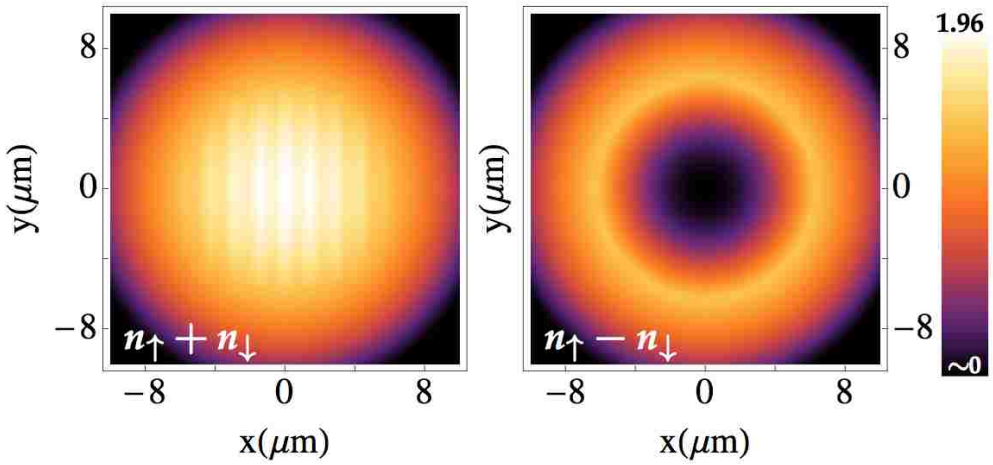

Figure 6-17: This plot shows a top view of the total density $n_\uparrow + n_\downarrow$ and magnetization $n_\uparrow - n_\downarrow$. The density scale is atom number in $10^{20}\mathrm{m}^{-3}$.

Recall that $c_0 \gg |c_2|$ and $\hat{\Omega}^2 \ll 1$. This implies that, in the first term, the overall density is controlled by $c_0 > 0$, so that $n(\mathbf{r})$ should exhibit the standard parabolic Thomas-Fermi profile in a trap. The magnetization $M(\mathbf{r})$, however, does not directly couple to the trap potential, but exhibits a spatial variation since the last term couples $M(\mathbf{r})$ and $n(\mathbf{r})$. Since $c_2 < 0$, this term favors having small (or negative) $M(\mathbf{r})$ in region of large $n(\mathbf{r})$ (i.e., at the trap center), leading to the central dip in the magnetization shown in the right lower panel of Fig. 6-13.

6.4 Sound Mode

In the preceding section, we showed that the mixed BEC phase of bosons with SOC exhibits an unusual density profile for the two species in a harmonic trapping potential. Now we turn to another signature of the mixed BEC phase, which is the Bogoliubov sound velocity, focusing on the case of a uniform condensate. We work in the experimental regime requiring $c_2 > 0$ and $c'_{\uparrow\downarrow} = 2c_0\hat{\Omega}^2 > 0$ in this section.

Using the effective Hamiltonian for the $\uparrow'$ and $\downarrow'$ states, consisting of Eq. 6.7 and Eq. 6.10), we have the time-dependent Gross-Pitaevskii equations (recall $\hbar = 1$):

$$\begin{aligned}(i\partial_t - \varepsilon(\mathbf{p}) + \mu_{\uparrow'})\psi_{\uparrow'} &= c_0|\psi_{\uparrow'}|^2\psi_{\uparrow'} + \bar{c}|\psi_{\downarrow'}|^2\psi_{\uparrow'} \\ (i\partial_t - \varepsilon(\mathbf{p}) + \mu_{\downarrow'})\psi_{\downarrow'} &= (c_0 + c_2)|\psi_{\downarrow'}|^2\psi_{\downarrow'} + \bar{c}|\psi_{\uparrow'}|^2\psi_{\downarrow'},\end{aligned} \tag{6.64}$$

where we defined $\bar{c} \equiv c_0(1 + \hat{\Omega}^2) + c_2$. Here, $\varepsilon(\mathbf{p})$ is the effective dispersion Eq. 6.8), and $\mathbf{p} = -i\boldsymbol{\nabla}$ is the momentum operator.

The next step is to consider small time-dependent fluctuations $\phi_\sigma(\mathbf{r}, t)$ around the equilibrium mixed phase solution, writing $\psi_\sigma(\mathbf{r}, t) = \psi_\sigma + \phi_\sigma(\mathbf{r}, t)$, where ψ_σ is the homogeneous mixed-phase solution satisfying Eq. 6.24, that we'll take to be real below. We can further express the fluctuation part as

$$\phi_\sigma = u_\sigma(\mathbf{r})e^{-i\omega t} + v_\sigma^*(\mathbf{r})e^{i\omega t}. \tag{6.65}$$

Plugging this into the time-dependent GP equations, keeping only linear terms in the fluctuations, and eliminating the chemical potentials using Eq. 6.24, we obtain

$$P \begin{pmatrix} u_{\uparrow'}(\mathbf{r}) \\ v_{\uparrow'}(\mathbf{r}) \\ u_{\downarrow'}(\mathbf{r}) \\ v_{\downarrow'}(\mathbf{r}) \end{pmatrix} = \omega \begin{pmatrix} u_{\uparrow'}(\mathbf{r}) \\ v_{\uparrow'}(\mathbf{r}) \\ u_{\downarrow'}(\mathbf{r}) \\ v_{\downarrow'}(\mathbf{r}) \end{pmatrix}, \tag{6.66}$$

where the matrix P

$$P = \begin{pmatrix} \varepsilon(\mathbf{p}) + c_0\psi_{\uparrow'}^2 & c_0\psi_{\uparrow'}^2 & \bar{c}\psi_{\uparrow'}\psi_{\downarrow'} & \bar{c}\psi_{\uparrow'}\psi_{\downarrow'} \\ -c_0\psi_{\uparrow'}^2 & -\varepsilon(\mathbf{p}) - c_0\psi_{\uparrow'}^2 & -\bar{c}\psi_{\uparrow'}\psi_{\downarrow'} & -\bar{c}\psi_{\uparrow'}\psi_{\downarrow'} \\ \bar{c}\psi_{\uparrow'}\psi_{\downarrow'} & \bar{c}\psi_{\uparrow'}\psi_{\downarrow'} & \varepsilon(\mathbf{p}) + (c_0+c_2)\psi_{\downarrow'}^2 & (c_0+c_2)\psi_{\downarrow'}^2 \\ -\bar{c}\psi_{\uparrow'}\psi_{\downarrow'} & -\bar{c}\psi_{\uparrow'}\psi_{\downarrow'} & -(c_0+c_2)\psi_{\downarrow'}^2 & -\varepsilon(\mathbf{p}) - (c_0+c_2)\psi_{\downarrow'}^2 \end{pmatrix}, \tag{6.67}$$

describing the collective Bogoliubov modes in the mixed BEC phase. The four eigenfrequencies $\omega(\mathbf{k})$ are straightforwardly found, after assuming plane wave solutions $u_\sigma(\mathbf{r}) = u_\sigma e^{i\mathbf{k}\cdot\mathbf{r}}$ and $v_\sigma(\mathbf{r}) = v_\sigma e^{i\mathbf{k}\cdot\mathbf{r}}$. They are $\pm\omega_\alpha$ with $\alpha = \pm$ and

$$\omega_\pm = \sqrt{\varepsilon(\mathbf{p})^2 + \varepsilon(\mathbf{p})(A \pm \sqrt{A^2 - 4Dn_{\uparrow'}n_{\downarrow'}})}, \tag{6.68}$$

where we defined

$$A = c_2 n_{\downarrow'} + c_0(n_{\uparrow'} + n_{\downarrow'}), \tag{6.69}$$

where D is the denominator defined in Eq. 6.28 that also determines the phase boundary at fixed densities, with stability of the mixed-BEC requiring $D > 0$.

Although both of $\omega_\pm(\mathbf{p})$ are linearly dispersing at low $\mathbf{p}$, representing Bogoliubov sound modes for BEC with spin-orbit coupling, we now focus on $\omega_-(\mathbf{p})$ which has interesting behavior as a function of the light-atom coupling. We first note that, due to the anisotropy of $\varepsilon(\mathbf{p})$, the corresponding sound velocity is smaller for modes propagating along the light-induced SOC direction (i.e. the $\hat{x}$ axis) than for modes propagating perpendicular to it. Explicitly, we find $v_x = v_\perp\sqrt{1-\hat{\Omega}^2}$, so that $v_x = v_\perp$ for $\hat{\Omega} = 0$ (in the limit of no light-atom coupling). To obtain $v_\perp$,

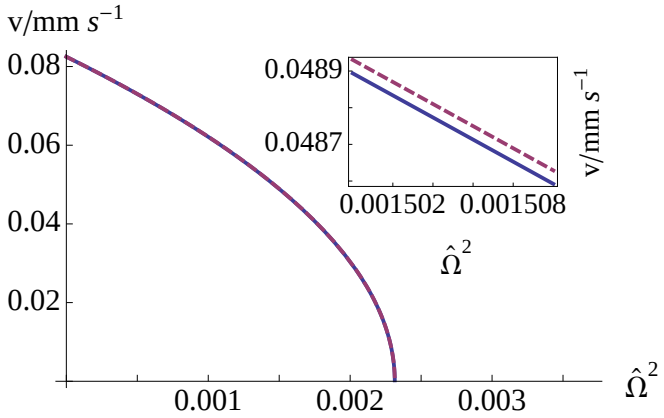

Figure 6-18: The main plot shows the Bogoliubov sound velocity in the mixed BEC phase, as a function of normalized light-atom coupling, which vanishes at the transition to the regime of phase separation. At this scale, it is not possible to discern the difference between v_x and $v_\perp$ (for sound modes along the SOC direction and perpendicular to it, respectively), although the inset, a zoom-in to these curves, shows the slight difference. In this inset, the dashed curve is $v_\perp$, and the solid curve is v_x.

we choose $\mathbf{p}$ along the $\hat{y}$ or $\hat{z}$ direction. Then, $v_\perp = \frac{d\omega_-}{dp}\,|_{p\to 0}$ with

$$v_\perp = \frac{1}{\sqrt{2m}}\sqrt{A - \sqrt{A^2 - 4Dn_{\uparrow'}n_{\downarrow'}}}. \tag{6.70}$$

For a spin-orbit coupled BEC in the mixed phase with fixed densities $n_{\uparrow'}$ and $n_{\downarrow'}$ (or fixed $n_\uparrow$ and $n_\downarrow$), Eq. 6.70 describes a collective superfluid sound mode. From the form of this equation, it is clear that $D > 0$ is required and that $v_\perp \to 0$ for $D \to 0$, with increasing light-atom coupling $\hat{\Omega}$, as the system approaches the regime of phase separation.

In Fig. 6-18, we illustrate this for the case of a mixed BEC state with $n_\uparrow = 0.6 \times 10^{20}/m^3$ and $n_\downarrow = 1.3 \times 10^{20}/m^3$ (with c_0 and c_2 the same as in the preceding section). Note that the smallness of c_2 for ^{87}Rb implies that the mixed BEC phase is only stable for very small values of $\hat{\Omega}$, further implying that, in practice, $v_\perp$ and v_x are nearly identical for realistic parameters. Thus, at this scale, the main plot could be either $v_\perp$ or v_x. Although the difference between these two velocities is

likely not observable, their vanishing as the phase boundary is approached would provide a distinct signature of the mixed-BEC phase.

6.5 Concluding Remarks

In this chapter, we have deployed the mean-field approximation to study a ^{87}Rb BEC with light-induced artificial SOC following the original setup of the Spielman group at NIST [34]. Although previous theoretical works often make simplifying assumptions when studying this system, such as focusing on the balanced case (i.e., Zeeman energy difference $\delta = 0$) or neglecting the spin-dependence of the interactions, we find that accounting for these effects leads to novel insight into the behavior of BEC's with artificial SOC.

In particular, we have analyzed the mean-field phase diagram as a function of δ (which is equivalent to a chemical potential difference for the two dressed states), the Raman coupling strength Ω, and interaction parameters. We argued that the evolution of this phase diagram as a function of chemical potentials implies (within the local density approximation) an unusual density dependence in a harmonic trap, with the dressed spin-$\uparrow$ ($m = 0$) bosons showing a density maximum with increasing radius, where the dressed spin-$\downarrow$ ($m = -1$) density vanishes. We also predict that the mixed-BEC phase of bosons with artificial SOC should exhibit a Bogolibov sound mode, the velocity of which vanishes as the regime of phase separation is approached.

CHAPTER 7
CONCLUSION

Ultracold atoms have provided physicists a remarkable new setting to observe new quantum many-body phenomena. Its high controllability makes more parameter ranges accessible and more Hamiltonians realistic. This thesis work is about the novel phases and unconventional properties of ultracold atomic many-body Bose-Einstein Condensate systems.

In previous chapters, we mainly studied the phase transitions and the density dependence in non-interacting and interacting BEC in an optical lattice (Chapters 2, 3 and 4), and for BEC with light-induced spin-orbit coupling (Chapters 5 and 6). For each topic, we introduced its background and related experiments, explained its theoretical model, applied the model to a few systems and tried to capture the physical implications through calculating physical observables that can be compared with or verified by experiments.

The first half of this thesis aims at developing a natural formalism for bosons in optical lattices, looking for physics beyond the tight-binding Bose Hubbard Model. We started from the single-particle states for atoms in a periodic potential by solving the Mathieu equation, and thereby developed an effective self-consistent theory describing interacting bosons based on Hartree Fock approximation. In these chapters, we examined the relationship between observables such as the transition temperature, condensate fraction and the density profile after time-of-flight free expansion, and parameters such as the optical lattice depth and the interaction strength.

In the second half of this thesis, we investigate the interesting physics brought by the artificial spin-orbit coupling implemented on interacting bosons, which creates a two-species interacting system that possesses a unique band structure. We studied the experimental setup by the Spielman group [34] in detail, concentrating on the mixed BEC phase formed by superposition of the two spin states. Our research on this miscible phase within mean-field approximation predicts an unusual density profile by implication of the phase diagrams that can be explained by the intrinsic imbalanced interaction of the two spin states. We also find the collective sound modes to be a signature of the mixed BEC phase that is worth probing experimentally.

Throughout our research, we strive to approach our problems in a very essential way. Our Mathieu equation formalism is directly based on the pristine Schröindger Equation, providing a method to to explore physics in regimes where the Hubbard model breaks down. Our study on bosons with light-induced spin-orbit coupling also starts from the band structure and the low-energy eigenstates, then builds up an effective theory to determine the stable states. As we try to extract the rich physics entailed from elegant theoretical models, we also make efforts at the same time to grasp current experiments. This course to address our research goals has been proved useful so far.

The thesis research is a small part of the ongoing effort of the atomic physics and condensed matter physics communities to understand the interplay between interaction, optical lattices and gauge fields. Bosons in optical lattices and bosons with strong interactions are fields that have been extensively studied. The competition between localization and de-localization for interacting bosons in optical lattices is a fruitful topic that has brought many insights for traditional condensed matter systems. However, as we have shown in this thesis, there still can be new

ways to describe the physical properties of such systems. Also, bosons with artificial gauge fields have attracted both experimental and theoretical attentions recently. Several kinds of synthetic gauge fields, including electric fields, magnetic fields and spin-orbit coupling have been proposed and/or realized. We anticipate a larger combination among interaction, optical lattices and gauge fields within various parameter regimes will bring more exotic phases and give rise to more intriguing behaviors of the system near phase transitions or critical points.

There are several possible extensions to our work. For example, it would be interesting to study bosons in optical lattices with gauge fields, as realized by the Ketterle Group [54] and the Bloch group [63] recently. Another possible addition is the response of the interacting bosons to a dynamical modulation of the optical lattices. It is also worth noting that spin-orbit coupling plays an important role in the transport mechanism of topological insulators, which is a peculiar state of matter that conducts at the surface while insulates in the bulk [39]. Although topological insulators have been realized in other materials, cold atoms is still a possible candidate and we hope our understanding of the light induced spin-orbit coupling will be proved helpful in finding the cold atom equivalent of topological insulators.

BIBLIOGRAPHY

[1] S. N. Bose, Z. Phys. **26**, 178 (1924).

[2] A. Einstein, Sitzber Kgl Preuss Akad Wiss, 261 (1924).

[3] A. Einstein, Sitzber Kgl Preuss Akad Wiss, 3 (1925).

[4] W. Ketterle, Rev. Mod. Phys. **74**, 1131 (2002).

[5] M. H. Anderson, J. R. Ensher, M. R. Matthews, C. E. Wieman, and E. A. Cornell, Science **269**, 198 (1995).

[6] C. C. Bradley, C. A. Sackett, J. J. Tollett, and R. G. Hulet, Phys. Rev. Lett. **75**, 1687,(1995).

[7] K. B. Davis, M.-O. Mewes, M. R. Andrews, N. J. van Druten, D. S. Durfee, D. M. Kurn, and W. Ketterle, Phys. Rev. Lett. **75**, 3969 (1995).

[8] http://patapsco.nist.gov/imagegallery/details.cfm?imageid=193, public use is allowed.

[9] M. Greiner, O. Mandel, T. Esslinger, T. W. Hänsch, and I. Bloch, Nature **415**, 39 (2002).

[10] I. B. Spielman, W. D. Phillips, and J. V. Porto, Phys. Rev. Lett. **98**, 080404 (2007).

[11] M. R. Andrews, C. G. Townsend, H.-J. Miesner, D. S. Durfee, D. M. Kurn, and W. Ketterle, Science **275**, 637 (1997).

[12] M. R. Matthews, B. P. Anderson, P. C. Haljan, D. S. Hall, C. E. Wieman, and E. A. Cornell, Phys. Rev. Lett. **83**, 2498 (1999).

[13] K. W. Madison, F. Chevy, W. Wohlleben, and J. Dalibard, Phys. Rev. Lett. **84**, 806 (2000).

[14] S. Levy, E. Lahoud, I. Shomroni, and J. Steinhauer, Nature **449**, 579-583 (2007).

[15] G. Roati, C. D. Errico, L. Fallani, M. Fattori, C. Fort, M. Zaccanti, G. Modugno, M. Modugno, and M. Inguscio, Nature **453**, 895 (2008).

[16] NIST Digital Library of Mathematical Functions, http://dlmf.nist.gov/ .

[17] I. Bloch, Nature Physics **1**, 23 (2005).

[18] I. Bloch, J. Dalibard, and W. Zwerger, Rev. Mod. Phys., **80**, 885 (2008).

[19] J. O. Andersen, Rev. Mod. Phys. **76**, 599 (2004).

[20] N. Gemelke, X. Zhang, C. Hung, and C. Chin, Nature, **460**, 995 (2009).

[21] F. Dalfovo, S. Giorgini, L.P. Pitaevskii, and S. Stringari, Rev. Mod. Phys., **71**, 463 (1999).

[22] M. P. A. Fisher, P. B. Weichman, G. Grinstein, and D. S. Fisher, Phys. Rev. B **40**, 546 (1989).

[23] H. Shi and A. Griffin, Physics Reports **304**, 1 (1998).

[24] M. Endres, M. Cheneau, T. Fukuhara, C. Weitenberg, P. Schauß, C. Gross, L. Mazza, M. C. Bañuls, L. Pollet, I. Bloch, and S. Kuhr, Science **334**, 200 (2011).

[25] X. Zhang, C.-L. Hung, S.-K. Tung, and C. Chin, Science **335**, 1070 (2012).

[26] S. Trotzky, L. Pollet, F. Gerbier, U. Schnorrberger, I. Bloch, N. V. Prokof'ev, B. Svistunov, and M. Troyer, Nature Physics **6**, 998 (2010).

[27] A. Elçi and E. Jones, Phys. Rev. B **34**, 8611 (1986).

[28] P. Grüter, D. Ceperley, and F. Laloë, Phys. Rev. Lett. **79**, 3549 (1997).

[29] M. J. Mark, E. Haller, K. Lauber, J. G. Danzl, A. J. Daley, and H.-C. Nägerl, Phys. Rev. Lett. **107**, 175301 (2011).

[30] H. Zhai, Int. J. Mod. Phys. B **26**, 1230001 (2012).

[31] Y.-J. Lin, R. L. Compton, A. R. Perry, W. D. Phillips, J. V. Porto, and I. B. Spielman, Phys. Rev. Lett. **102**, 130401 (2009).

[32] Y.-J. Lin, R. L. Compton, K. Jiménez-García , J. V. Porto, and I. B. Spielman, Nature **462**, 628 (2009).

[33] Y-J. Lin, R. L. Compton, K. Jiménez-García, W. D. Phillips, J.V. Porto, and I.B. Spielman, Nature Physics **7**, 531 (2011).

[34] Y.-J. Lin, K. Jiménez-García, and I. B. Spielman, Nature **471**, 83 (2011).

[35] T.-L. Ho and S. Zhang , Phys. Rev. Lett. **107**, 150403 (2011).

[36] J. Ruseckas, G. Juzeliunas, P. Öhberg, and M. Fleischhauer, Phys. Rev. Lett. **95**, 010404 (2005).

[37] T. Stanescu, C. Zhang, and V. Galitski, Phys. Rev. Lett. **99**, 110403 (2007).

[38] T. Stanescu, B. Anderson, and V. Galitski, Phys. Rev. A **78**, 023616 (2008).

[39] M. Z. Hasan and C. L. Kane, Rev. Mod. Phys., **82**, 3045 (2010).

[40] D. Xiao, N.-C. Chang, and Q. Niu, Rev. Mod. Phys. **82**, 1959 (2010).

[41] Y. K. Kato, R. C. Myers, A. C. Gossard, and D. D. Awschalom, Science **306**, 1910 (2004).

[42] M. König, S. Wiedmann, C. Brüne, A. Roth, H. Buhmann, L. W. Molenkamp, X.-L. Qi, and S.-C. Zhang, Science **318**, 766 (2007).

[43] X.-L. Qi and S.-C. Zhang, Rev. Mod. Phys. **83**, 1057 (2011).

[44] I. Žutić, J. Fabian, and S. Das Sarma, Rev. Mod. Phys. **76**, 323 (2004).

[45] J. D. Koralek, C. P. Weber, J. Orenstein, B. A. Bernevig, S.-C. Zhang, S. Mack, and D. D. Awschalom, Nature **458**, 610 (2009).

[46] C. Qu, C. Hamner, M. Gong, C. Zhang, and P. Engels, Phys. Rev. A **88**, 021604(R) (2013).

[47] L. J. LeBlanc, M. C. Beeler, K. Jiménez-García, A. R. Perry, S. Sugawa, R. A. Williams, and I. B. Spielman, New J. Phys. **15**, 073011 (2013).

[48] M. Aidelsburger, M. Atala, S. Nascimbène, S. Trotzky, Y.-A. Chen, and I. Bloch, Phys. Rev. Lett. **107**, 255301 (2011).

[49] J-Y Zhang, S.-C. Ji, Z. Chen, L. Zhang, Z.-D. Du, B. Yan, G.-S. Pan, B. Zhao, Y.-J. Deng, H. Zhai, S. Chen, and J.-W. Pan, Phys. Rev. Lett. **109**, 115301 (2012).

[50] Z. Fu, P. Wang, S. Chai, L. Huang, and J. Zhang, Phys. Rev. A **84**, 043609 (2011).

[51] L. J. LeBlanc, K. Jiménez-García, R. A. Williams, M. C. Beeler, A. R. Perry, W. D. Phillips, and I. B Spielman, Proc. Natl. Acad. Sci. USA **109**, 10811 (2012).

[52] P. Wang, Z.-Q. Yu, Z. Fu, J. Miao, L. Huang, S. Chai, H. Zhai, and J. Zhang, Phys. Rev. Lett. **109**, 095301 (2012).

[53] L. W. Cheuk, A. T. Sommer, Z. Hadzibabic, T. Yefsah, W. S. Bakr, and M. W. Zwierlein, Phys. Rev. Lett. **109**, 095302 (2012).

[54] H. Miyake, G. A. Siviloglou, C. J. Kennedy, W. C. Burton, W. Ketterle, Phys. Rev. Lett. **111**, 185302 (2013).

[55] S.-L. Zhu, H. Fu, C.-J. Wu, S.-C. Zhang, and L.-M. Duan, Phys. Rev. Lett. **97**, 240401 (2006).

[56] C. J. Kennedy, G. A. Siviloglou, H. Miyake, W. C. Burton, and W. Ketterle, Phys. Rev. Lett. **111**, 225301 (2013).

[57] G. Baym and C. Pethick, Phys. Rev. Lett. **76**, 6 (1996).

[58] G. Baym, J.-P. Blaizot, M. Holzmann, F. Laloë, and D. Vautherin, Phys. Rev. Lett. **83**, 1703 (1999).

[59] T.-L. Ho, Phys. Rev. Lett. **81**, 742 (1998).

[60] A. Widera, F. Gerbier, S. Fölling, T. Gericke, O. Mandel, and I. Bloch, New J. Phys. **8**, 152 (2006).

[61] Q.-Q. Lü and D. E. Sheehy, Phys. Rev. A **88**, 043645 (2013).

[62] C. Wang, C. Gao, C.-M. Jian, and H. Zhai, Phys. Rev. Lett. **105**, 160403 (2010).

[63] M. Aidelsburger, M. Atala, M. Lohse, J. T. Barreiro, B. Paredes, and I. Bloch, Phys. Rev. Lett. **111**, 185301 (2013).

[64] V. Mourik, K. Zuo, S. M. Frolov, S. R. Plissard, E. P. A. M. Bakkers, and L. P. Kouwenhoven, Science **336**, 1003 (2012).

[65] Z. F. Xu, R. Lü, and L. You, Phys. Rev. A **83**, 053602 (2011).

[66] T. Kawakami, T. Mizushima, and K. Machida, Phys. Rev. A **84**, 011607(R) (2011).

[67] C.-J. Wu, I. Mondragon-Shem, and X.-F. Zhou, Chin. Phys. Lett. **28**, 097102 (2011).

[68] H. Hu, B. Ramachandhran, H. Pu, and X.-J. Liu, Phys. Rev. Lett. **108**, 010402 (2012).

[69] S. Sinha, R. Nath, and L. Santos, Phys. Rev. Lett. **107**, 270401 (2011).

[70] J.-Y. Zhang, S.-C. Ji, L. Zhang, Z.-D. Du, W. Zheng, Y.-J. Deng, H. Zhai, S. Chen, and J.-W. Pan, Nature Physics **10**, 314 (2014).

[71] Y. Li, L.P. Pitaevskii, and S. Stringari, Phys. Rev. Lett. **108**, 225301 (2012).

[72] W. Zheng, Z.-Q. Yu, X. Cui, and H. Zhai, J. Phys. B **46**, 134007 (2013).

APPENDIX A
BOGOLIUBOV HAMILTONIAN

In this Appendix, we include the clipped details in Section. 2.3.2 in deriving the approximated Hamiltonian.

The grand canonical Hamiltonian is

$$\hat{K} = \int d^3r \Psi^\dagger(\mathbf{r})[-\frac{\hbar^2}{2m}\nabla^2 - \mu]\Psi(\mathbf{r}) + \frac{1}{2}\int d^3r \int d^3r' \, \Psi^\dagger(\mathbf{r})\Psi^\dagger(\mathbf{r}')v(\mathbf{r}-\mathbf{r}')\Psi(\mathbf{r}')\Psi(\mathbf{r}), \tag{A.1}$$

Use the Bogliubov prescription Equations 2.21 and 2.22, and the following deductions,

$$\frac{1}{V}\int d^3r \, a_0^\dagger(-\frac{\hbar^2}{2m}\nabla^2 - \mu)a_0 = -\mu N_0; \tag{A.2}$$

$$\frac{1}{\sqrt{V}}\int d^3r \, a_0^\dagger(-\frac{\hbar^2}{2m}\nabla^2 - \mu)\hat{\Psi}_1(\mathbf{r}) = \frac{1}{V}\int d^3r \, a_0^\dagger(-\frac{\hbar^2}{2m}\nabla^2 - \mu)\sum_{\mathbf{k}\neq 0}\hat{a}_\mathbf{k} e^{i\mathbf{k}\cdot\mathbf{r}} = 0; \tag{A.3}$$

$$\begin{aligned}
&\int d^3r \, \hat{\Psi}_1^\dagger(\mathbf{r})(-\frac{\hbar^2}{2m}\nabla^2 - \mu)\hat{\Psi}_1(\mathbf{r}) \\
=&\frac{1}{V}\sum_{\mathbf{k},\mathbf{k}'\neq 0}\int d^3r \, \hat{a}_\mathbf{k}^\dagger e^{-i\mathbf{k}\cdot\mathbf{r}}(-\frac{\hbar^2}{2m}\nabla^2 - \mu)\hat{a}_{\mathbf{k}'}e^{i\mathbf{k}'\cdot\mathbf{r}} \\
=&\sum_{\mathbf{k},\mathbf{k}'\neq 0}\delta_{\mathbf{k},\mathbf{k}'}(E_{\mathbf{k}'} - \mu)\hat{a}_\mathbf{k}^\dagger\hat{a}_{\mathbf{k}'} = \sum_{\mathbf{k}\neq 0}(E_\mathbf{k} - \mu)\hat{a}_\mathbf{k}^\dagger\hat{a}_\mathbf{k};
\end{aligned} \tag{A.4}$$

$$\begin{aligned}
&\frac{1}{2}\int d^3r \int d^3r' \, \frac{\hat{a}_0^\dagger}{\sqrt{V}}\frac{\hat{a}_0^\dagger}{\sqrt{V}}v(\mathbf{r}-\mathbf{r}')\frac{\hat{a}_0}{\sqrt{V}}\frac{\hat{a}_0}{\sqrt{V}} \\
=&\frac{1}{2}{n_0}^2 V\int d\mathbf{x}\sum_\mathbf{q} e^{-i\mathbf{q}\cdot\mathbf{x}}v(\mathbf{q}) \approx \frac{1}{2}{n_0}^2 V v(\mathbf{q}=0);
\end{aligned} \tag{A.5}$$

$$\frac{1}{2}\int d\mathbf{r}\int d\mathbf{r}'\frac{\hat{a}_0^\dagger}{\sqrt{V}}\frac{\hat{a}_0^\dagger}{\sqrt{V}}v(\mathbf{r}-\mathbf{r}')\frac{\hat{a}_0}{\sqrt{V}}\hat{\Psi}_1(\mathbf{r}) = 0; \tag{A.6}$$

$$
\begin{aligned}
&\frac{1}{2}\int d\mathbf{r}\int d\mathbf{r}'\frac{\hat{a}_0^\dagger}{\sqrt{V}}\frac{\hat{a}_0^\dagger}{\sqrt{V}}v(\mathbf{r}-\mathbf{r}')\hat{\Psi}_1(\mathbf{r}')\hat{\Psi}_1(\mathbf{r})\\
=&\frac{1}{2}\frac{\hat{a}_0^\dagger}{\sqrt{V}}\frac{\hat{a}_0^\dagger}{\sqrt{V}}\int d\mathbf{r}\int d\mathbf{r}'\sum_{\mathbf{q}}e^{-i\mathbf{q}\cdot(\mathbf{r}-\mathbf{r}')}v(\mathbf{q})\hat{\Psi}_1(\mathbf{r}')\hat{\Psi}_1(\mathbf{r})\\
=&\frac{1}{2}N_0\sum_{\mathbf{q}}v(\mathbf{q})\hat{\Psi}_1(\mathbf{q})\hat{\Psi}_1(-\mathbf{q})\\
=&\frac{1}{2}n_0\sum_{\mathbf{q}}v(\mathbf{q})\hat{a}_{\mathbf{q}}\hat{a}_{-\mathbf{q}};
\end{aligned}
\tag{A.7}
$$

$$
\begin{aligned}
&\frac{1}{2}\int d\mathbf{r}\int d\mathbf{r}'\hat{\Psi}_1^\dagger(\mathbf{r})\frac{\hat{a}_0^\dagger}{\sqrt{V}}v(\mathbf{r}-\mathbf{r}')\hat{\Psi}_1(\mathbf{r}')\frac{\hat{a}_0}{\sqrt{V}}+\frac{1}{2}\int d\mathbf{r}\int d\mathbf{r}'\frac{\hat{a}_0^\dagger}{\sqrt{V}}\hat{\Psi}_1^\dagger(\mathbf{r}')v(\mathbf{r}-\mathbf{r}')\frac{\hat{a}_0}{\sqrt{V}}\hat{\Psi}_1(\mathbf{r})\\
=&n_0\int d\mathbf{r}\int d\mathbf{r}'\hat{\Psi}_1^\dagger(\mathbf{r})v(\mathbf{r}-\mathbf{r}')\hat{\Psi}_1(\mathbf{r}')\\
=&N_0\sum_{\mathbf{q}}v(\mathbf{q})\hat{\Psi}_1^\dagger(\mathbf{q})\hat{\Psi}_1(\mathbf{q})\\
=&n_0\sum_{\mathbf{q}}v(\mathbf{q})\hat{a}_{\mathbf{q}}^\dagger\hat{a}_{\mathbf{q}};
\end{aligned}
\tag{A.8}
$$

$$
\begin{aligned}
&\frac{1}{2}\int d\mathbf{r}\int d\mathbf{r}'\hat{\Psi}_1^\dagger(\mathbf{r})\frac{\hat{a}_0^\dagger}{\sqrt{V}}v(\mathbf{r}-\mathbf{r}')\hat{\Psi}_1(\mathbf{r})\frac{\hat{a}_0}{\sqrt{V}}+\frac{1}{2}\int d\mathbf{r}\int d\mathbf{r}'\frac{\hat{a}_0^\dagger}{\sqrt{V}}\hat{\Psi}_1^\dagger(\mathbf{r}')v(\mathbf{r}-\mathbf{r}')\frac{\hat{a}_0}{\sqrt{V}}\hat{\Psi}_1(\mathbf{r}')\\
=&n_0\int d\mathbf{r}\int d\mathbf{r}'\hat{\Psi}_1^\dagger(\mathbf{r})v(\mathbf{r}-\mathbf{r}')\hat{\Psi}_1(\mathbf{r})\\
=&n_0\int d\mathbf{r}\int d\mathbf{r}'\sum_{\mathbf{k},\mathbf{k}'\neq 0}\sum_{\mathbf{q}}e^{-i\mathbf{k}\cdot\mathbf{r}}e^{(\mathbf{r}-\mathbf{r}')\cdot\mathbf{q}}e^{i\mathbf{k}'\cdot\mathbf{r}}\hat{a}_{\mathbf{k}}^\dagger v(\mathbf{q})\hat{a}_{\mathbf{k}'}\\
=&n_0\sum_{\mathbf{k},\mathbf{k}'\neq 0}\sum_{\mathbf{q}}\delta_{\mathbf{q},0}v(\mathbf{q})\delta_{\mathbf{k},\mathbf{q}+\mathbf{k}'}\hat{a}_{\mathbf{k}}^\dagger\hat{a}_{\mathbf{k}'}\\
=&n_0\sum_{\mathbf{k}\neq 0}v(\mathbf{0})\hat{a}_{\mathbf{k}}^\dagger\hat{a}_{\mathbf{k}},
\end{aligned}
\tag{A.9}
$$

we can obtain the final result of the grand canonical Hamiltonian $\hat{K}$:

$$
\hat{K}=-\mu N_0+\sum_{\mathbf{k}\neq 0}(E_{\mathbf{k}}-\mu)\hat{a}_{\mathbf{k}}^\dagger\hat{a}_{\mathbf{k}}+E_0+\sum_{j=1}^{7}\hat{V}_j=\hat{K}_0+\sum_{j=1}^{7}\hat{V}_j, \tag{A.10}
$$

where

$$E_0 = \frac{1}{2} {n_0}^2 V v(0); \tag{A.11}$$

$$\hat{V}_1 = \frac{1}{2} n_0 \sum_{\mathbf{q}} v(\mathbf{q}) \hat{a}_{\mathbf{q}} \hat{a}_{-\mathbf{q}}; \tag{A.12}$$

$$\hat{V}_2 = \frac{1}{2} n_0 \sum_{\mathbf{q}} v(\mathbf{q}) \hat{a}^\dagger_{\mathbf{q}} \hat{a}^\dagger_{-\mathbf{q}}; \tag{A.13}$$

$$\hat{V}_3 = n_0 \sum_{\mathbf{q}} v(\mathbf{q}) \hat{a}^\dagger_{\mathbf{q}} \hat{a}_{\mathbf{q}}; \tag{A.14}$$

$$\hat{V}_4 = n_0 \sum_{\mathbf{k} \neq 0} v(\mathbf{0}) \hat{a}^\dagger_{\mathbf{k}} \hat{a}_{\mathbf{k}}; \tag{A.15}$$

$$\hat{V}_5 = \frac{\sqrt{n_0}}{\sqrt{V}} \sum_{\mathbf{k} \neq 0, \mathbf{q}} v(\mathbf{q}) \hat{a}^\dagger_{\mathbf{k}+\mathbf{q}} \hat{a}_{\mathbf{k}} \hat{a}_{\mathbf{q}}; \tag{A.16}$$

$$\hat{V}_6 = \frac{\sqrt{n_0}}{\sqrt{V}} \sum_{\mathbf{k} \neq 0, \mathbf{q}} v(\mathbf{q}) \hat{a}^\dagger_{\mathbf{k}} \hat{a}^\dagger_{\mathbf{q}} \hat{a}_{\mathbf{k}+\mathbf{q}}; \tag{A.17}$$

$$\hat{V}_7 = \frac{1}{2V} \sum_{\mathbf{k}, \mathbf{k}' \neq 0, \mathbf{q}} v(\mathbf{q}) \hat{a}^\dagger_{\mathbf{k}+\mathbf{q}} \hat{a}^\dagger_{\mathbf{k}'-\mathbf{q}} \hat{a}_{\mathbf{k}'} \hat{a}_{\mathbf{k}}, \tag{A.18}$$

where the Fourier transformed interaction

$$v(\mathbf{q}) \equiv \int d\mathbf{x} e^{i\mathbf{q}\cdot\mathbf{x}} v(\mathbf{x}). \tag{A.19}$$

For an extreme case in which only exists excited particles, i.e. thermal gas, only $\hat{V}_7$ is left.

Normally, in the regime where the Bogoliubov Approximation applies, since the excited particles are few compared to the dominant majority of particles in the condensate, we can neglect $\hat{V}_5$,$\hat{V}_6$,$\hat{V}_7$.

APPENDIX B
GREEN'S FUNCTION

In this Appendix, we introduce the use of Green's function in a translationally invariant or discrete translationally invariant (e.g. lattice) interacting boson system.

The Green's function is defined as a function of spatial coordinates $\mathbf{r}$, $\mathbf{r}'$ and imaginary time τ, τ':

$$G(\mathbf{r},\tau;\mathbf{r}',\tau') = -\left\langle T_\tau \Phi(\mathbf{r},\tau)\Phi^\dagger(\mathbf{r}',\tau')\right\rangle, \tag{B.1}$$

where T_τ is the time ordering operator, meaning that the field operators following it are to be ordered in the way that their time arguments increase from right to left. By virtue of the translational invariance for imaginary time, we can set $\tau' = 0$:

$$G(\mathbf{r},\mathbf{r}';\tau,0) = -\left\langle T_\tau \Psi(\mathbf{r},\tau)\Psi^\dagger(\mathbf{r}',0)\right\rangle. \tag{B.2}$$

We begin by noting that the Dyson's Equation Eq. 2.30 can be transformed into the Matsubara space,

$$G(\mathbf{r},\mathbf{r}';i\Omega_m) = G_0(\mathbf{r},\mathbf{r}';i\Omega_m) + \int d^3r_1 d^3r_2\, G_0(\mathbf{r},\mathbf{r}_1;i\Omega_m)\Sigma(\mathbf{r}_1,\mathbf{r}_2;i\Omega_m)G(\mathbf{r}_2,\mathbf{r}';i\Omega_m). \tag{B.3}$$

Since the boson field operators can be expanded in orthonormal basis

$$\Psi(\mathbf{r},\tau) = \sum_{n\mathbf{k}} \psi_{n\mathbf{k}}(\mathbf{r}) b_{n\mathbf{k}}(\tau), \tag{B.4}$$

the Green's function becomes

$$G(\mathbf{r},\mathbf{r}';\tau,0) = -\sum_{nn'}\sum_{\mathbf{k}\mathbf{k}'}\psi_{n\mathbf{k}}(\mathbf{r})\psi^{*}_{n'\mathbf{k}'}(\mathbf{r}')\langle T_\tau b_{n\mathbf{k}}(\tau)b^{\dagger}_{n'\mathbf{k}'}(0)\rangle. \tag{B.5}$$

The Green's function after a replacement of $\mathbf{R}$, where $\mathbf{R}$ is any vector in a translationally invariant system or the periodic vector in a discrete translationally invariant system, is

$$G(\mathbf{r}+\mathbf{R},\mathbf{r}'+\mathbf{R};\tau,0) = -\sum_{nn'}\sum_{\mathbf{k}\mathbf{k}'}e^{i\mathbf{k}\cdot\mathbf{R}}\psi_{n\mathbf{k}}(\mathbf{r})e^{-i\mathbf{k}'\cdot\mathbf{R}}\psi^{*}_{n'\mathbf{k}'}(\mathbf{r}')\langle T_\tau b_{n\mathbf{k}}(\tau)b^{\dagger}_{n'\mathbf{k}'}(0)\rangle. \tag{B.6}$$

For such systems, we have

$$G(\mathbf{r}+\mathbf{R},\mathbf{r}'+\mathbf{R};\tau,0) = G(\mathbf{r},\mathbf{r}';\tau,0), \tag{B.7}$$

which means Eq. B.5 and Eq. B.6 should be equivalent. Therefore $\mathbf{k}=\mathbf{k}'$, which is also self-evident as momentum conservation. This condition forces the averaging bracket to contain a δ-function,

$$\langle T_\tau b_{n\mathbf{k}}(\tau)b^{\dagger}_{n',\mathbf{k}'}(0)\rangle \propto \delta(\mathbf{k},\mathbf{k}')G_{nn'}(\mathbf{k},\tau), \tag{B.8}$$

which tells us the Green's function B.5 is diagonal about $\mathbf{k}$. Expanding B.5 formally,

$$G(\mathbf{r},\mathbf{r}';\tau,0) = \sum_{nn'}\sum_{\mathbf{k}}\psi_{n\mathbf{k}}(\mathbf{r})\psi^{*}_{n'\mathbf{k}}(\mathbf{r}')G_{nn'}(\mathbf{k},\tau), \tag{B.9}$$

which can be, of course, transformed again into Matsubara space,

$$G(\mathbf{r},\mathbf{r}';i\Omega_m) = \sum_{nn'}\sum_{\mathbf{k}}\psi_{n\mathbf{k}}(\mathbf{r})\psi^{*}_{n'\mathbf{k}}(\mathbf{r}')G_{nn'}(\mathbf{k};i\Omega_m). \tag{B.10}$$

Assuming $G_0(\mathbf{r},\mathbf{r}';\tau,0)$,$\Sigma(\mathbf{r},\mathbf{r}';\tau,0)$ both have the same symmetry as in Eq. B.7, they should also be diagonal in $\mathbf{k}$. So in Matsubara space we have

$$G_0(\mathbf{r},\mathbf{r}';i\Omega_m) = \sum_{nn'}\sum_{\mathbf{k}} \psi_{n\mathbf{k}}(\mathbf{r})\psi^*_{n'\mathbf{k}}(\mathbf{r}')G_{0nn'}(\mathbf{k};i\Omega_m), \tag{B.11}$$

and

$$\Sigma(\mathbf{r},\mathbf{r}';i\Omega_m) = \sum_{nn'}\sum_{\mathbf{k}} \psi_{n\mathbf{k}}(\mathbf{r})\psi^*_{n'\mathbf{k}}(\mathbf{r}')\Sigma_{nn'}(\mathbf{k};i\Omega_m). \tag{B.12}$$

Plug in the above three equations into the Dyson Equation Eq. B.3, and use the following orthogonal relationship [27]

$$\int d\mathbf{r}\psi^*_{n\mathbf{k}}(\mathbf{r})\psi_{n'\mathbf{k}'}(\mathbf{r}) = \delta_{nn'}\delta(\mathbf{k},\mathbf{k}'), \tag{B.13}$$

we obtain

$$G_{nn'}(\mathbf{k};i\Omega_m) = G_{0nn'}(\mathbf{k};i\Omega_m) + \sum_{n_1n_2} G_{0nn_1}(\mathbf{k};i\Omega_m)\Sigma_{n_1n_2}(\mathbf{k};i\Omega_m)G_{n_2n'}(\mathbf{k};i\Omega_m), \tag{B.14}$$

which can be rewritten in matrix forms in n,n' space, with the second term naturally becoming matrix multiplication

$$\mathbf{G}(\mathbf{k};i\Omega_m) = \mathbf{G}_0(\mathbf{k};i\Omega_m) + \mathbf{G}_0(\mathbf{k};i\Omega_m)\mathbf{\Sigma}(\mathbf{k};i\Omega_m)\mathbf{G}(\mathbf{k};i\Omega_m), \tag{B.15}$$

or, more compactly,

$$\mathbf{G}(\mathbf{k};i\Omega_m) = \frac{1}{\mathbf{G}_0^{-1}(\mathbf{k};i\Omega_m) - \mathbf{\Sigma}(\mathbf{k};i\Omega_m)}. \tag{B.16}$$

If temperature is low, effects from higher bands can be neglected, we can make the single-band approximation focusing on the lowest band only,

$$\begin{aligned}&\mathbf{G}(\mathbf{k}; i\Omega_m) \approx G_{00}(\mathbf{k}; i\Omega_m) \\ =&\frac{1}{G_{0_{00}}^{-1}(\mathbf{k}; i\Omega_m) - \Sigma_{00}(\mathbf{k}; i\Omega_m)} = \frac{1}{i\Omega_m - \varepsilon_{0\mathbf{k}} - \Sigma_{00}(\mathbf{k}; i\Omega_m)},\end{aligned} \tag{B.17}$$

where the subscripts 00 refer to $n = n' = 0$.

APPENDIX C
BLOCH FUNCTION AND WANNIER FUNCTION

This appendix introduces two important complete bases: Bloch Function and Wannier Function.

C.1 Bloch Function

The Bloch states of single particle wavefunctions in a periodic system are:

$$\psi_{n\mathbf{k}}(\mathbf{r}) = e^{i\mathbf{k}\cdot\mathbf{r}} u_{n\mathbf{k}}(\mathbf{r}), \tag{C.1}$$

where n is the band index and $\mathbf{k}$ is the momentum within the first Brillouin Zone. $u_{n\mathbf{k}}(\mathbf{r})$ is periodic in $\mathbf{r}$. Therefore Bloch functions satisfy the following relationship:

$$\psi_{n\mathbf{k}}(\mathbf{r}+\mathbf{R}) = e^{i\mathbf{k}\cdot\mathbf{R}} \psi_{n\mathbf{k}}(\mathbf{r}), \tag{C.2}$$

where $\mathbf{R}$ is a lattice vector. Bloch functions can also be written in the following form

$$\psi_{n\mathbf{k}}(\mathbf{r}) = \sum_{\mathbf{G}} \phi_n(\mathbf{k}-\mathbf{G}) e^{i(\mathbf{k}-\mathbf{G})\cdot\mathbf{r}}, \tag{C.3}$$

where $\mathbf{G}$ is a reciprocal lattice vector, and $\phi_n(\mathbf{k})$ is the momentum Bloch function.

$\{\psi_{n\mathbf{k}}\}$ is a complete set, because of the following orthonormality relations [27]:

$$\sum_{n\mathbf{k}} \psi^*_{n\mathbf{k}}(\mathbf{r})\psi_{n\mathbf{k}}(\mathbf{r}') = \delta(\mathbf{r}-\mathbf{r}'); \tag{C.4}$$

$$\int d\mathbf{r}\ \psi^*_{n\mathbf{k}}(\mathbf{r})\psi_{n'\mathbf{k}'}(\mathbf{r}) = \delta_{nn'}\delta(\mathbf{k},\mathbf{k}'); \tag{C.5}$$

$$\sum_{n} \phi^*_{n}(\mathbf{k}-\mathbf{G})\phi_{n}(\mathbf{k}-\mathbf{G}') = \delta_{\mathbf{G}\mathbf{G}'}; \tag{C.6}$$

$$\sum_{n} \phi^*_{n}(\mathbf{k}-\mathbf{G})\phi_{n'}(\mathbf{k}-\mathbf{G}) = \delta_{nn'}, \tag{C.7}$$

where

$$\delta(\mathbf{k},\mathbf{k}') = \begin{cases} \delta_{\mathbf{k}\mathbf{k}'} \text{ if } \mathbf{k} \text{ discrete;} \\ \dfrac{(2\pi)^3}{V}\delta(\mathbf{k}-\mathbf{k}') \text{ if } \mathbf{k} \text{ continuous,} \end{cases} \tag{C.8}$$

where V is volume. So we can expand any function $\Phi(\mathbf{r})$ using Bloch functions:

$$\Phi(\mathbf{r}) = \frac{1}{\sqrt{V}}\sum_{n\mathbf{k}} c_{n\mathbf{k}}\psi_{n\mathbf{k}}(\mathbf{r}). \tag{C.9}$$

C.2 Wannier Function

Expand the Bloch function in Fourier Series, we come to Wannier functions

$$\psi_{n\mathbf{k}}(\mathbf{r}) = \sum_{\mathbf{R}} w_{n\mathbf{R}}(\mathbf{r})e^{i\mathbf{k}\cdot\mathbf{R}}, \tag{C.10}$$

so the Wannier functions can be expressed as

$$w_{n\mathbf{R}}(\mathbf{r}) = \frac{1}{v_k}\int_{v_k} d^3k\psi_{n\mathbf{k}}(\mathbf{r})e^{-i\mathbf{k}\cdot\mathbf{R}}, \tag{C.11}$$

v_k is the volume of one Brillouin zone,

$$v_k = \frac{(2\pi)^3}{v}. \tag{C.12}$$

Consider the periodicity of the Bloch function

$$\psi_{n\mathbf{k}}(\mathbf{r}+\mathbf{R}) = \psi_{n\mathbf{k}}(\mathbf{r})e^{i\mathbf{k}\cdot\mathbf{R}}, \tag{C.13}$$

We have

$$w_{n\mathbf{R}}(\mathbf{r}) = \frac{1}{v_k}\int_{v_k} d^3k\psi_{n\mathbf{k}}(\mathbf{r})e^{-i\mathbf{k}\cdot\mathbf{R}} = \frac{1}{v_k}\int_{v_k} d^3k\psi_{n\mathbf{k}}(\mathbf{r}-\mathbf{R}), \tag{C.14}$$

which is only dependent on $\mathbf{r}-\mathbf{R}$. Therefore we can rewrite the Wannier functions in a form that only depends on $\mathbf{r}$:

$$w_n(\mathbf{r}) \equiv w_{n\mathbf{R}}(\mathbf{r}+\mathbf{R}) = \frac{1}{v_k}\int_{v_k} d^3k\psi_{n\mathbf{k}}(\mathbf{r}). \tag{C.15}$$

And, $\psi_{n\mathbf{k}}(\mathbf{r})$, in return, can be written as

$$\psi_{n\mathbf{k}}(\mathbf{r}) = \sum_{\mathbf{R}} w_n(\mathbf{r}-\mathbf{R})e^{i\mathbf{k}\cdot\mathbf{R}}. \tag{C.16}$$

The orthonormal relationship of Wannier functions can be immediately derived from that of the Bloch functions,

$$\int d^3r w_n^*(\mathbf{r}-\mathbf{R})w_m(\mathbf{r}-\mathbf{R}') = \delta_{nm}\delta_{\mathbf{R}\mathbf{R}'}; \tag{C.17}$$

$$\sum_{\mathbf{R}n} w_n^*(\mathbf{r}'-\mathbf{R})w_n(\mathbf{r}-\mathbf{R}) = \delta(\mathbf{r}-\mathbf{r}'). \tag{C.18}$$

Then the Wannier functions can be used as the basis to expand any function

$$\Phi(\mathbf{r}) = \sum_{n\mathbf{R}} w_n(\mathbf{r}-\mathbf{R})b_n(\mathbf{R}). \tag{C.19}$$

Compare with Eq. C.9 and C.10, we get the relationship between $c_{n\mathbf{q}}$ and $b_n(\mathbf{R})$.

$$b_n(\mathbf{R}) = \frac{1}{\sqrt{V}} \sum_{\mathbf{q}} c_{n\mathbf{q}} e^{i\mathbf{q}\cdot\mathbf{R}}; \tag{C.20}$$

$$c_{n\mathbf{q}} = \frac{1}{\sqrt{V}} \sum_{\mathbf{R}} b_n(\mathbf{R}) e^{-i\mathbf{q}\cdot\mathbf{R}}. \tag{C.21}$$

Plug Eq. C.19 into the non-interacting Hamiltonian

$$H_0 = \int_V d^3r \sum_{n_1\mathbf{R}_1} \sum_{n_2\mathbf{R}_2} b^\dagger_{n_1}(\mathbf{R}_1) w^*_n(\mathbf{r}_1 - \mathbf{R}_1)(\hat{h} - \mu) b_{n_2}(\mathbf{R}_2) w_n(\mathbf{r}_2 - \mathbf{R}_2), \tag{C.22}$$

where $\hat{h}$ includes the kinetic term and external potentials. Now

$$\hat{h} w_n(\mathbf{r}_2 - \mathbf{R}_2) = \frac{1}{v_k} \int_{v_k} d^3k \epsilon_{n\mathbf{k}} \psi_{n\mathbf{k}}(\mathbf{r}_2 - \mathbf{R}_2) = \frac{1}{v_k} \int_{v_k} d^3k \epsilon_{n_2\mathbf{k}} \sum_{\mathbf{R}'} w_{n_2}(\mathbf{r}_2 - \mathbf{R}_2 - \mathbf{R}') e^{i\mathbf{k}\cdot\mathbf{R}'}, \tag{C.23}$$

where $\epsilon_{n\mathbf{k}}$ is the eigenvalue of Bloch function.

APPENDIX D
MATHIEU EQUATION

This Appendix introduces the mathematical details of the Mathieu Equation. The Mathieu Equation (Eq. 3.10) has the following solution:

$$y = C_1 \, \mathrm{ce}(a, q, u) + C_2 \, \mathrm{se}(a, q, u), \tag{D.1}$$

where C_1 and C_2 are constants, $\mathrm{ce}(a, q, u)$ is the Mathieu even function, which is even symmetric (analogous to cosine). $\mathrm{se}(a, q, u)$ is the Mathieu odd function (analogous to sine). Fig. $D-1$ shows the even Mathieu Function $\mathrm{ce}(a, q, u)$ when $a = 0.2$, $q = 0.5$. The shape of this function is high frequency oscillation enveloped in low frequency cosine-shaped bands. When $q = 0$, the function is reduced to a pure cosine wave, shown in Fig. $D-2$. The same can be said for the odd Mathieu function $\mathrm{se}(a = 0.2, q = 0.5, u)$ and $\mathrm{se}(a = 0.2, q = 0, u)$, as shown in Fig. $D-3$ and Fig. $D-4$.

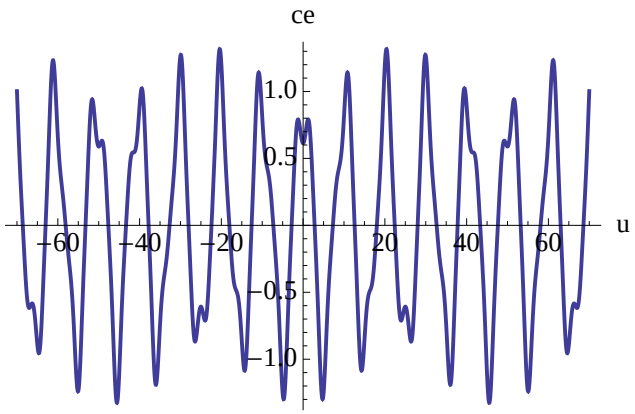

Figure D-1: The even Mathieu Function $\mathrm{ce}(a, q, u)$ when $a = 0.2$, $q = 0.5$.

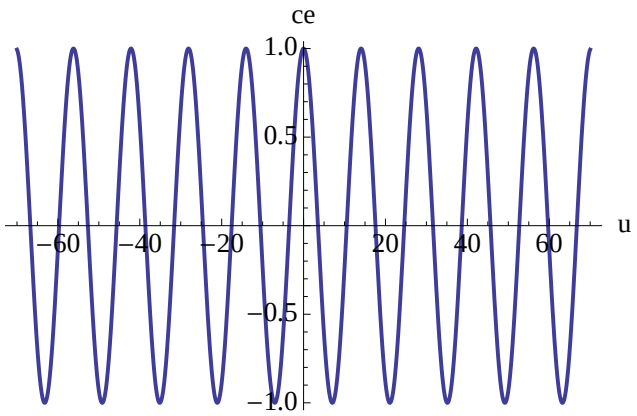

Figure D-2: The even Mathieu Function $\mathrm{ce}(a, q, u)$ becomes cosine function when $a = 0.2$, $q = 0$.

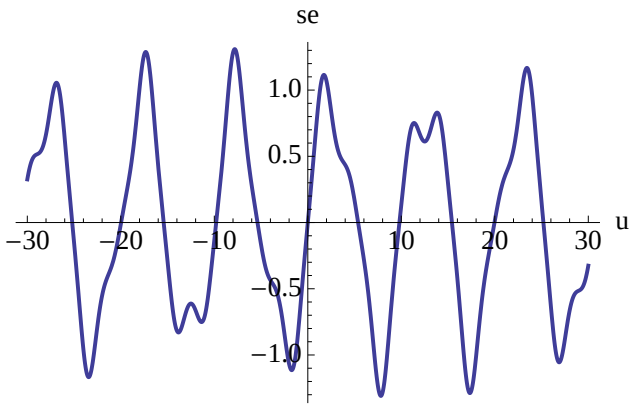

Figure D-3: The odd Mathieu Function $\mathrm{se}(a, q, u)$ when $a = 0.2$, $q = 0.5$.

Characteristic Functions

Mathieu functions are real when the parameter a is from Mathieu Characteristic Functions, which depend on ν (ν physically means quasi-momentum in the optical lattice problem) and q. Characteristic Functions for even Mathieu functions ce are denoted as $a_\nu(q)$, and Characteristic Functions for odd Mathieu functions se are denoted as $b_\nu(q)$.

Characteristic functions have discontinuity (or band gap in the physics language of dispersion) at integer ν values. Fig. $D-5$ shows the Characteristic Function $a_\nu(q)$ when $q = 1$, indicating that the function is even symmetric about ν. Fig. $D-6$ compares $a_\nu(q)$ when $q = 0, 0.5, 1$. The physical interpretation is that the

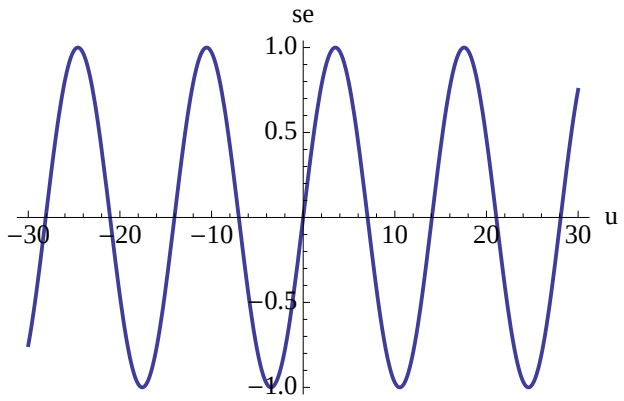

Figure D-4: The odd Mathieu Function $\mathrm{se}(a, q, u)$ becomes sine function when $a = 0.2$, $q = 0$.

ground state energy (at $\nu = 0$) is lowered as the optical lattice potential q becomes larger. This trend of the minima of $a_\nu(q)$ is explicitly described in Fig. $D-7$. In fact, $a_\nu(q)$ is also even symmetric about q, as shown in Fig. $D-8$ and Fig. $D-9$.

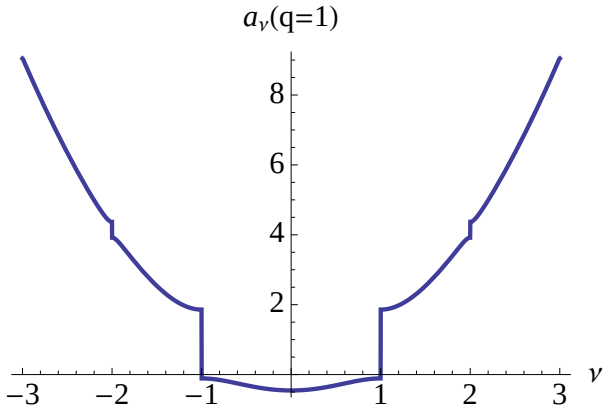

Figure D-5: Mathieu Characteristic Function $a_\nu(q)$ for the even Mathieu function when $q = 1$. The function has an even symmetry about ν. Here $q = V_0/4E_{re}$ indicates the lattice depth, ν is essentially the quasi-momentum, and $a(\nu, q)$ measures the energy. For particles in a periodic potential, this diagram represents energy bands in the extended-zone scheme.

Characteristic Functions $a_\nu(q)$ and $b_\nu(q)$ are equal except at integer ν's ($\nu = n$). Shown in Fig. $D-10$, at these discontinuous spots, $b_n(q)$ equals $a_n(q)$ at $q = 0$ and asymptotically approaches $a_{n-1}(q)$ at $q = \infty$. The former is because at $q = 0$ the Characteristic Function becomes a continuous parabola, and the latter is due to that

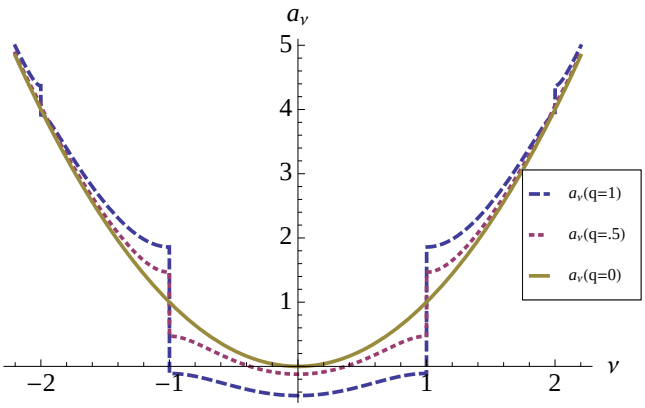

Figure D-6: Mathieu Characteristic Function $a_\nu(q)$ for the even Mathieu function when $q = 1, 0.5, 0$. The physical interpretation is that the ground state energy is lowered as the optical lattice potential q becomes larger. The Characteristic Function $a_\nu(q)$ is reduced to parabola when $q = 0$.

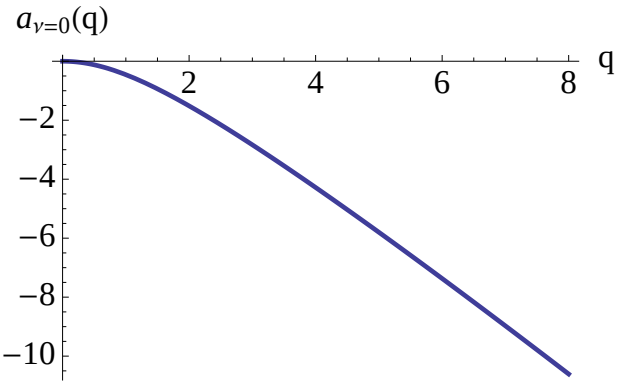

Figure D-7: The minima of the Mathieu Characteristic Function $a_\nu(q)$ are at $\nu = 0$. This graph shows its value at the minima as a function of q.

the bands are more and more flattened when q increases. If q can take negative values, $a_{2n}(q)$ and $a_{2n+1}(q)$, $b_{2n+1}(q)$ and $b_{2n+2}(q)$ are respective pairs that approach with each other at $q = -\infty$, due to the non-symmetry of $a_{2n+1}(q)$ and $b_{2n+1}(q)$. It is also worth noting that $b_\nu(q)$ is undefined at $\nu = 0$.

Besides these integer ν's, $a_\nu(q) = b_\nu(q)$ and the even symmetries of $a_\nu(q)$ applies to $b_\nu(q)$.

We observe that the parameter ν in Characteristic Functions is the number of periods in the Mathieu Functions in the interval $[0, 2\pi]$. In Fig. $D - 11$, the even Mathieu Functions $\mathrm{ce}(a, q = 1, u)$ are plotted as a function of u, where a's are from

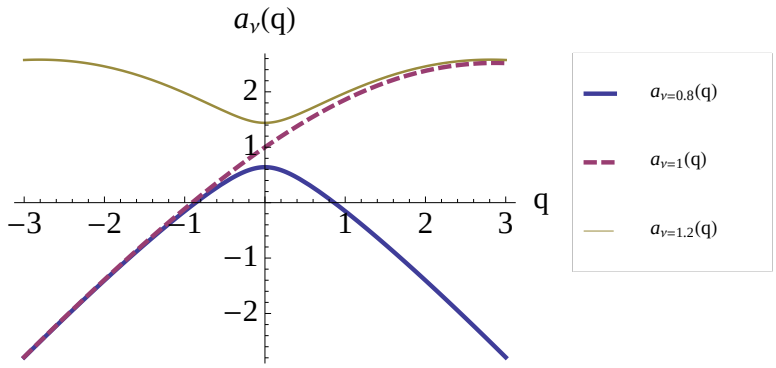

Figure D-8: The Mathieu Characteristic Function $a_\nu(q)$ when $\nu = 0.8, 1.2$, both of which are even symmetric about q. Note that the Characteristic Functions are discontinuous at integer ν, so the $\nu = 1$ curve shown here has asymptotic behavior at large optical lattice depth..

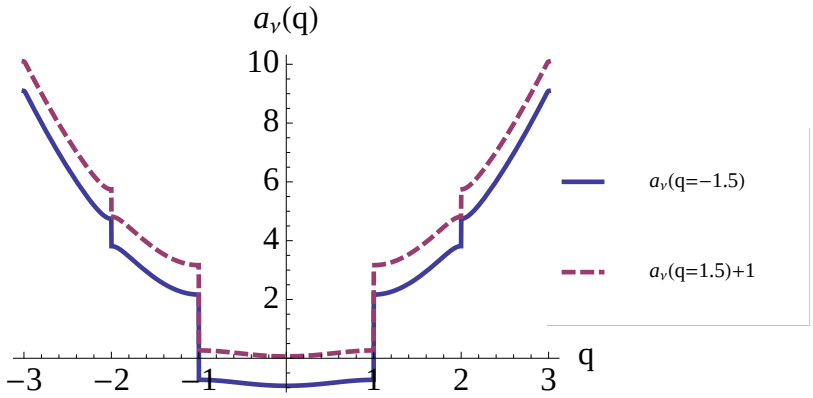

Figure D-9: The Mathieu Characteristic Functions $a_\nu(q)$ for $q = -1.5$ and $q = 1.5$ are identical. Here to visually differentiate the two curves we lift the former curve by 1 everywhere.

$a_{\nu=1.5}(q = 1)$ and $a_{\nu=2.5}(q = 1)$. One can see there are respectively 1.5 and 2.5 periods for these two curves between 0 and 2π.

When a is not from Characteristic Functions, Mathieu Functions are complex in value. Fig. $D - 12$ shows that Mathieu Functions are complex for a large part of the parametric space.

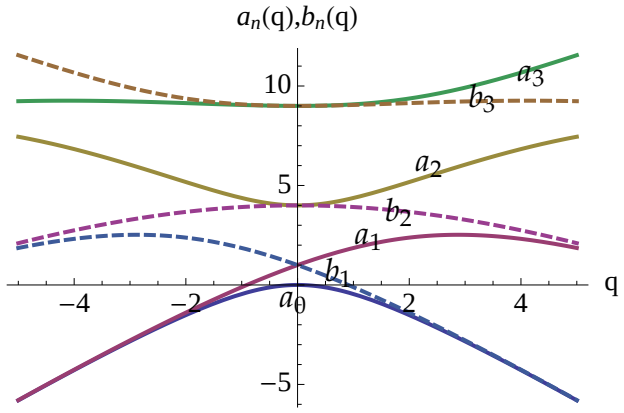

Figure D-10: The Characteristic Functions are discontinuous at integer ν's, the only spots when the even Characteristic Function $a_\nu(q)$ and the odd Characteristic Function $b_\nu(q)$ show differences. In fact, $b_n(q)$ equals $a_n(q)$ at $q = 0$, and asymptotically approaches $a_{n-1}(q)$ at $q = \infty$. Also shown here, when q takes negative values, a_{2n} and a_{2n+1}, b_{2n+1} and b_{2n+2} are asymptotic pairs at $q = -\infty$, due to the non-symmetry of a_{2n+1} and b_{2n+1}.

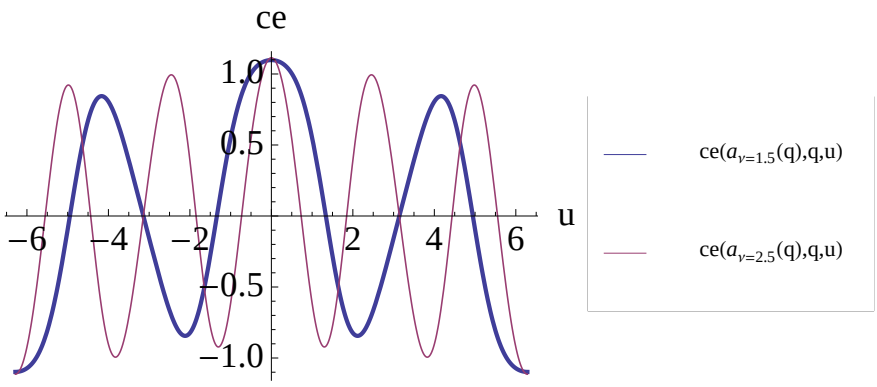

Figure D-11: The even Mathieu Functions $ce(a, q, u)$ as a function of u when a is from $a_{\nu=1.5}(q)$ and $a_{\nu=2.5}(q)$. One can see ν equals the number of periods in $[0, 2\pi]$ in $ce(a, q, u)$. Here $q = 1$.

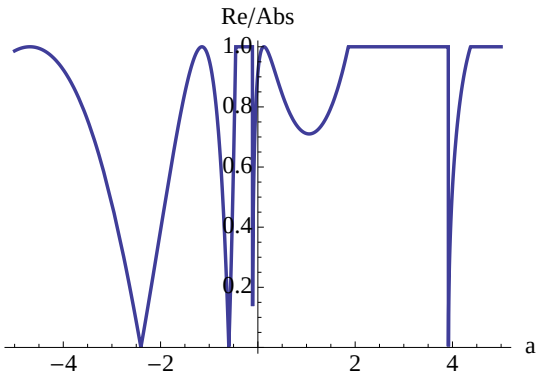

Figure D-12: Mathieu Functions can be complex valued in large ranges when a is not from Characteristic Functions. Here we plot the ratio of the real part of the even Mathieu function $\mathrm{ce}(a, q, u)$ to its modulus, as a function of continuous a. The curve take real values When the ratio hits 1.

APPENDIX E
BOUNDARY CONDITIONS AND FINITE SIZE EFFECT

Actual experiments take place in finite systems, before we step into calculations for such systems we need to choose proper boundary conditions. We discuss two kinds of boundary conditions here: vanishing boundary (hard wall) and periodic boundary. The former assumes a box shaped potential well with a flat bottom, while the latter is a theoretical model in which the boundary on one end is made to connect with the other end.

E.1 Vanishing Boundary Condition

For vanishing boundaries, the 1-D wavefunction is divided into even and odd states

$$\phi(\nu,q,x)=\begin{cases}\sqrt{\frac{2}{L}}\mathrm{ce}(a_\nu,q,k_{ol}x) & \nu=\frac{2n+1}{N_s};\\ \sqrt{\frac{2}{L}}\mathrm{se}(b_\nu,q,k_{ol}x) & \nu=\frac{2n}{N_s},\end{cases} \tag{E.1}$$

which makes analogue to the particle-in-a-box problem. Fig. $E-1$ shows the first four bands (when N_s is naively taken as 1 for simplicity), and they make perfect analog to particle-in-a-box wave functions.

The Fourier transform of the wavefunction is

$$\begin{aligned}\phi(\nu,q,k)&=\sqrt{\frac{2}{L}}\int_{-L/2}^{L/2}dx e^{ikx}\phi(\nu,q,x)\\ &=\begin{cases}\frac{2}{L}\int_{-L/2}^{L/2}dx\cos(kx)\mathrm{ce}(a_\nu,q,k_{ol}x) & \nu=\frac{2n}{N_s};\\ \frac{2}{L}\int_{-L/2}^{L/2}dx\sin(kx)\mathrm{se}(b_\nu,q,k_{ol}x) & \nu=\frac{2n+1}{N_s}.\end{cases}\end{aligned} \tag{E.2}$$

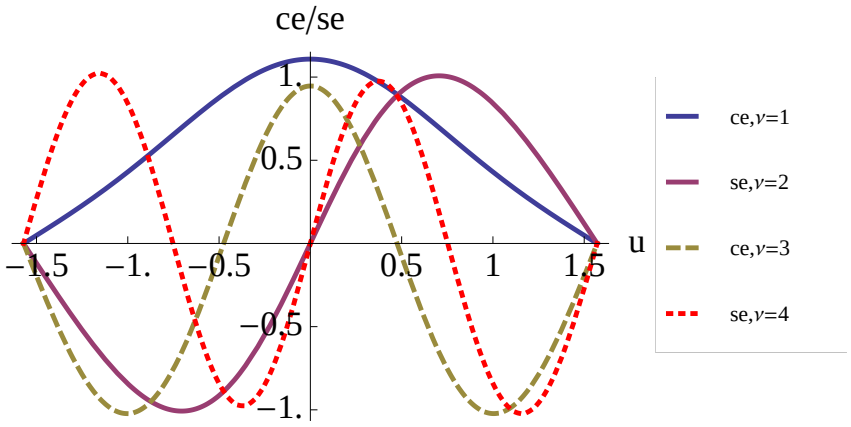

Figure E-1: The wave functions of bosons in a periodic potential can be solved from the Mathieu Equation. The eigenfunctions of the Mathieu Equation are the even ce states and the odd se states. In analogy to the particle-in-a-box problem, the nodes of the wave functions increase as the label of the state grows. ν is the quasi-momentum, $u = k_{ol}x$ is a dimensionless spacial variable. The first four Mathieu wave functions when $L = 2$ and $N_s = 1$ are shown here.

The wavefunctions in the real and momentum spaces are related by

$$\phi(\nu, q, x) = \sqrt{\frac{2}{L}} \sum_{k=m\pi/L} e^{ikx} \phi(\nu, q, k), \tag{E.3}$$

where m is an integer. The 3D Fourier transformed wavefunction

$$\Phi(\boldsymbol{\nu}, q, \mathbf{k}) = \phi(\nu_1, q, k_1)\phi(\nu_2, q, k_2)\phi(\nu_3, q, k_3), \tag{E.4}$$

where $\boldsymbol{\nu}$, $\mathbf{k}$ stand for vectors (ν_1, ν_2, ν_3) and (k_1, k_2, k_3), respectively.

E.2 Periodic Boundary Condition

For periodic boundary conditions, we define a complex Mathieu function, which makes analogue to Euler's formula.

$$\mathrm{me}(\nu, q, u) = \mathrm{ce}(a_\nu, q, u) + i\,\mathrm{sgn}(\nu)\mathrm{se}(b_\nu, q, u), \tag{E.5}$$

where ce and se are respectively even and odd Mathieu functions, a_ν and b_ν are their Characteristic Functions. The 1-d periodic boundary condition wave function is

$$\phi(n,q,x) = \begin{cases} \sqrt{\frac{1}{L}}\mathrm{me}(2n/N_s,q,k_{ol}x) & \text{if } n \neq 0; \\ \sqrt{\frac{2}{L}}\mathrm{ce}(a_0,q,k_{ol}x) & \text{if } n = 0. \end{cases} \tag{E.6}$$

This definition is explained as follows. When $n \neq 0$, from Bloch theorem

$$\mathrm{me}(\nu,q,u+2m\pi) = e^{2i\pi m\nu}\mathrm{me}(\nu,q,u), \tag{E.7}$$

where m is an integer. To satisfy $e^{2i\pi m\nu} = 1$, we need

$$\nu = n/m, \tag{E.8}$$

where n is also an integer. Now we require that the original box can be translationally repeated as the smallest period,

$$\mathrm{me}(\nu,q,u+N_s\pi) = \mathrm{me}(\nu,q,u), \tag{E.9}$$

this means the smallest m is

$$m = N_s/2, \tag{E.10}$$

then

$$\nu = 2n/N_s, \tag{E.11}$$

which proves the $n \neq 0$ wave function in Eq. E.6. Because now the wave function contains both real and imaginary parts, the normalizing factor is $\sqrt{1/L}$.

However, when $n = 0$, the odd Mathieu function $\mathrm{se}(b_\nu,q,u)$ is not defined in literature. It is natural to let $\mathrm{se}(b_0,q,u) = 0$. With only $\mathrm{ce}(a_0,q,u)$ in $\phi_0(x)$, the normalizing factor must be $\sqrt{\frac{2}{L}}$.

The reason to add a sign function to $\mathrm{se}(b_\nu, q, u)$ is to ensure its odd parity for both ν and u.

$$\mathrm{sgn}(\nu)\mathrm{se}(b_\nu, q, -u) = -\mathrm{sgn}(\nu)\mathrm{se}(b_\nu, q, u) = \mathrm{sgn}(-\nu)\mathrm{se}(b_{-\nu}, q, u), \tag{E.12}$$

meanwhile the even symmetry of $\mathrm{ce}(a_\nu, q, u)$ does not need modification.

We can expand the Mathieu functions in Fourier series ($n \neq 0$)

$$\mathrm{me}(2n/N_s, q, k_{ol}x) = \sum_{m=-\infty}^{\infty} c_{2m}^{2n/N_s}(q) e^{i(2n/N_s+2m)k_{ol}x}. \tag{E.13}$$

Fourier transform to obtain c_{2m}^{2n/N_s} coefficients,

$$c_{2m}^{2n/N_s}(q) = \frac{1}{L}\int_{-L/2}^{L/2} dx e^{-i(2n/N_s+2m)k_{ol}x}\mathrm{me}(2n/N_s, q, k_{ol}x). \tag{E.14}$$

When $n = 0$, the coefficient is just

$$c_{2m}^{0}(q) = \frac{\sqrt{2}}{L}\int_{-L/2}^{L/2} dx e^{-2imk_{ol}x}\mathrm{ce}(a_0, q, k_{ol}x). \tag{E.15}$$

The 3-d coefficient is

$$C[\mathbf{m}, \mathbf{n}, q] = c_{2m_1}^{2n_1/N_s}(q) c_{2m_2}^{2n_2/N_s}(q) c_{2m_3}^{2n_3/N_s}(q), \tag{E.16}$$

where $\mathbf{n}$ and $\mathbf{m}$ are 3-D vectors $\mathbf{n} = (n_1, n_2, n_3)$, $\mathbf{m} = (m_1, m_2, m_3)$. The Fourier transformed wavefunction is

$$\begin{aligned} &\Phi(\mathbf{n}, q, \mathbf{k}) \\ =&\frac{1}{V}\int d^3x e^{i\mathbf{k}\cdot\mathbf{x}} \sum_{\mathbf{m}} C[\mathbf{m}, \mathbf{n}, q] e^{i(2\mathbf{n}/N_s+2\mathbf{m})\mathbf{k}_{ol}\cdot\mathbf{x}} \\ =&\sum_{\mathbf{m}} C[\mathbf{m}, \mathbf{n}, q]\delta(2\frac{\mathbf{n}}{N_s} + 2\mathbf{m}, -\frac{\mathbf{k}}{k_{ol}}), \end{aligned} \tag{E.17}$$

where the wave vector $\mathbf{k} = (k_1, k_2, k_3)$. The following orthogonality relation is applied to obtain the Kronecker Delta function.

$$\frac{1}{L}\int_0^L dx e^{imx} e^{-inx} = \delta(m, n), \tag{E.18}$$

where m, n are integers. When $n = 0$, the ground state wavefunction can also be treated similarly

$$\Phi(\mathbf{0}, q, \mathbf{k}) = \sum_{\mathbf{m}} C[\mathbf{m}, 0, q]\delta(2\mathbf{m}, -\frac{\mathbf{k}}{k_{ol}}). \tag{E.19}$$

Now we have to deal with the finite size effect in the periodic boundary condition. By using Eq. E.18 it is assumed $k = sk_{ol}$ where s is an integer. This is not true in real experiments. If k is continuous, we generally don't get Kronecker delta, but a broadened smeared delta function.

$$\frac{1}{L}\int_{-L/2}^{L/2} dx e^{ix(k_1 + 2k_{ol}\frac{n_1}{N_s} + 2k_{ol}m_1)} = \frac{2}{L}\frac{\sin(\frac{L}{2}(k_1 + 2k_{ol}\frac{n_1}{N_s} + 2k_{ol}m_1))}{k_1 + 2k_{ol}\frac{n_1}{N_s} + 2k_{ol}m_1}. \tag{E.20}$$

This smeared delta gives a finite width to all the peaks in the density distribution. When $k_1 + 2k_{ol}\frac{n_1}{N_s} + 2k_{ol}m_1 = 0$ or $L \to 0$, the above factor becomes 1, giving a Kronecker delta. When $k_1 + 2k_{ol}\frac{n_1}{N_s} + 2k_{ol}m_1 \neq 0$, let $L \to \infty$, the factor becomes zero, eliminating width of any peaks. This shows the peaks have no width in a truly infinite system.

The 3-d smeared delta function is defined as

$$\begin{aligned}&\delta_V(\mathbf{k} + 2k_{ol}\frac{\mathbf{n}}{N_s} + 2k_{ol}\mathbf{m}) \\ &= \frac{8}{V}\prod_{i=x,y,z}\frac{\sin(L(k_i + 2k_{ol}\frac{n_i}{N_s} + 2k_{ol}m_i)/2)}{k_i + 2k_{ol}\frac{n_i}{N_s} + 2k_{ol}m_i}.\end{aligned} \tag{E.21}$$

APPENDIX F
PRECISION TEST

To do a numerical calculation, we need to set cutoffs for the upper and lower limits of the numerical integral in Eq. 3.19. The purpose of this Appendix is to verify that our numerical results are independent of this choice.

Ideally $\Lambda = \infty$ and $\epsilon = 0$, but it's unrealistic to numerically integrate to infinity and at $\nu_1 = \nu_2 = \nu_3 = 0$ singularity occurs. Therefore in actual calculation we need to use cutoffs. Also, the integral is on positive ν only, not on $[-\Lambda, \Lambda]$, since in both vanishing and periodic boundary conditions ν are ratios of positive integers.

In Eq. 3.19, the integral on the right hand side of the equation is a function of q and T_c, denoted as $I(q, T_c)$. Therefore for given q and f, we can solve for T_c numerically. Or we can assume critical temperatures T_c and see how the filling f changes.

Alternatively, Eq. 3.19 can be calculated in the spherical coordinate. Our calculation shows integrations using Cartesian coordinate and the spherical coordinate give the same result, as expected. One advantage of the spherical coordinate is that the singularity of the integrand at $\epsilon = 0$ can be avoided by the inclusion of the Jacobian of $d\nu^3$. But at the same time, it is less straightforward in the spherical coordinate to use integer values for Λ, which essentially is the Brillouin Zone we are integrating over. Due to the lacking of a clear physical picture, we still stick to Cartesian coordinate.

Physically, Λ indicates the number of bands in the dispersion that are included in the integral. Characteristic Functions increase with ν, so the contribution to $I(q, T_c)$ from large ν can be neglected. For a certain combination of f and T_c, We need to know what Λ is sufficient.

Another technical subtlety is choosing the lower cutoff for the integral to avoid singularity. The major contribution to the integral comes from when ν_i are small, therefore the lower limit ϵ should be carefully chosen to ensure adequate precision but not to consume undesirably long runtime.

In addition, allowing *Mathematica* to automatically set the number of recursions for numerical integrals would usually exceed reasonable time frame, we can only afford such luxury for a few individual calculations but not for across-the-board. So we have used `MaxRecursion` option in *Mathematica* to limit the number of recursions for iteration, which should also be tested.

To summarize, we have to check if the choice of these three parameters are sufficient to ensure precision: the upper cutoff Λ, the lower cutoff ϵ, and the number of recursion. We will run the same calculation for multiple times with one parameter of the three varying, and see if the result changes. For each case we test for both a deep lattice of high q, and a no lattice extreme of zero q. Note that since we don't have the real value as a reference, it is a precision test, we cannot do an *accuracy* test .

Testing Λ We first look at the upper cutoff Λ. As we include more bands (i.e. increase the upper cutoff), the integral approaches the total filling of the uncondensed cloud. We assume a temperature in the vicinity of the critical temperature, and observe how fast the integral I stablizes with inclusion of more bands. Fig. $F-1$ shows the filling as a function of Λ for $q = 0$, $\epsilon = 0.0001$, and the number of recursion is automatically set. One can see the curve goes into a platform after $\Lambda = 3$.

Similar plot for $q = 4$ is shown in Fig. $F-2$, where $\epsilon = 0.0001$, and the number of recursion is also automatically set. Note the small scale of the horizontal axis. The curve is stable from the beginning, indicating that for a system with deeper

Accuracy refers to how far the result is from the true value, while precision describes the range of results in multiple runs, i.e. how reproducible the result is.

lattice atoms tend to occupy over lower bands than a system with shallow lattice. Therefore, including the first 4 to 5 bands is probably more than enough for fillings that are not much larger than 1.

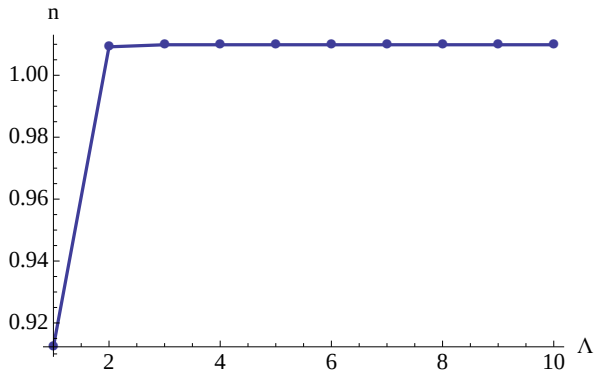

Figure F-1: In the numerical integral, the atom filling is stablized when the first 3 bands are included for $q = 0$, $\epsilon = 0.0001$, and the number of recursion is automatically set. The critical temperature $k_B T_c / E_{re} = 1.48$.

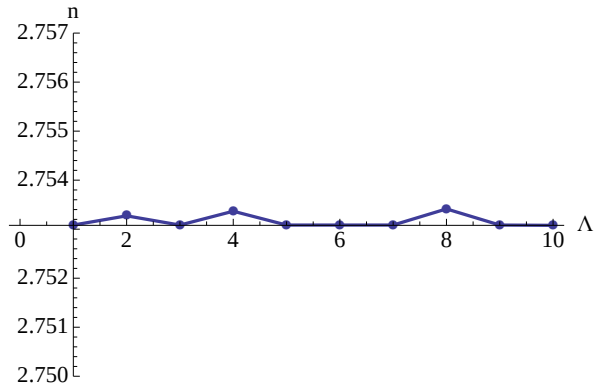

Figure F-2: In the numerical integral, the atom filling only fluctuates in very narrow range for $q = 4$, indicating atoms occupying only the lowest band. Here $\epsilon = 0.0001$, the number of recursion is automatically set. The critical temperature $k_B T_c / E_{re} = 33.7$.

Testing ϵ Next we test for an acceptable value of the lower cutoff ϵ, since integrating from 0 would bring singularity when the integral is done in Cartesian coordinate. The contribution from near the band bottom is the largest, so we need to carefully examine the effect of choosing finite ϵ.

We again assume a critical temperature, and look at the filling increasing with including more bands. This time, we plot the fillings calculated with different ϵ in the same graph, so that we can see how the integral converges to a certain limit when ϵ approaches 0.

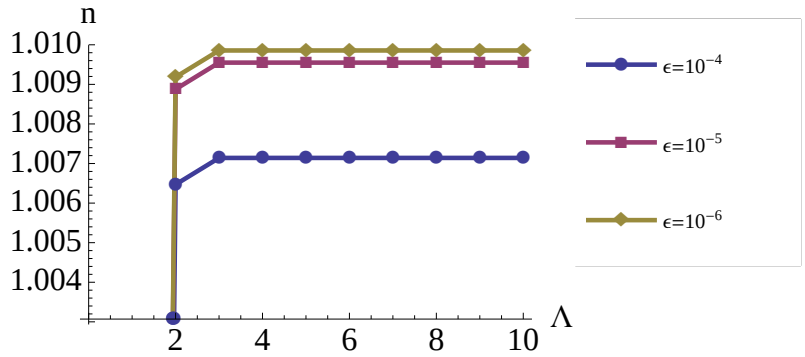

Figure F-3: The integrated value of the atom filling is larger when the lower cutoff ϵ takes a smaller value, but the increment falls under 1/1000 when ϵ goes down from 10^{-5} to 10^{-6}, showing a converging trend. Here the optical lattice depth $q = 0$. The number of recursion is automatically set. The critical temperature $k_B T_c / E_{re} = 1.48$.

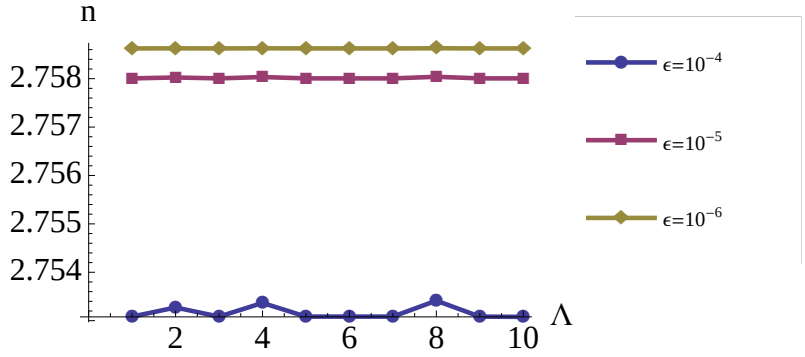

Figure F-4: The integrated value of the atom filling is larger when the lower cutoff ϵ takes a smaller value, but the increment falls under 1/1000 when ϵ goes down from 10^{-5} to 10^{-6}, showing a converging trend. Here the optical lattice depth $q = 4$. The number of recursion is automatically set. The critical temperature $k_B T_c / E_{re} = 33.7$.

Fig. $F-3$ shows at $q = 0$ the calculated filling is stablized within 1/1000 when ϵ goes below 10^{-5}. A similar trend for $q = 4$ is shown in Fig. $F-4$. From the point of numerical precision, this is enough.

Testing the number of recursion `MaxRecursion` is an artificially set parameter in *Mathematica*. The more recursions allowed in numerical integrals, the more accurate results they would yield. If the number of recursion is good enough, increasing it would not change the integral result.

We again assume a critical temperature that makes the calculated filling close to 1, and do the same integral for different `MaxRecursion`. Both Fig. $F-5$ and Fig. $F-5$ show a saturating trend when there are more than 2 recursions. To be on the safe side, we usually set `MaxRecursion` to be 4 or 5 in this project.

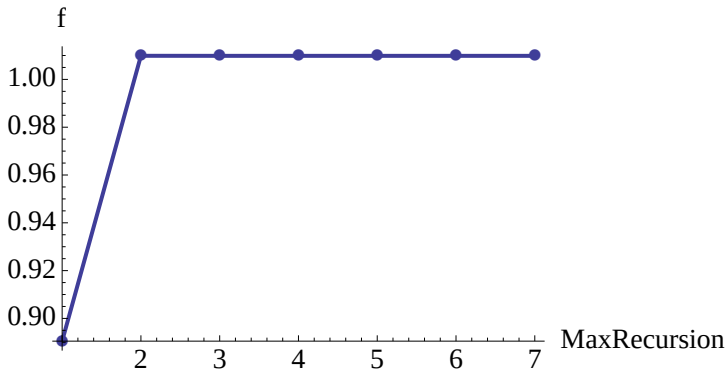

Figure F-5: This plot shows the calculated fillings at different number of recursions when the optical lattice depth $q = 0$. `MaxRecursion` is an artificially set parameter in *Mathematica*. When it is larger than 2, filling shows a saturating trend.

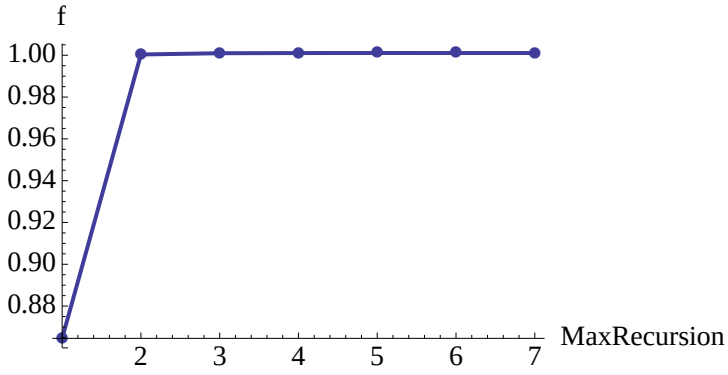

Figure F-6: This plot shows the calculated fillings at different number of recursions when the optical lattice depth $q = 4$. `MaxRecursion` is an artificially set parameter in *Mathematica*. When it is larger than 2, filling shows a saturating trend.

APPENDIX G
FREE EXPANSION

After the trapping potential is turned off, a Bose gas will undergo free expansion. Assume the potential is turned off at $t = 0$. The time dependent density

$$n(\mathbf{r}, t) = \mathrm{Tr}\rho_{\mathcal{H}}(t)\hat{n}(\mathbf{r}) = \mathrm{Tr}\rho_{\mathcal{H}}(t)\hat{\Phi}^{\dagger}(\mathbf{r})\hat{\Phi}(\mathbf{r}), \tag{G.1}$$

where the field operators $\Phi^{\dagger}(\mathbf{r})$ and $\Phi(\mathbf{r})$ obey the commutation rule

$$[\hat{\Phi}(\mathbf{r}), \hat{\Phi}^{\dagger}(\mathbf{r}')] = \delta(\mathbf{r} - \mathbf{r}'), \tag{G.2}$$

and $\rho_{\mathcal{H}}$ is the density matrix for the time dependent Hamiltonian

$$\mathcal{H}(t) = H + \Theta(-t)H_{trap}, \tag{G.3}$$

where

$$\Theta(t) = \begin{cases} 0, & (t \leq 0); \\ 1, & (t > 0). \end{cases} \tag{G.4}$$

We have

$$\partial_t \rho_{\mathcal{H}}(t) = -i[\mathcal{H}(t), \rho_{\mathcal{H}}(t)]. \tag{G.5}$$

Integration gives

$$\rho_{\mathcal{H}}(t) = \rho_{\mathcal{H}}(-\infty) - i\int_{-\infty}^{t} dt'[\mathcal{H}(t'), \rho_{\mathcal{H}}(t')]. \tag{G.6}$$

The Hamiltonian $\mathcal{H}$ is entirely time invariant during $t < 0$. Let $\mathcal{H}(t < 0) \equiv \mathcal{H}_\infty$ and $\rho_{\mathcal{H}}(t < 0) \equiv \rho_{\mathcal{H}_\infty}$. Then

$$[\mathcal{H}(t), \rho_{\mathcal{H}}(t)] = 0 \quad (t < 0). \tag{G.7}$$

For $t < 0$, the density is

$$n(t < 0) \equiv n_\infty = \mathrm{Tr}\rho_{\mathcal{H}_\infty}\hat{\Phi}^\dagger(\mathbf{r})\hat{\Phi}(\mathbf{r}). \tag{G.8}$$

For $t > 0$, to obtain the density, we first consider

$$\rho_{\mathcal{H}}(t) = \rho_{\mathcal{H}_\infty} - i\int_0^t dt'[\mathcal{H}(t'), \rho_{\mathcal{H}}(t')]. \tag{G.9}$$

Because

$$\begin{aligned}
\rho_{\mathcal{H}}(t) &= \sum_n \frac{t^n}{n!}\frac{\partial^n \rho_{\mathcal{H}}(t')}{\partial t'^n}|_{t'=0} \\
&= \rho_{\mathcal{H}}(0) + \sum_{n=1}^{\infty}\frac{t^n}{n!}(-i)[\mathcal{H}(t'), \frac{\partial^{n-1}\rho_{\mathcal{H}}(t')}{\partial t'^{n-1}}]|_{t'=0} \\
&= \rho_{\mathcal{H}_\infty} - it[H, \rho_{\mathcal{H}_\infty}] + (-i)^2\sum_{n=2}^{\infty}\frac{t^n}{n!}[\mathcal{H}(t'), [\mathcal{H}(t'), \frac{\partial^{n-2}\rho_{\mathcal{H}}(t')}{\partial t'^{n-2}}]]|_{t'=0} \\
&= \rho_{\mathcal{H}_\infty} - it[H, \rho_{\mathcal{H}_\infty}] + (-i)^2\frac{t^2}{2!}[H, [H, \rho_{\mathcal{H}_\infty}]] + (-i)^3\frac{t^3}{3!}[H, [H, [H, \rho_{\mathcal{H}_\infty}]]] + ...
\end{aligned} \tag{G.10}$$

According to Hadamard Lemma of Baker-Campbell-Hausdorff formula, the above summation is

$$\rho_{\mathcal{H}}(t) = e^{-itH}\rho_{\mathcal{H}_\infty}e^{itH}, \tag{G.11}$$

as expected. So for $t > 0$, let $\hat{n}(\mathbf{r}, t) \equiv e^{itH} n(\mathbf{r}) e^{-itH}$,

$$n(\mathbf{r}, t) = \mathrm{Tr}\, e^{-itH} \rho_{\mathcal{H}_\infty} e^{itH} \hat{\Phi}^\dagger(\mathbf{r}) \hat{\Phi}(\mathbf{r}) = \mathrm{Tr}\, e^{-itH} \rho_{\mathcal{H}_\infty} \hat{n}(\mathbf{r}, t) e^{itH} = \mathrm{Tr} \rho_{\mathcal{H}_\infty} \hat{n}(\mathbf{r}, t). \tag{G.12}$$

where the cyclic permutation $\mathrm{Tr}ABC = \mathrm{Tr}BCA$ is used. The above result is again as expected.

Now, for non-interacting bosons we rewrite H as H_0, therefore the Hamiltonian is $\mathcal{H}_\infty = H_0 + H_{trap}$ when $t < 0$, and H_0 when $t > 0$. The wave functions of H_0 are single particle plane waves. we can expand the field operators in terms of the H_0 eigenstates.

$$\hat{\Phi}(\mathbf{r}) = \frac{1}{\sqrt{V}} \sum_k e^{i\mathbf{k}\cdot\mathbf{r}} \hat{a}_\mathbf{k}, \tag{G.13}$$

where the dimensionless operators $\hat{a}_\mathbf{k}$ satisfy

$$[\hat{a}_\mathbf{k}, \hat{a}^\dagger_{\mathbf{k}'}] = \delta_{\mathbf{k},\mathbf{k}'}. \tag{G.14}$$

Therefore

$$\hat{n}(\mathbf{r}, t) = \frac{1}{V} \sum_{\mathbf{k},\mathbf{k}'} e^{it(E_\mathbf{k} - E_{\mathbf{k}'})} e^{-i(\mathbf{k}-\mathbf{k}')\cdot\mathbf{r}} \hat{a}^\dagger_\mathbf{k} \hat{a}_{\mathbf{k}'}. \tag{G.15}$$

We can also expand it in the bases of $\mathcal{H}_\infty$

$$\hat{\Phi}(\mathbf{r}) = \sum_\alpha \phi_\alpha(\mathbf{r}) \hat{c}_\alpha, \tag{G.16}$$

where $\phi_\alpha(\mathbf{r})$ are the eigenfunctions before the trap is turned off, and the dimensionless operators c_α satisfy

$$[\hat{c}_\alpha, \hat{c}^\dagger_{\alpha'}] = \delta_{\alpha,\alpha'}. \tag{G.17}$$

Therefore we can equate these two expansions

$$\hat{\Phi}(\mathbf{r}) = \frac{1}{\sqrt{V}} \sum_k e^{i\mathbf{k}\cdot\mathbf{r}} \hat{a}_{\mathbf{k}} = \sum_\alpha \phi_\alpha(\mathbf{r}) \hat{c}_\alpha. \tag{G.18}$$

A Fourier Transform can solve $\hat{a}_{\mathbf{k}}$

$$\int d^3 r e^{-i\mathbf{k}'\cdot\mathbf{r}} \sum_\alpha \phi_\alpha(\mathbf{r}) \hat{c}_\alpha = \sum_{\mathbf{k}} \frac{1}{\sqrt{V}} (2\pi)^3 \hat{a}_{\mathbf{k}} \delta(\mathbf{k} - \mathbf{k}'), \tag{G.19}$$

or

$$\hat{a}_{\mathbf{k}} = \sqrt{V} \sum_\alpha \phi_\alpha(\mathbf{k}) \hat{c}_\alpha, \tag{G.20}$$

where $\mathbf{k}'$ has been rewritten as $\mathbf{k}$, and $\phi_\alpha(\mathbf{k})$ is the Fourier transform of the eigenfunction of $\mathcal{H}_\infty$ in the momentum space. In an equilibrium system, the probability of the state $|i\rangle$ of energy E_i is $e^{-\beta E_i}/Z$. The density matrix is

$$\rho_{\mathcal{H}_\infty} = \frac{1}{Z} \sum_i e^{-\beta E_i} |i\rangle \langle i| = \frac{e^{-\beta \mathcal{H}_\infty}}{Z}. \tag{G.21}$$

So the density

$$\begin{aligned}
n(\mathbf{r}, t) &= \mathrm{Tr} \rho_{\mathcal{H}_\infty} \hat{n}(\mathbf{r}, t) \\
&= \mathrm{Tr}[\frac{e^{-\beta \mathcal{H}_\infty}}{Tre^{-\beta \mathcal{H}_\infty}} \frac{1}{V} \sum_{\mathbf{k},\mathbf{k}'} e^{it(E_{\mathbf{k}} - E_{\mathbf{k}'})} e^{-i(\mathbf{k}-\mathbf{k}')\cdot\mathbf{r}} \hat{a}^\dagger_{\mathbf{k}} \hat{a}_{\mathbf{k}'}] \\
&= \sum_{\mathbf{k},\mathbf{k}'} e^{it(E_{\mathbf{k}} - E_{\mathbf{k}'})} e^{-i(\mathbf{k}-\mathbf{k}')\cdot\mathbf{r}} \sum_{\alpha_0} \langle \alpha_0 | \frac{e^{-\beta \mathcal{H}_\infty}}{Tre^{-\beta \mathcal{H}_\infty}} \sum_{\alpha,\alpha'} \phi^*_\alpha(\mathbf{k}) \hat{c}^\dagger_\alpha \phi_{\alpha'}(\mathbf{k}') \hat{c}_{\alpha'} |\alpha_0\rangle \\
&= \sum_{\alpha_0} \sum_{\mathbf{k}} | e^{itE_{\mathbf{k}} - i\mathbf{k}\cdot\mathbf{r}} |^2 | \phi_{\alpha_0}(\mathbf{k}) |^2 \frac{\langle \alpha_0 | e^{-\beta \mathcal{H}_\infty} \hat{c}^\dagger_{\alpha_0} \hat{c}_{\alpha_0} |\alpha_0\rangle}{\mathrm{Tr}\, e^{-\beta \mathcal{H}_\infty}}.
\end{aligned} \tag{G.22}$$

Because

$$\frac{\mathrm{Tr}\, e^{-\beta \mathcal{H}_\infty} \hat{c}^\dagger_{\alpha_0} \hat{c}_{\alpha_0}}{\mathrm{Tr}\, e^{-\beta \mathcal{H}_\infty}} = \langle \hat{c}^\dagger_{\alpha_0} \hat{c}_{\alpha_0} \rangle, \tag{G.23}$$

the density is expressed as

$$n(\mathbf{r},t) = \sum_{\alpha_0}\sum_{\mathbf{k}} \left| e^{itE_{\mathbf{k}} - i\mathbf{k}\cdot\mathbf{r}} \phi_{\alpha_0}(\mathbf{k}) \right|^2 n_B(\varepsilon_{\alpha_0} - \mu). \tag{G.24}$$

If we translationally move in the momentum space from $\mathbf{k}$ to $\mathbf{k} + m\mathbf{r}/t$, where $\mathbf{k} \ll m\mathbf{r}/t$, Eq. G.24 becomes

$$n(\mathbf{r},t) \approx c \sum_{\alpha_0} \mid \phi_{\alpha_0}(\mathbf{k} = \mathbf{r}m/t) \mid^2 n_B(\varepsilon_{\alpha_0} - \mu), \tag{G.25}$$

where c is an overall constant prefactor. The above equation is the starting point for us to calculate the density after the free expansion.

Sometimes it may be more convenient to work in Bloch or Wannier bases. To calculate the density of the freely expanded cloud, one only has to expand the field operator into the needed basis, and work through similar steps.

Free expansion in Wannier basis The expanded density can be obtained in Wannier basis similarly as in the non-interacting eigenfunction basis. We still have the expansion G.13, and the density operator can still be expressed as Eq. G.15.

$$\hat{n}(\mathbf{r},t) = \frac{1}{V} \sum_{\mathbf{k},\mathbf{k}'} e^{it(E_{\mathbf{k}} - E_{\mathbf{k}'})} e^{-i(\mathbf{k}-\mathbf{k}')\cdot\mathbf{r}} a^\dagger_{\mathbf{k}} a_{\mathbf{k}'}. \tag{G.26}$$

Now expand $\Phi(\mathbf{r})$ in Wannier basis as in Eq. C.19, we have

$$\Phi(\mathbf{r}) = \frac{1}{\sqrt{V}} \sum_{k} e^{i\mathbf{k}\cdot\mathbf{r}} a_{\mathbf{k}} = \sum_{n\mathbf{R}} w_n(\mathbf{r} - \mathbf{R}) b_n(\mathbf{R}), \tag{G.27}$$

where $b_n(\mathbf{R})$ is the Wannier annihilation operator. We again use Fourier Transform to obtain $a_{\mathbf{k}}$,

$$a_{\mathbf{k}} = \frac{1}{\sqrt{V}} \sum_{n\mathbf{R}} e^{-i\mathbf{k}\cdot\mathbf{R}} \tilde{w}_n(\mathbf{k}) b_n(\mathbf{R}), \tag{G.28}$$

where $\tilde{w}_n(\mathbf{k})$ is the Fourier transformed wannier function

$$\tilde{w}_n(\mathbf{k}) = \int d^3 r e^{-i\mathbf{k}\cdot\mathbf{r}} w_n(\mathbf{r}). \tag{G.29}$$

Plug $a_{\mathbf{k}}$ into the density, we get

$$\hat{n}(\mathbf{r},t) = \frac{1}{V^2}\sum_{\mathbf{k},\mathbf{k}'}\sum_{n\mathbf{R}}\sum_{n'\mathbf{R}'} e^{it(E_{\mathbf{k}}-E_{\mathbf{k}'})} e^{-i(\mathbf{k}-\mathbf{k}')\cdot\mathbf{r}} e^{i\mathbf{k}\cdot\mathbf{R}-i\mathbf{k}'\cdot\mathbf{R}'} \tilde{w}_n^*(\mathbf{k})\tilde{w}_{n'}(\mathbf{k}') b_n^\dagger(\mathbf{R}) b_{n'}(\mathbf{R}'). \tag{G.30}$$

Shift $\mathbf{k}$ to $\mathbf{k} + m\mathbf{r}/t$, we get

$$\hat{n}(\mathbf{r},t) = \frac{1}{V^2}\sum_{\mathbf{k},\mathbf{k}'}\sum_{n\mathbf{R}}\sum_{n'\mathbf{R}'} e^{it(E_{\mathbf{k}}-E_{\mathbf{k}'})} e^{i(\mathbf{k}+\frac{m\mathbf{r}}{t})\cdot\mathbf{R}-i(\mathbf{k}'+\frac{m\mathbf{r}}{t})\cdot\mathbf{R}'} \tilde{w}_n^*(\mathbf{k}+\frac{m\mathbf{r}}{t})\tilde{w}_{n'}(\mathbf{k}'+\frac{m\mathbf{r}}{t}) b_n^\dagger(\mathbf{R}) b_{n'}(\mathbf{R}'). \tag{G.31}$$

For the expanded cloud, assume $\mathbf{k} \ll m\mathbf{r}/t$, then

$$\begin{aligned}
&\hat{n}(\mathbf{r},t) \\
&= \frac{1}{V^2}\sum_{n\mathbf{R}}\sum_{n'\mathbf{R}'} \mid \sum_{\mathbf{k}} e^{itE_{\mathbf{k}}} \mid^2 e^{i\frac{m\mathbf{r}}{t}\cdot\mathbf{R}-i\frac{m\mathbf{r}}{t}\cdot\mathbf{R}'} \tilde{w}_n^*(\frac{m\mathbf{r}}{t})\tilde{w}_{n'}(\frac{m\mathbf{r}}{t}) b_n^\dagger(\mathbf{R}) b_{n'}(\mathbf{R}') \\
&= (\frac{m}{2\pi\hbar^2 t})^3 \sum_{n\mathbf{R}}\sum_{n'\mathbf{R}'} e^{i\frac{m\mathbf{r}}{t}\cdot\mathbf{R}-i\frac{m\mathbf{r}}{t}\cdot\mathbf{R}'} \tilde{w}_n^*(\frac{m\mathbf{r}}{t})\tilde{w}_{n'}(\frac{m\mathbf{r}}{t}) b_n^\dagger(\mathbf{R}) b_{n'}(\mathbf{R}'),
\end{aligned} \tag{G.32}$$

which is a summation over band indices and lattice sites. In the last step the following sum has been used (λ is an introduced real part which is let to be 0 eventually)

$$\begin{aligned}
&\sum_{\mathbf{k}} e^{-itE_{\mathbf{k}}} \\
&= \frac{V}{(2\pi)^3}\int d^3 k e^{-it\hbar^2 k^2/2m} \\
&= \frac{V}{2\pi^2}(\frac{2m}{t})^{3/2}\int_0^\infty k^2 dk e^{-i\hbar^2 k^2 - \lambda k^2} \\
&= \frac{V}{2\pi^2}(\frac{2m}{t})^{3/2}\frac{\sqrt{\pi}}{4(i\hbar^2+\lambda)^{3/2}} \\
&\approx \frac{V}{2\pi^2}(\frac{2m}{t})^{3/2}\frac{\sqrt{\pi}}{4i^{3/2}\hbar^3}.
\end{aligned} \tag{G.33}$$

Free expansion in Bloch basis Using the same method, $\Phi(\mathbf{r})$ can be expanded in two bases:

$$\Phi(\mathbf{r}) = \frac{1}{\sqrt{V}} \sum_k e^{i\mathbf{k}\cdot\mathbf{r}} a_{\mathbf{k}} = \frac{1}{\sqrt{V}} \sum_{n\mathbf{q}} c_{n\mathbf{q}} \psi_{n\mathbf{q}}(\mathbf{r}), \tag{G.34}$$

where $c_{n\mathbf{q}}$ is the Bloch annihilation operator, q is in the first Brillouin zone. $a_{\mathbf{k}}$ is obtained from Fourier Transform

$$a_{\mathbf{k}} = \frac{1}{\sqrt{V}} \sum_{n\mathbf{q}} \tilde{\psi}_{n\mathbf{q}}(\mathbf{k}) c_{n\mathbf{q}}, \tag{G.35}$$

where the Fourier transformed Bloch function

$$\tilde{\psi}_{n\mathbf{q}}(\mathbf{k}) = \frac{1}{\sqrt{V}} \int d^3 r e^{-i\mathbf{k}\cdot\mathbf{r}} \psi_{n\mathbf{q}}(\mathbf{r}). \tag{G.36}$$

Plug into the density, and then shift $\mathbf{k}$ to $\mathbf{k} + m\mathbf{r}/t$, where we also assume $\mathbf{k} \ll m\mathbf{r}/t$, we get

$$\hat{n}(\mathbf{r}, t) = (\frac{m}{2\pi\hbar^2 t})^3 \sum_{n\mathbf{q}} \sum_{n'\mathbf{q}'} \tilde{\psi}^*_{n\mathbf{q}}(\frac{m\mathbf{r}}{t}) \tilde{\psi}_{n'\mathbf{q}'}(\frac{m\mathbf{r}}{t}) c^\dagger_{n\mathbf{q}} c_{n'\mathbf{q}'}, \tag{G.37}$$

which is a summation over band indices and momenta.

APPENDIX H
RABI OSCILLATION

Consider a two level system of an atom in an electromagnetic field. Atoms at the ground state can absorb photons and be excited, atoms at the excited state can emit photons while being de-exited. If the emission of a photon is due to the effect of another photon passing by, the emission is called stimulated emission (otherwise it is spontaneous emission). If there is a constant source of photons, the atoms can enter into a cycle of absorbing and emitting photons through stimulated emission. Such a cycle is called the Rabi cycle, its frequency is the Rabi frequency. Here we will mathematically describe this process in a semi-classical approach (Rabi Model).

The total Hamiltonian of the system consists of three parts, the atomic Hamiltonian, the field's Hamiltonian, and the Hamiltonian for the interaction between the atom and the field:

$$H = H_{atom} + H_{field} + H_{atom-field}. \tag{H.1}$$

Denote the excited state as $|e\rangle$, the ground state as $|g\rangle$. The Hamiltonian is written as

$$H_{atom} = \hbar\omega_e |e\rangle \langle e| + \hbar\omega_g |g\rangle \langle g| . \tag{H.2}$$

Let the ground state at zero energy, then

$$H_{atom} = \hbar\omega_0 |e\rangle \langle e| , \tag{H.3}$$

where ω_e has been rewritten as ω_0, the transition frequency. The classic field is

$$\mathbf{E} = \mathbf{E_0}\, e^{-i\omega_L t} + \mathbf{E}_0^*\, e^{i\omega_L t}, \tag{H.4}$$

where ω_L is the photon frequency of the field. The free field Hamiltonian in the classical picture can be neglected:

$$H_{field} = 0. \tag{H.5}$$

The atom has an electric dipole moment $\mathbf{D}$ coupling with the field, which enables the transition between states. If the system stays in the same state, it retains the shape of the electric cloud, so the diagonal elements in $\mathbf{D}$, $\mathbf{d}_{gg}$, $\mathbf{d}_{ee}$ are zero. The total dipole moment can be written as

$$\mathbf{D} = \mathbf{d}_{eg} \left|e\right\rangle \left\langle g\right| + \mathbf{d}_{eg}^{*} \left|g\right\rangle \left\langle e\right|, \tag{H.6}$$

where we have used the Hermitian relationship $\mathbf{d}_{ge} = \mathbf{d}_{eg}^{*}$. The dipole moment can also be equivalently written as

$$\mathbf{D} = (\mathbf{d}_{eg}\hat{\sigma}_{+} + \mathbf{d}_{eg}^{*}\hat{\sigma}_{-})/2, \tag{H.7}$$

where $\hat{\sigma}_{\pm}$ are the ladder operators

$$\hat{\sigma}_{+} = \sigma_1 - i\sigma_2 = \begin{pmatrix} 0 & 0 \\ 2 & 0 \end{pmatrix}; \tag{H.8}$$

$$\hat{\sigma}_{-} = \sigma_1 + i\sigma_2 = \begin{pmatrix} 0 & 2 \\ 0 & 0 \end{pmatrix}, \tag{H.9}$$

where σ_1 and σ_2 are Pauli matrices. Note that the definition of $\sigma_{\pm}$ is a bit different from usual. Then the atom-field interaction Hamiltonian is

$$H_{atom-field} = -(\mathbf{d}_{eg} \left|e\right\rangle \left\langle g\right| + \mathbf{d}_{eg}^{*} \left|g\right\rangle \left\langle e\right|) \cdot (\mathbf{E_0}\, e^{-i\omega_L t} + \mathbf{E}_0^{*}\, e^{i\omega_L t}). \tag{H.10}$$

We can write

$$\mathbf{d}_{eg} \cdot \mathbf{E}_0 \equiv \hbar\Omega; \tag{H.11}$$

$$\mathbf{d}_{eg} \cdot \mathbf{E}_0^* \equiv \hbar\tilde{\Omega}. \tag{H.12}$$

So the total Hamiltonian written in the matrix form is

$$H = \hbar \begin{pmatrix} 0 & -\tilde{\Omega}^* e^{-i\omega_L t} - \Omega^* e^{i\omega_L t} \\ -\Omega e^{-i\omega_L t} - \tilde{\Omega} e^{i\omega_L t} & \omega_0 \end{pmatrix}. \tag{H.13}$$

The Hamiltonian in the interaction picture is

$$\begin{aligned} \mathcal{H}_I &= e^{iH_{atom}t} H e^{-iH_{atom}t} \\ &= \hbar \begin{pmatrix} 0 & -\tilde{\Omega}^* e^{-i(\omega_L+\omega_0)t} - \Omega^* e^{i(\omega_L-\omega_0)t} \\ -\Omega e^{-i(\omega_L-\omega_0)t} - \tilde{\Omega} e^{i(\omega_L+\omega_0)t} & \omega_0 \end{pmatrix}. \end{aligned} \tag{H.14}$$

The electric fields of $\omega_L + \omega_0$ frequency are $2\omega_0$ away from resonance. These rapidly oscillating terms will soon average to zero, therefore we can neglect them. This approximation is called the rotating wave approximation. Now if we write $\omega_L - \omega_0$ as Δ ("detuning"), then

$$\mathcal{H}_I = \hbar \begin{pmatrix} 0 & -\Omega^* e^{i\Delta t} \\ -\Omega e^{-i\Delta t} & \omega_0 \end{pmatrix}. \tag{H.15}$$

Therefore the Schrödinger equation in this picture is

$$\mathcal{H}\tilde{\Psi} = i\hbar \frac{d\tilde{\Psi}}{dt}, \tag{H.16}$$

where

$$\mathcal{H} = -\frac{\hbar}{2}(\Omega^* e^{i\Delta t}\sigma_- + \Omega e^{-i\Delta t}\sigma_+), \tag{H.17}$$

and $\tilde{\Psi}$ is transformed from Ψ

$$\tilde{\Psi} = e^{iH_{atom}t}\Psi. \tag{H.18}$$

The solution is

$$\Psi = c_1 |g\rangle + c_2 |e\rangle , \tag{H.19}$$

where

$$c_1 = \exp[-\frac{i\Delta t}{2}](-\frac{\Delta - \Omega_R}{2\Omega_R}\exp[\frac{i}{2}\Omega_R t] + \frac{\Delta + \Omega_R}{2\Omega_R}\exp[-\frac{i}{2}\Omega_R t]); \tag{H.20}$$

$$c_2 = \exp[-\frac{i}{2}(\omega_0 + \omega_L)t](-\frac{\Omega}{\Omega_R}\exp[\frac{i}{2}\Omega_R t] + \frac{\Omega}{\Omega_R}\exp[-\frac{i}{2}\Omega_R t]), \tag{H.21}$$

where

$$\Omega_R = \sqrt{4|\Omega|^2 + \Delta^2} \tag{H.22}$$

is defined as the Rabi frequency. c_1 and c_2 are already normalized. The probability of the atom at the excited state is

$$P(|e\rangle) = |c_2|^2 = 4\left|\frac{\Omega}{\Omega_R}\right|^2 \sin^2\frac{\Omega_R t}{2}, \tag{H.23}$$

which proves that Ω_R is the frequency at which the atom oscillates.

APPENDIX I
EFFECTIVE LOW-ENERGY HAMILTONIAN

In this appendix we derive the low energy effective Hamiltonian for a ^{87}Rb BEC with spin-orbit coupling, focusing on states near the minima of $\varepsilon_-(\mathbf{p})$ (occuring at $\pm p_0 \approx k_L$ for $\delta \to 0$). Our analysis closely follows Ref. [34].

Effective Bare Hamiltonian

In Chapter 6, we have the original bare Hamiltonian

$$H_0 = \begin{pmatrix} \frac{\hat{p}^2}{2m} + \frac{\delta}{2} & \frac{1}{2}\Omega e^{2ik_L x} \\ \frac{1}{2}\Omega e^{-2ik_L x} & \frac{\hat{p}^2}{2m} - \frac{\delta}{2} \end{pmatrix}, \tag{I.1}$$

and the rotated bare Hamiltonian,

$$\hat{H}_r(\mathbf{p}, \delta) = \frac{1}{2m}(\mathbf{p}^2 + \mathbf{k}_L^2) + \frac{1}{2}\delta\sigma_z + \frac{1}{2}\Omega\sigma_x + \frac{1}{m}k_L\sigma_z\hat{p}_x, \tag{I.2}$$

The original and rotated Hamiltonians are connected by a unitary transformation $\hat{H}_r = \hat{U}^\dagger H_0 \hat{U}$ where the unitary operator $U = \mathrm{e}^{i\mathbf{k}_L\cdot\mathbf{r}\sigma_z}$, with σ_z being the Pauli matrix.

We start by noting the eigenstates of the rotated Hamiltonian $\hat{H}_r$:

$$\hat{\psi}_{\mathbf{p}+} = \frac{1}{\mathcal{N}(p_x, \delta)} \begin{pmatrix} -1 \\ f(p_x, \delta) \end{pmatrix}, \tag{I.3}$$

$$\hat{\psi}_{\mathbf{p}-} = \frac{1}{\mathcal{N}(p_x, \delta)} \begin{pmatrix} f(p_x, \delta) \\ 1 \end{pmatrix}, \tag{I.4}$$

corresponding to the eigenvalues Eq. 6.2. Here, we defined

$$f(p_x,\delta)=\frac{\delta+\frac{2k_Lp_x}{m}-\sqrt{\Omega^2+\delta^2+\frac{4k_L^2p_x^2}{m^2}+\frac{4k_L\delta p_x}{m}}}{\Omega}, \tag{I.5}$$

and the normalization factor $\mathcal{N}(p_x,\delta)=\sqrt{1+f(p_x,\delta)^2}$.

Denote $f_0(p)=f(p,\delta=0)$, it can be verified that for small δ

$$f(p_x,\delta)\simeq f_0(p_x)-\frac{f_0(p_x)}{\sqrt{\Omega^2+\frac{4k_L^2p_x^2}{m^2}}}\delta. \tag{I.6}$$

In addition, we have the following relationship

$$f(p_r,\delta)f(p_\ell,\delta)\simeq\frac{(\hat{\delta}-1+\hat{\Omega}^2)^2}{(-1+\hat{\Omega}^2)^2} \tag{I.7}$$

and

$$(1+f(p_r,\delta)^2)(1+f(p_\ell,\delta)^2)\simeq\frac{64{E_L}^2}{\Omega^2}-\frac{512{E_L}^3\delta}{16{E_L}^2\Omega^2-\Omega^4}=\frac{4}{\hat{\Omega}^2}-\frac{8}{\hat{\Omega}^2-\hat{\Omega}^4}\hat{\delta}. \tag{I.8}$$

Specifically, when $\delta=0$, $f_0(p_0)f_0(-p_0)=1$ and $[1+f_0(p_0)^2][1+f_0(-p_0)^2]=4/\hat{\Omega}^2$.

Next, we turn the momentum space eigenfunctions into real space, i.e. $e^{i\mathbf{p}\cdot\mathbf{r}}\hat{\psi}_{\mathbf{p}\pm}$, then transform back into the original basis by applying the same unitary operator U to obtain the eigenfunction of H_0: $\hat{\Psi}_{\mathbf{p}\alpha}(\mathbf{r})=\hat{U}\hat{\psi}_{\mathbf{p}\alpha}e^{i\mathbf{p}\cdot\mathbf{r}}$ (where $\hat{U}=e^{i\mathbf{k}_L\cdot\mathbf{r}\sigma_z}$) and finally express the original field $\Psi(\mathbf{r})$ in terms of operators $\psi_\alpha(\mathbf{p})$ with momentum $\mathbf{p}$ in band $\alpha=\pm$:

$$\Psi(\mathbf{r})=\sum_{\mathbf{p},\alpha=\pm}\hat{\Psi}_{\mathbf{p}\alpha}(\mathbf{r})\psi_\alpha(\mathbf{p}). \tag{I.9}$$

At low energies, it is sufficient to restrict attention to the lower $(-)$ band and focus on $\mathbf{p}$ close to the right $(\mathbf{p}_r)$ and left $(\mathbf{p}_\ell)$ minima of $\varepsilon_-(\mathbf{p},\delta)$:

$$\begin{aligned}\Psi(\mathbf{r}) &= \sum_{p<\Lambda, a=r,\ell} \hat{\Psi}_{\mathbf{p}+\mathbf{p}_a -}(\mathbf{r})\psi_-(\mathbf{p}+\mathbf{p}_a), \\ &= \sum_{p<\Lambda} \left[\hat{\Psi}_{\mathbf{p}+\mathbf{p}_r -}(\mathbf{r})\psi_{\downarrow'}(\mathbf{p}) + \Psi_{\mathbf{p}+\mathbf{p}_\ell -}(\mathbf{r})\psi_{\uparrow'}(\mathbf{p})\right],\end{aligned} \tag{I.10}$$

where in the second line we introduced the notation $\psi_{\downarrow'}(\mathbf{p}) = \psi_-(\mathbf{p}+\mathbf{p}_r)$ and $\psi_{\uparrow'}(\mathbf{p}) = \psi_-(\mathbf{p}+\mathbf{p}_\ell)$ for the states near $\mathbf{p}_r$ and $\mathbf{p}_\ell$; the notation $\downarrow'$ and $\uparrow'$ follows since, for vanishing light-atom coupling $\Omega \to 0$, the states near the right (left) minimum map onto the $\downarrow$ $(\uparrow)$ band of Eq. *I*.1.

Plugging this into the single-particle Hamiltonian $\mathcal{H}_0$, and using the orthonormality of the eigenfunctions of Eq. *I*.1, we obtain

$$\mathcal{H}_0 = \sum_{\mathbf{p}<\Lambda, \sigma=\uparrow',\downarrow'} \varepsilon_\sigma(\mathbf{p})\psi^\dagger_\sigma(\mathbf{p})\psi_\sigma(\mathbf{p}), \tag{I.11}$$

where the dispersion $\varepsilon_\sigma(\mathbf{p})$ is given by $\varepsilon_{\uparrow'}(\mathbf{p}) = \varepsilon_-(\mathbf{p}+\mathbf{p}_\ell)$ and $\varepsilon_{\downarrow'}(\mathbf{p}) = \varepsilon_-(\mathbf{p}+\mathbf{p}_r)$.

Eq. *I*.11 can be simplified further by noting that, as shown below and in agreement with the expermental findings of Ref. [34], the mixed phase is only stable for a small range of δ values, so that this parameter can be taken to be small. To leading order in small $\delta/4E_L$, the minima of $\varepsilon_-(\mathbf{p})$ occur at

$$p_{r,\ell} \simeq \pm k_L\sqrt{1-\hat{\Omega}^2} + k_L\hat{\delta}\frac{\hat{\Omega}^2}{1-\hat{\Omega}^2}, \tag{I.12}$$

with the $+$ $(-)$ corresponding to the right (left) minimum. Here, we defined $\hat{\Omega} = \Omega/4E_L$ and $\hat{\delta} = \delta/4E_L$. Since stability of the mixed phase also requires $\hat{\Omega} \ll 1$ as well as $\hat{\delta} \ll 1$, it is clear that the final term in this expression can be neglected

compared to the first term, implying that the locations of the minima of $\varepsilon_-(\mathbf{p})$ are close to $p_x = \pm k_L\sqrt{1-\hat{\Omega}^2}$. Inserting these values into $\varepsilon_-(\mathbf{p})$, and again neglecting terms of order $\hat{\Omega}^2\hat{\delta}$, we find the energies of the local minima to be:

$$\varepsilon_-(\mathbf{p}_{r/\ell}) = E_L\big(\hat{\Omega}^2 \pm 2\hat{\delta}\big), \tag{I.13}$$

with the $-$ $(+)$ corresponding to the right (left) minima. The preceding calculations show that, for sufficiently small values of δ, the effect of nonzero δ is simply to apply a chemical potential difference, lowering the $\downarrow'$ state energy for $\delta > 0$ and the $\uparrow'$ state energy for $\delta < 0$. Expanding the disperions $\varepsilon_-(\mathbf{p})$ to leading order $\mathbf{p}$ near these minima, we finally arrive at (including a chemical potential μ that couples to the density and defining $\mu_{\uparrow'} = \mu - \frac{1}{2}\delta$ and $\mu_{\downarrow'} = \mu + \frac{1}{2}\delta$):

$$\mathcal{H}_0 = \sum_{\sigma=\uparrow',\downarrow'} \int d^3r \big(\varepsilon(\mathbf{p}) - \mu_\sigma\big)\psi^\dagger_\sigma(\mathbf{r})\psi_\sigma(\mathbf{r}), \tag{I.14}$$

where $\mu_{\uparrow'} = \mu - \frac{1}{2}\delta$ and $\mu_{\downarrow'} = \mu + \frac{1}{2}\delta$, with μ the chemical potential. In Eq. *I.14* we also dropped an overall constant, the first term of Eq. *I.13*. Here, the effective dispersion is

$$\varepsilon(\mathbf{p}) = \frac{1}{2m^*}p_x^2 + \frac{1}{2m}(p_y^2 + p_z^2) \tag{I.15}$$

with a different effective mass m^* in the x direction, reflecting the curvature of the minima of $\varepsilon_-(\mathbf{p})$, that satisfies $(m^*)^{-1} = m^{-1}(1-\hat{\Omega}^2)$.

Effective Interaction Hamiltonian

After obtaining the effective bare Hamiltonian, we now turn to the interaction Hamiltonian. From Chapter 2.5, the interaction Hamiltonian for a BEC with two

species of bosons is

$$\begin{aligned}\mathcal{H}_{int} &= \frac{1}{2}\int d^3r\ [c_0(n_\uparrow + n_\downarrow)^2 + c_2(2n_\uparrow n_\downarrow + {n_\downarrow}^2)] \\ &= \frac{1}{2}\int d^3r\ [(c_0 + \frac{c_2}{2})(n_\uparrow + n_\downarrow)^2 + \frac{c_2}{2}({n_\downarrow}^2 - {n_\uparrow}^2) + c_2 n_\uparrow n_\downarrow] \\ &= \frac{1}{2}\int d^3r \Big[(c_0 + c_2)n_\downarrow^2 + c_0 n_\uparrow^2 + 2(c_0 + c_2)n_\uparrow n_\downarrow\Big],\end{aligned} \tag{I.16}$$

where c_0 and c_2 are interaction parameters, densities of the original spin species $n_\sigma = \Psi_\sigma^\dagger \Psi_\sigma$ with $\sigma = \uparrow, \downarrow$ and normal ordering is implied.

To obtain the effective interactions among the dressed bosons, we need to use Eq. *I*.10 in Eq. *I*.16. For Eq. *I*.10, we need the eigenfunctions near the minima at $\mathbf{p}_r$ and $\mathbf{p}_\ell$. Defining the Fourier transform $\psi_\sigma(\mathbf{r}) = \sum_{\mathbf{p}} e^{i\mathbf{p}\cdot\mathbf{r}}\psi_\sigma(\mathbf{p})$ (essentially taking the cutoff parameter $\Lambda \to \infty$), we write Eq. *I*.10 as

$$\begin{aligned}\Psi(\mathbf{r}) &= \sum_{p<\Lambda}\Big[\hat{\Psi}_{\mathbf{p}+\mathbf{p}_r-}(\mathbf{r})\psi_{\downarrow'}(\mathbf{p}) + \Psi_{\mathbf{p}+\mathbf{p}_\ell-}(\mathbf{r})\psi_{\uparrow'}(\mathbf{p})\Big], \\ &= \sum_{p<\Lambda}\Big[\hat{U}\hat{\psi}_{\mathbf{p}+\mathbf{p}_r-}e^{i(\mathbf{p}+\mathbf{p}_r)\cdot\mathbf{r}}\psi_{\downarrow'}(\mathbf{p}) + \hat{U}\hat{\psi}_{\mathbf{p}+\mathbf{p}_\ell-}e^{i(\mathbf{p}+\mathbf{p}_\ell)\cdot\mathbf{r}}\psi_{\uparrow'}(\mathbf{p})\Big] \\ &\simeq \hat{U}\hat{\psi}_{\mathbf{p}_r-}e^{i\mathbf{p}_r\cdot\mathbf{r}}\psi_{\downarrow'}(\mathbf{r}) + \hat{U}\hat{\psi}_{\mathbf{p}_\ell-}e^{i\mathbf{p}_\ell\cdot\mathbf{r}}\psi_{\uparrow'}(\mathbf{r}).\end{aligned} \tag{I.17}$$

After approximating the functions $f(\mathbf{p}+\mathbf{p}_r,\delta) \simeq f(\mathbf{p}_r,\delta)$ (and similarly for $f(\mathbf{p}+\mathbf{p}_\ell,\delta)$), we obtain

$$\Psi(\mathbf{r}) \simeq \frac{1}{\mathcal{N}(\mathbf{p}_r,\delta)}\begin{pmatrix} f(\mathbf{p}_r,\delta)e^{2ik_Lx} \\ 1\end{pmatrix}\psi_{\downarrow'}(\mathbf{r}) + \frac{1}{\mathcal{N}(\mathbf{p}_\ell,\delta)}\begin{pmatrix} f(\mathbf{p}_\ell,\delta) \\ e^{-2ik_Lx}\end{pmatrix}\psi_{\uparrow'}(\mathbf{r}). \tag{I.18}$$

We then insert Eq. *I*.18 into Eq. *I*.16. Again focusing on the limit of small $\hat{\Omega}$, we keep terms up to order $c_0\hat{\Omega}^2$ (discarding terms with rapidly-varying exponential factors) and take the limit $\hat{\Omega} \to 0$ in the terms proportional to c_2 (since $|c_2| \ll c_0$). Just as what we found for $\mathcal{H}_0$, the corrections due to $\hat{\delta}$ are also subdominant here,

leading to the final interaction Hamiltonian

$$\mathcal{H}_1 = \frac{1}{2}\int d^3r \Big[(c_0+c_2)|\psi_{\downarrow'}(\mathbf{r})|^4 + c_0|\psi_{\uparrow'}(\mathbf{r})|^4 + 2\big[c_0(1+\hat{\Omega}^2)+c_2\big]|\psi_{\uparrow'}(\mathbf{r})|^2|\psi_{\downarrow'}(\mathbf{r})|^2\Big], \tag{I.19}$$

where normal ordering is implied. This is the effective interaction Hamiltonian for dressed states. Comparing with Eq. *I*.16, Eq. *I*.19 has an extra term proportional to $\hat{\Omega}^2$. More generally, this term can be characterized by a parameter $c'_{\uparrow\downarrow}$, so that

$$\mathcal{H}_1 = \frac{1}{2}\int d^3r \Big[(c_0+c_2)|\psi_{\downarrow'}(\mathbf{r})|^4 + c_0|\psi_{\uparrow'}(\mathbf{r})|^4 + 2\big(c_0+c_2+\frac{c'_{\uparrow\downarrow}}{2}\big)|\psi_{\uparrow'}(\mathbf{r})|^2|\psi_{\downarrow'}(\mathbf{r})|^2\Big]. \tag{I.20}$$

Thus, we see that, in agreement with Ref. [34], the leading impact of SOC on the ^{87}Rb interactions is to renormalize the interatomic interactions.

VITA

Qin-Qin Lü was born in Wuxue (formerly the County of Guangji), Hubei Province, China. He attended University of Science and Technology of China from 2003 and obtained a Bachelor of Science degree in physics in 2008. In August 2008, he entered the graduate school of Louisiana State University in Baton Rouge to pursue his Doctor of Philosophy degree. Besides physics, he has passions for food, music, museums, archaeology and geography.